Probing magnetic fluctuations close to quantum critical points by neutron scattering

DISSERTATION

zur Erlangung des akademischen Grades

Doctor rerum naturalium

(Dr. rer. nat.)

vorgelegt

der Fakultät Mathematik und Naturwissenschaften der
Technischen Universität Dresden

von

Anna Zita Hüsges

(Master of Science)

geboren am 10. April 1985 in Berlin

Eingereicht am 20. Oktober 2015
Verteidigt am 30. März 2016

Contents

List of Acronyms

AC	Alternating current
AF	Antiferromagnet/Antiferromagnetic/Antiferromagnetism
CEF	Crystal electric field
EDX	Energy-dispersive x-ray spectroscopy
FL	Fermi liquid
FM	Ferromagnet/Ferromagnetic/Ferromagnetism
FRM2	Forschungsreaktor München 2
FWHM	Full width at half maximum
HMM	Hertz-Millis-Moriya
HZB	Helmholtz-Zentrum Berlin
ILL	Institut Laue-Langevin
PPMS	Physical Property Measurement System (*product name*)
PSI	Paul Scherrer Institut
QCP	Quantum critical point
QE	Quasi-elastic
RG	Renormalisation group
RKKY	Ruderman-Kittel-Kasuya-Yosida
SCR	Self-consistent renormalisation
SHE	Superconducting Helium Electronics (*brand name*)
ToF	Time of flight
XRD	X-ray diffraction

List of Physical Constants

Elementary charge	$e =$	$1.602 \cdot 10^{-19}$ As
Planck constant	$h =$	$6.626 \cdot 10^{-34}$ Js
Reduced Planck constant	$\hbar =$	$h/2\pi = 1.055 \cdot 10^{-34}$ Js
Boltzmann constant	$k_{\mathrm{B}} =$	$1.381 \cdot 10^{-23}$ J/K
Avogadro constant	$N_{\mathrm{A}} =$	$6.022 \cdot 10^{23}$ 1/mol
Gas constant	$R =$	8.314 J/(mol·K)
Vacuum permeability	$\mu_0 =$	$4\pi \cdot 10^{-7}$ Vs/(Am)
Bohr magneton	$\mu_{\mathrm{B}} =$	$9.274 \cdot 10^{-24}$ J/T

Chapter 1

Introduction

Quantum mechanics describes the processes at the length scale of atoms and molecules, which in turn make up the objects of our everyday life. Thus, there is essentially no single physical movement that does not involve quantum mechanics - and yet, physical science was able to describe much of the world before quantum effects were even discovered. The reason behind this astonishing occurrence is that quantum effects tend to average out on longer length scales, leading to behaviour for macroscopic objects which can be well described by classical theories. There is, of course, a multitude of observations which can only be explained by an explicit use of quantum theories - a famous example is the photoelectric effect, which has contributed much to the initial development of quantum mechanics. Also some states of matter, such as superconductivity, are impossible to understand on a classical basis. Still, quasi-classical theories continue to be very useful for describing experiments on a macroscopic length scale, as they commonly occur in the study of condensed matter physics.

In the last decades, there has been an enhanced interest in systems where quantum effects need to be dealt with explicitly. One way to achieve this is to reduce the system size, which is realised in the field of nanophysics. However, macroscopic objects may also display exotic properties caused by quantum phenomena. Such compounds are the centre of interest in the field of strongly correlated electron systems, which deals with the electronic properties of solids that require theories beyond the mean-field description.

One of the compound classes of strongly correlated electron systems is the so-called heavy fermions. They are metals, usually containing f-elements, whose charge carriers at low temperatures have effective masses which are hundreds of times higher than that of the free electron [Ful95, Mis08]. Within the Fermi-liquid concept [Lan57], this is explained by interactions between the electrons in the solid - loosely speaking, the interactions slow down the

charge carriers, making them appear 'heavy'. Heavy fermions are important in the study of quantum phenomena, as they can be used to investigate quantum criticality: Here, critical fluctuations occur at zero temperature, which implies that they are not thermal, but quantum in nature. Quantum fluctuations can be observed if a second-order phase transition happens at zero temperature. Many heavy-fermion compounds have a magnetically ordered state at temperatures as low as ≈ 1 K; the value of the transition temperature is often rather sensitive to the application of pressure or magnetic field, so that it can easily be tuned to $T = 0$. Such a point in the p, T or B, T phase diagram is called a quantum critical point [LRVW07]. In its vicinity, quantum fluctuations dominate the physical properties, which results in unusual behaviour and possibly exotic phases.

The concept of quantum criticality goes far beyond heavy fermions. The appearance of exotic phases around quantum critical points seems to be a generic observation. This is particularly discussed for unconventional superconductivity, which is thought to be driven by magnetic excitations rather than by phonons. Phases of unconventional superconductivity have been frequently found close to magnetic quantum critical points for heavy fermions, and also for cuprate and pnictide compounds [Sca12]. The latter two have attracted much attention, also outside of basic research, due to their high transition temperatures: For the cuprates, these often far exceed liquid nitrogen temperature (77 K), while for pnictides the record is still above 50 K. In heavy-fermion compounds the relevant energy scales are around two orders of magnitude smaller, meaning that transition temperatures are far below any commercially interesting values. However, these low temperatures have a principal advantage: The electronic properties can often be studied much more clearly, since phonons are frozen out and have little impact on the thermodynamic properties of the system. Furthermore, the large effective masses enhance the magnitude of electronic properties. For this reason, the study of quantum criticality in heavy-fermion compounds can give insights that are relevant for a much wider class of solids, and show the origins behind unusual phases and properties.

In this thesis, the behaviour of heavy fermions is studied based mainly on neutron scattering experiments. These give crucial complementary information to thermodynamic measurements, since they yield a microscopic view on magnetism. Neutron scattering directly measures the spin-spin correlation function, giving access to the relevant magnetic interactions in both time (energy) and space (momentum) [Col89]. Three different heavy-fermion compounds are investigated here, $CeCu_2Si_2$, CePdAl and $YbNi_4P_2$. These were chosen due to their ability to be tuned to a quantum critical point. $CeCu_2Si_2$ was in fact the first unconventional superconductor ever reported [SAB$^+$79]

and has therefore received much attention over the last decades. The other two compounds have more recently been discovered for the study of quantum criticality; they do not show superconductivity, but display other unusual properties. CePdAl has a partially frustrated magnetic state [DEM$^+$96], offering the possibility to study the interplay of frustration and quantum criticality [GHU$^+$02, FBG$^+$14]. YbNi$_4$P$_2$ is a very rare example of a ferromagnet that can be tuned to a quantum critical point [KLS$^+$11, SKL$^+$13], making the study of the associated fluctuations particularly interesting.

This thesis is organised as follows. In chapter 2, a basic introduction to the theory behind the experimental work is provided by discussing elementary concepts of phase transitions, quantum criticality, heavy fermions and neutron scattering. Chapter 3 is concerned with neutron spectroscopy on CeCu$_2$Si$_2$: The compound displays a variety of ground states ranging from antiferromagnetic ('A-type') to superconducting ('S-type') including mixed states ('A/S-type'), and the spectroscopic response of these different states will be compared. Some of the crystals were synthesised particularly for this work and therefore a short section on sample preparation is also given. In chapter 4, results of single-crystal neutron diffraction on CePdAl are reported. The role of frustration on the magnetic structure, and also its potential effects on the quantum critical behaviour, will be discussed. Chapter 5 deals with powder neutron spectroscopy of YbNi$_4$P$_2$. This includes the measurement of excitations in the crystal electric field, which are then compared to simulations, and a discussion of ferromagnetic and local magnetic fluctuations. Finally, a concluding discussion for all compounds is given in chapter 6.

Chapter 2

Basics of quantum phase transitions

In the following, a few important concepts for the understanding of this thesis will be presented. In section 2.1, I start by introducing critical phenomena at phase transitions. Here I follow mainly the account given by Collins in his excellent book [Col89], as well as the basic textbook by Nolting [Nol02]. These concepts will then be extended to quantum phase transitions, an approach pioneered by Hertz [Her76] and later refined by other authors [Mil93, MT95]. Next, the case of heavy-fermion compounds is discussed in more detail, before I turn to the role of neutron scattering in the study of (quantum) critical phenomena. This last section will again lend many of its ideas from Collins' book [Col89].

2.1 Phase transitions

Phase transitions occur in a large variety of systems, from everyday phenomena such as the melting of ice to the low-temperature magnetic transitions which are the topic of this thesis. Some common thermodynamic concepts can be used to describe these processes. In classical phase transitions, the transformation from one phase to the other occurs at a critical temperature T_c. At T_c, the (Gibbs) free energy of both phases must be identical:

$$F_1(T_c, V) = F_2(T_c, V) \quad \text{or} \quad G_1(T_c, p) = G_2(T_c, p) \tag{2.1}$$

For the magnetic case, one would write

$$F_1(T_c, \mathbf{M}) = F_2(T_c, \mathbf{M}) \quad \text{or} \quad G_1(T_c, \mathbf{H}) = G_2(T_c, \mathbf{H}), \tag{2.2}$$

where the vector nature of magnetisation **M** and magnetic field **H** needs to be taken into account. It is assumed in all cases that the particle number is conserved.

While the free energy is continuous through the phase transition, its derivatives with respect to temperature may not be equal in both phases at T_c. If the first derivatives are not identical,

$$\frac{\partial F_1}{\partial T} \neq \frac{\partial F_2}{\partial T}, \quad \text{or} \quad \lim_{T \to T_c^+} \frac{\partial F}{\partial T} \neq \lim_{T \to T_c^-} \frac{\partial F}{\partial T}, \tag{2.3}$$

the respective phase transition is called a first-order transition. This implies that there is a jump in the entropy

$$\Delta S = - \lim_{T \to T_c^+} \left(\frac{\partial F_1}{\partial T} \right)_V + \lim_{T \to T_c^-} \left(\frac{\partial F_2}{\partial T} \right)_V, \tag{2.4}$$

which translates to the latent heat $\Delta Q = T \Delta S$. Examples are the well known cases of heat of fusion or heat of condensation. The first derivative of the free energy may also be continuous through the phase transition, and a jump will appear only in the second derivative $\partial^2 F / \partial T^2$, which is the heat capacity. These transitions are called second-order transitions [Col89, Nol02].

The idea of first-, second-, and possibly higher order transitions was introduced by Ehrenfest [Ehr33]. It was later realised that phase transitions can more conveniently be classified as discontinuous, which corresponds to first order, and continuous transitions, which corresponds to any order higher than one. The name is derived from the behaviour of the order parameter, a suitably defined quantity whose average value is zero in one phase but finite in the other. For magnetic systems, this would be the magnetisation (for ferromagnets, FM) or the sublattice magnetisation (for antiferromagnets, AF). In a discontinuous phase transition, the value of the order parameter jumps at T_c, while a gradual onset is observed for continuous transitions. A continuous phase transition always involves symmetry breaking.

In the case of discontinuous transitions, the latent heat allows for a co-existence of both phases at T_c, which also makes phenomena such as super-cooling possible. For large ΔS, the two phases will have radically different properties and the transition from one to the other proceeds from nucle-ation points. Continuous phase transitions, on the other hand, involve two phases of equal entropy at the transition. Thus, fluctuating microregions of one phase can be found in the other if the temperature is close to T_c. These order-parameter fluctuations are characterised by a typical correlation length ξ and lifetime ξ_τ, which both diverge at T_c. Due to this divergence, it is common to speak of critical fluctuations and also critical phase transitions [Col89].

The fascination of critical phenomena stems from the fact that the same concepts can be used for very diverse systems, which is called universality. The divergence of ξ and ξ_τ causes power-law behaviour of many physical properties close to the critical temperature. This is quantified by critical exponents, which are commonly defined with respect to the reduced temperature

$$t = \frac{T - T_\mathrm{c}}{T_\mathrm{c}}. \tag{2.5}$$

For small $|t|$, power-law behaviour $f(t) = t^\psi$ with a single exponent ψ is expected. For example, the critical exponent for the correlation length ξ is generally called ν and defined as

$$\xi(t) \propto t^{-\nu} \quad \text{or} \quad \xi(t) \propto (-t)^{-\nu'}, \tag{2.6}$$

if the transition temperature is approached from above or below, respectively. Analogous definitions exist for the thermodynamic exponents α (specific heat), β (order parameter, e.g. magnetisation) and γ (susceptibility). Furthermore, the exponent δ is defined for the behaviour of the order parameter at T_c as a function of (magnetic) field. Less common is the correlation function exponent η. Generally, the critical exponent ψ with respect to a property x is defined as

$$\psi = \lim_{x \to 0^+} \left(\frac{\ln f(x)}{\ln x} \right) \quad \text{or} \quad \psi' = \lim_{x \to 0^-} \left(\frac{\ln f(x)}{\ln x} \right). \tag{2.7}$$

The values of the various exponents are not independent of one another, but connected by inequality relationships on the basis of thermodynamic stability arguments.

The idea of universality is that the value for each exponent does not depend on the microscopic details of a specific system, but only on these three conditions:

- the dimensionality d of the system;

- the symmetry of the order parameter, which can often be unambiguously replaced by its dimensionality D;

- whether the effective interactions are long or short range.

If the idea of universality holds, it implies that only the simplest model within each class needs to be solved in order to know the exact solution for all possible critical transitions within that class. Often, the simplest models are magnetic models, such as the Ising model ($D = 1$), the XY

model ($D = 2$), the Heisenberg model ($D = 3$) and the spherical model ($D = \infty$). Unfortunately, even for these 'simple' models exact solutions are mostly not known. Exceptions are the case $d = 1$ (Ising's solution), which does not show a finite-temperature phase transition, the case $d = 2$, $D = 1$ (Onsager's solution), the spherical model, all cases where $d \geq 4$ and all cases where the range of the interactions is infinite. For all other models, including the most relevant case $D = 3$, only approximate solutions are known [Col89]. In the following paragraphs, a few important approaches to understanding second-order transitions are presented.

The Ginzburg-Landau model treats transitions involving symmetry breaking without explicitly considering the divergence of the correlation length. The free energy in the vicinity of T_c is expanded as a power series in the order parameter ϕ:

$$F(T, \phi) = F_0(T) + \alpha_2(T)\phi^2 + \alpha_4(T)\phi^4 + \dots \qquad (2.8)$$

Odd terms vanish, since the free energy is an even function of ϕ. The expansion is often truncated after the 4th order and $\alpha_4(T)$ assumed to be constant, which must be positive to ensure a minimum of the free energy. $\alpha_2(T)$ drives the system through the phase transition: It is proportional to $(T - T_c)$ and thus changes sign at T_c. This simple description ensures that the free energy has a minimum at $\phi = 0$ for $T > T_c$, but at $\phi > 0$ for $T < T_c$, and that the development of ϕ is continuous through the transition. The critical exponents can be evaluated by differentiating the free energy with respect to the appropriate variables.

The Ginzburg-Landau theory does not rely on any microscopic model or any further assumptions, except the validity of the above expansion around T_c. This turns out to be equivalent to assuming mean-field behaviour. Unfortunately, this condition is rarely met in reality, as it requires either spacial dimensions $d \geq 4$ or an infinite range of the interaction [Col89].

An important step towards the general understanding of critical phenomena was the concept of scaling. It is based on the assumption that the free energy is a generalised homogeneous function of temperature and field. Using the example of a paramagnet in a magnetic field, the appropriate function is $G(t, h)$ (with the dimensionless magnetic field h), and the following scaling relation is supposed to hold:

$$l^d G(t, h) = G(\tilde{t}, \tilde{h}) = G(l^y t, l^x h). \qquad (2.9)$$

Here l is the scaling factor and x and y the scaling exponents. The idea is to start with a block of length L, which contains L^d spins; L is large compared to the unit cell size a, but small compared to the correlation length ξ. If the

block size is rescaled to the length $l \cdot L$, then the functional form of the free energy should stay the same, but the variables t and h need to be rescaled to $\tilde{t} = l^y t$ and $\tilde{h} = l^x h$. Furthermore, since the correlation length is independent of the chosen cell size L, the following relation must hold:

$$l^{-1}\xi(t,h) = \xi(l^y t, l^x h). \tag{2.10}$$

From these assumptions, the scaling laws can be derived. They predict that critical exponents above and below T_c (λ and λ') are identical; furthermore, they give relations between the exponents α, β, γ, δ, ν, x and y, such that if any two exponents are known, the others can be calculated. Some of the scaling laws involve the dimensionality d; these are called hyperscaling laws. While scaling laws not containing d are supported by both theory and experiment, hyperscaling laws seem to hold only for certain dimensions [Col89].

The renormalisation group (RG) technique is based on similar ideas as scaling theory, but goes further in giving values for the critical exponents. This requires moving from the very general arguments of scaling to the explicit evaluation of Hamiltonians. The basic idea is that the Hamiltonian should keep its functional form when the system size is rescaled, and only the variables are modified to renormalised values. The approach is based on the work of Wilson, who used a reciprocal space formalism [WK74]. This typically requires evaluating a number of integrals in momentum space which include the relevant interaction terms. An increase of the system size in real space corresponds to a smaller momentum cut-off of the integrals in reciprocal space. Physically this means that as the correlation length gets large, only small momentum transfers determine the behaviour. After a certain number of renormalisation steps, a fixed point may be reached where further renormalisation does not alter the renormalised values of the variables. If a variable is rescaled to zero during this process, it is said to be irrelevant [Col89].

This explicit treatment of the Hamiltonian provides full solutions to any model, however under the condition that the integrals appearing in the model are solvable. Generally, this is the case when they are of Gaussian type, i.e. when they only contain quadratic terms; these situations correspond to mean-field behaviour, and the renormalisation group solution will reproduce the Landau exponents. The success of the method lies in the fact that non-Gaussian terms can be treated in a perturbative way, thus allowing for approximate solutions for more complicated models.

So far, only static critical exponents have been discussed. However, it was already mentioned that the critical fluctuations have a characteristic lifetime

ξ_τ, which diverges at T_c. The divergence of the correlation length and the lifetime are related via the dynamical critical exponent z by

$$\xi_\tau \propto \xi^z \tag{2.11}$$

so that the lifetime behaves as

$$\xi_\tau(t) \propto t^{-\nu \cdot z}. \tag{2.12}$$

For classical phase transitions at finite temperature, the value of z is independent of the values of the static critical exponents, since dynamics and statics decouple. There are no exact solutions for the dynamical critical exponent. However, it is assumed that universality also holds, if one further condition is added:

- z depends also on the conservation laws of the system.

This implies that z will be different for ferromagnets and antiferromagnets [Col89, HH69].

2.2 Quantum phase transitions

In the last section, phase transitions at finite temperature have been discussed. Although quantum mechanics will often be important for the formation of the ordered state (e.g., the exchange interaction), these transitions are termed classical, since quantum effects are not important for the critical behaviour. This is because the energy scale of the order-parameter fluctuations, expressed by a characteristic frequency ω_c, goes to zero close to the phase transition,

$$\hbar\omega_c \propto 1/\xi_\tau \propto t^{\nu \cdot z}, \tag{2.13}$$

while the energy scale of the thermal fluctuations stays roughly constant at $k_B T_c$. Thus, for finite T_c the immediate proximity of the transition will be dominated by thermal fluctuations.

The situation is different for a transition at $T = 0$. Here, thermal fluctuations are absent, and the critical behaviour is dominated by quantum fluctuations. Such a transition can be driven by a non-thermal control parameter r, which might be magnetic field, pressure or element substitution. The transition occurs at the critical value r_c at $T = 0$, which is called a quantum critical point (QCP). For $r > r_c$, the system is said to be quantum disordered at low temperatures, while it is in its ordered state for $r < r_c$. A finite transition temperature exists for $r < r_c$ which gradually goes to zero as r approaches r_c [Voj03]. In some cases, e.g. the case $d = 2$, $D = 3$,

long-range order at finite temperature is suppressed by fluctuations so that the ordered phase exists only at $T = 0$.

Close to a quantum critical point, critical behaviour is expected both as a function of r at $T = 0$ and as a function of T for $r = r_c$. Of course, $T = 0$ can never be realised in experiment, so that the study of quantum critical phenomena would be merely academic, if quantum effects disappeared at *any* finite temperature. However, in the vicinity of the QCP both the thermal and the quantum energy scale approaches zero, so that there will generally be an experimentally accessible temperature range where $\hbar\omega_c \gtrsim k_B T$. Thus, quantum fluctuations are important, and their dynamics will influence the critical behaviour. This is different from the classical transition, where the dynamics decouple from the static critical behaviour.

Hertz pointed out that the importance of the dynamics will reveal itself in an apparent increase of the dimensionality, since the fluctuations in time will appear as additional dimensions [Her76]. The scaling laws will involve an effective dimensionality $d_{\text{eff}} = d + z$.

Formally, quantum phase transitions are treated by analysing the properties of the order-parameter field $\Phi(q, \omega)$ for small momenta q and frequencies ω. The explicit treatment of the dynamics requires knowledge of the relevant microscopic excitations; Hertz considered itinerant magnetic systems, where the excitations are spin-waves. Looking at the transition as a function of r at $T = 0$, the second-order term of the field Φ takes the form

$$\Phi_2 = \frac{1}{2} \sum_{q\omega} (r + q^2 + \frac{|\omega|}{q})|\Phi(q, \omega)|^2 \qquad (2.14)$$

for ferromagnets, and

$$\Phi_2 = \frac{1}{2} \sum_{q\omega} (r + q^2 + |\omega|\xi_\tau)|\Phi(q, \omega)|^2 \qquad (2.15)$$

for antiferromagnets [Her76]. The difference arises due to the different damping mechanisms for FM and AF spin-waves. The forth-order term is proportional to a parameter u, which parametrises the interactions. The treatment of this field theory proceeds very similarly to the RG theory developed by Wilson, but is has one additional feature: During the renormalisation procedure, not only large momenta will be excluded from the explicit integration, but also large frequencies. While the momenta are rescaled with the scale factor l, the frequencies are rescaled by $z \cdot l$, so that the scaling procedure yields the same coefficients for both terms. This causes the dynamical critical exponent to influence the values of all other critical exponents. Equations
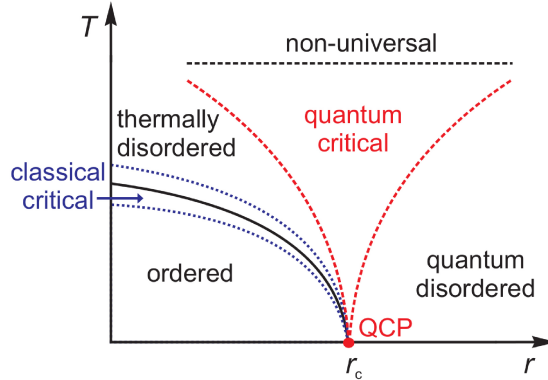
Figure 2.1: Generic r, T-phase diagram around a quantum critical point (QCP), which is located at $T = 0$ and $r = r_c$, the critical value of the control parameter. For $r < r_c$, a finite-temperature phase transition is found; it is surrounded by a classical critical region (dotted blue lines), which becomes narrower as the QCP is approached. Above the ordered region, the system is termed thermally disordered, while the region $r > r_c$ is called quantum disordered. At $r = r_c$ and finite temperatures, the system is in a quantum critical state. Its lower boundaries (dashed red lines) are given by $T \propto |r - r_c|^{\nu \cdot z}$, while the upper cut-off depends on microscopic details. Note that only the solid line represents a sharp transition, while dashed and dotted lines indicate crossover phenomena. Reproduced from [Voj03].

2.14 and 2.15 imply that $z = 3$ for the (clean) quantum ferromagnet and $z = 2$ for the quantum antiferromagnet.

While this treatment is at first sight more complex than the Wilson Ansatz for classical phase transitions, it turns out that it is actually easier to solve, since the interaction u scales to zero for many relevant situations. As mentioned above, a Gaussian theory will be valid only for $d > 4$ in the classical case, and thus in no real-world situation, but in $d_{\text{eff}} > 4$ for the quantum case, which includes $d = 2$ and $d = 3$ for ferromagnets and $d = 3$ for antiferromagnets. In these situations, mean-field or Landau exponents are predicted [Her76].

The influence of finite temperatures on the quantum phase transition has been studied by Millis [Mil93]; his treatment also allows the quantum phase transition to be analysed as a function of temperature at $r = r_c$. Technically this is done by including the temperature as an explicit parameter in the RG procedure. Solutions for the field theory can then be found for different limiting cases, where the limit $T \to 0$ is the case mainly considered by Hertz. Millis found that also for $r = r_c$ Gaussian behaviour occurs. However, the

critical exponents will not simply take the Landau values, but be dependent on z. For example, Millis derived for the temperature dependence of the correlation length in $d = 3$ [Mil93]

$$\xi^{-2} \propto T^{1+1/z}. \tag{2.16}$$

This is valid in a quantum critical cone whose limits are given by $T \propto |r - r_{\mathrm{c}}|^{\nu \cdot z}$. At higher temperature, there will be a cut-off energy scale, which is non-universal and determines the temperature range over which quantum critical behaviour can be studied experimentally. These ideas are summarised in the generic phase diagram for quantum critical points, see figure 2.1.

For $d_{\mathrm{eff}} < 4$, also the quantum phase transition will be below the critical dimension for mean-field behaviour. Since the interaction parameter u is relevant, solutions to the RG equations are more difficult to find. For the special case $d_{\mathrm{eff}} = 4$, which includes the 2-dimensional antiferromagnet, u is said the be marginal. Here, logarithmic corrections to the power-law behaviour appear in the RG solution [Mil93]; however, it has been pointed out that the RG treatment might generally not be valid for this case [LRVW07].

An alternative theoretical approach to quantum phase transitions was introduced by Moriya and Takimoto [MT95], which is called the self-consistent renormalisation (SCR) theory. Here the spin-fluctuations are described in a random-phase approximation, but allow for weak interactions between fluctuation modes. An expression for the susceptibility is derived that depends on a number of microscopic parameters, which can in principle be obtained from experiments such as neutron scattering. Critical exponents for the behaviour of the specific heat for $T \to 0$ agree with those given by Millis [Mil93] for the antiferromagnet in $d = 3$. Furthermore, Moriya and Takimoto could also derive an expression for the resistivity contribution of scattering from spin fluctuations.

Hertz and Millis developed their theories for itinerant electrons. Moriya's approach was first derived for weakly antiferromagnetic itinerant systems, but in reference [MT95] it is shown that essentially the same formalism can be used to treat 4f-based magnetism, which is more localised. This might serve as a justification for applying the Hertz-Millis theory also to 4f-based compounds. Both approaches, RG and SCR, are valid only in the paramagnetic state and make no predictions for the behaviour in the ordered phase.

In tables 2.1 and 2.2, some explicit results from the Hertz-Millis-Moriya model are given. Table 2.1 illustrates the difference between classical and quantum critical exponents, using the example of the correlation length exponent ν in 3 dimensions. Apart from the dependence on z for the quantum case, already mentioned above, there is one further striking point: In the

classical, $d = 3$			HMM, $d = 3$		
	$D = 1$	$D = 3$		$z = 2$	$z = 3$
$\xi \propto t^{-\nu}$	0.63	0.705	$\xi \propto r^{-\nu}$	0.5	0.5
			$\xi \propto T^{-\nu}$	0.75	0.666

Table 2.1: Calculations for the critical exponent ν for classical and quantum phase transitions in $d = 3$; classical values, for Ising ($D = 1$) and Heisenberg ($D = 3$) symmetry, are taken from reference [Nol02], values for the Hertz-Millis-Moriya (HMM) theory from [Mil93]. $z = 2$ corresponds to antiferromagnetic spin fluctuations, $z = 3$ to ferromagnetic spin fluctuations.

	HMM theory				Fermi
	$d = 2, z = 2$	$d = 3, z = 2$	$d = 2, z = 3$	$d = 3, z = 3$	liquid
$C/T \propto$	$\ln(1/T)$	$-T^{1/2}$	$T^{-1/3}$	$\ln(1/T)$	const.

Table 2.2: Predictions for the specific heat coefficient by the Hertz-Millis-Moriya approach [Mil93], contrasted with the behaviour expected within Fermi-liquid theory.

Hertz-Millis-Moriya theory, there is no dependence of the exponents on the dimensionality of the order parameter, i.e. whether the magnetism is of Ising or Heisenberg type.

Table 2.2 highlights another feature of quantum criticality, which has attracted much attention: The predictions for the temperature dependence are not in agreement with Fermi-liquid (FL) theory [Lan57] (see also section 2.3). In the table this is shown for the specific heat coefficient $\gamma = C/T$, which is constant at lowest temperatures for a Fermi liquid. Also other predictions of Fermi-liquid theory, e.g. the $\rho_{el} \propto T^2$ dependence of the electronic contribution to the resistivity, are often found to be violated at QCPs. It should be noted, however, that this does not imply that no well-defined electronic quasi-particles exist, but merely that the low-energy excitations associated with the quantum phase transition dominate thermodynamic and transport properties [LRVW07].

The work summarised in this section only concerns the principal publications [Her76, Mil93, MT95] that laid the groundwork for the Hertz-Millis-Moriya (HMM) theory. There has since been further development in the theoretical understanding of quantum phase transitions, both extending and contradicting its initial statements; an overview is given in [LRVW07]. An example for a further important prediction is the divergence of the Grüneisen

parameter Γ, which gives the ratio of the thermal expansion to the specific heat: While it does not diverge at a classical phase transition, Zhu and co-workers calculated that it will diverge at a quantum critical point both for $T \to 0$, $r = r_c$ and for $T = 0$, $r \to r_c$ [ZGRS03]. It thus gives a unique signature of a QCP.

Among the developments that showed the limits of the HMM scenario, two shall be mentioned here. One is the work by Kirkpatrick, Belitz and co-workers [KB03, BBGK15] who analysed the complications arising in the case of ferromagnetic quantum criticality: They predict that electronic particle-hole excitations are likely to drive a transition to be first order when it is tuned towards zero temperature. Thus, in case of ferromagnetism the quantum critical point can be avoided.

The second case is the possibility that other degrees of freedom, in addition to the magnetic order parameter, will become critical at $r = r_c$. This has in particular been discussed for a critical breakdown of the Kondo effect, which is often called local criticality since the Kondo effect is a local phenomenon [Si06, LRVW07]. In such a scenario, the critical exponents will be strongly modified from the HMM-prediction.

Furthermore, it should be mentioned that the concept of quantum criticality is not limited to magnetism; most studies, both theoretical and experimental, have focussed on magnetic transitions, but the concept is more general. A quantum critical point is expected for any second-order transition that can be tuned to $T = 0$ by a suitable tuning parameter. For example, quantum critical points have been reported for ferroelectric [RSS$^+$14] or structural transitions [GTS$^+$15].

2.3 The case of heavy-fermion compounds

This thesis is concerned with quantum criticality in heavy-fermion systems. These are intermetallic compounds containing 4f or 5f magnetic moments, which are paramagnetic at high temperature and frequently show magnetic order, mostly antiferromagnetic, at low temperatures. The ordering temperatures are often as low as ≈ 1 K and are very sensitive to pressure and magnetic field, so that they can be tuned to zero relatively easily. Thus, they are ideal model systems for the study of quantum criticality.

Heavy-fermion properties are only observed at temperatures below a characteristic energy scale, which is typically a few Kelvin. At higher temperatures, the compounds behave like local-moment paramagnets with Curie-Weiss susceptibility. For $T \to 0$, they display the following behaviour [Ful95, Mis08]:

- A linear specific heat $c_V = \gamma T$ with strongly enhanced coefficient γ, usually a factor of 100 to 1000 larger than for simple metals like lithium or sodium.

- A temperature-independent Pauli susceptibility χ_s, which is also enhanced by a factor of 100 to 1000.

- The Wilson ratio between heat capacity and susceptibility [EH00]

$$R = \frac{\pi^2 k_{\mathrm{B}}^2}{\mu_0 \mu_{\mathrm{eff}}^2} \frac{\chi_s}{\gamma} \tag{2.17}$$

  is approximately one, as for free electrons. μ_{eff} is the effective magnetic moment, k_{B} the Boltzmann constant and μ_0 the vacuum permeability.

A further, frequent observation for heavy fermions concerns the transport behaviour:

- The coefficient A of the electronic resistivity, $\rho_{\mathrm{el}} = \rho_0 + A \cdot T^2$, is very large.

These are characteristic properties of a Fermi liquid which has a strongly enhanced effective mass m^* of the quasi-particles, since $\gamma \propto m^*$, $\chi_s \propto m^*$ and $A \propto m^{*2}$. Thus they are named heavy Fermi liquids or heavy fermions.

The key to understanding the particular low-temperature properties are the strong local correlations of the f-electron site, in combination with a weak coupling to the conduction electrons. In the simplest (and very common) cases of Ce^{3+} and Yb^{3+} ions, the electron configurations are $4f^1$ and $4f^{13}$, respectively, the latter being (in first approximation) the hole analogon of the former. The f-levels are strongly localised and typically lie a few eV below the Fermi energy. The metallic character of many compounds containing Ce^{3+} and Yb^{3+} ions is usually due to the d-bands of the ligands.

An appropriate Hamiltonian to describe the coupling of localised f-levels with a conduction band is given by the Anderson model [Ful95]:

$$\begin{aligned} H & = \sum_{\mathbf{k}\sigma} \varepsilon(\mathbf{k}) c_{\mathbf{k}\sigma}^+ c_{\mathbf{k}\sigma} + \varepsilon_f \sum_m n_m^f + \frac{U}{2} \sum_{m \neq m'} n_m^f n_{m'}^f \\ & \quad + \sum_{\mathbf{k}m\sigma} [V_{m\sigma}(\mathbf{k}) f_m^+ c_{\mathbf{k}\sigma} + V_{m\sigma}^*(\mathbf{k}) c_{\mathbf{k}\sigma}^+ f_m] \end{aligned} \tag{2.18}$$

The first sum describes the kinetic energy of the (non-interacting) conduction electrons with spin σ and dispersion $\varepsilon(\mathbf{k})$, the second sum the kinetic energy of the dispersionless f-electrons, m being the z-component of the total spin

and $n_m^f = f_m^+ f_m$ the number operator for the f-site. U is the on-site interaction and $V_{m\sigma}(\mathbf{k})$ measures the interaction between conduction electrons and f-electrons. The Hamiltonian 2.18 is given for a single magnetic impurity atom; to treat a lattice of f-electrons, a summation over different f-sites has to be introduced. The single-ion Hamiltonian can be solved exactly, while approximations are required for the lattice case [Ful95].

In the following, the degeneracy of the f-level will be set to 2; this is often justified from an experimental point of view by typical values of spin-orbit coupling and crystalline electric field splitting, which are large compared to the low-temperature energy scale. Then the ground state of the f-level is a doublet, and the index m can be replaced by a spin index[1]. Furthermore, the limiting case of a large on-site interaction U and a weak coupling V is considered. Thus, the probability for a double occupancy of the f-level is completely suppressed, the f^1 configuration is stabilised and charge fluctuations are small, since they cost a lot of energy. On the low-energy scale, only spin excitations are present.

In such a situation, it is appropriate to project out the charge degrees of freedom from the treatment of the low-energy physics. This is done in a Schrieffer-Wolff transformation, which yields an effective Hamiltonian that only considers spin degrees of freedom [Ful95]:

$$H = \sum_{\mathbf{k}\sigma} \varepsilon(\mathbf{k}) c_{\mathbf{k}\sigma}^+ c_{\mathbf{k}\sigma} - 2J \mathbf{s}(0) \cdot \mathbf{S} \qquad (2.19)$$

This is called the Kondo Hamiltonian. The spin coupling constant J is given by

$$J = -\frac{V^2 U}{|\varepsilon_f|(|\varepsilon_f| + U)}, \qquad (2.20)$$

which is antiferromagnetic. Kondo has studied the properties of 2.19 by perturbation theory [Kon64], the second term forming the perturbation Hamiltonian. He found that the coupling J leads to a term proportional to $J \ln(T)$ in the low-temperature resistivity. This results in a minimum of the resistivity at a characteristic temperature, since the phonon contribution increases with temperature.

A further effect of the antiferromagnetic coupling to the conduction electrons is the compensation of the local spin for $T \to 0$ and thus to the formation of a singlet state. This happens below a temperature scale [Ful95]

$$k_{\mathrm{B}} T_{\mathrm{K}} = D \exp\left(\frac{1}{2N(0)J}\right), \qquad (2.21)$$

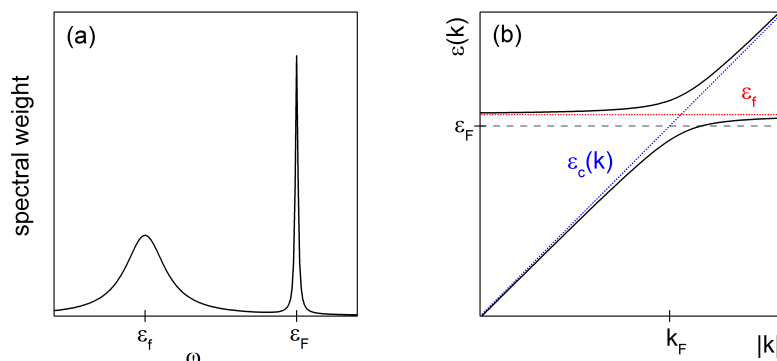[1]For cubic site symmetry, a quartet ground state is possible.

Figure 2.2: (a) Schematic representation of the spectral weight of the f-electron in a heavy-fermion compound. Note that the spectral weight of the conduction electrons is not shown in this panel. (b) Quasi-particle bands in the coherent Kondo state (solid black lines). Also shown are the energy of the Kondo resonance (dotted red line) and the dispersion of the conduction bands before hybridisation (dotted blue line), as well as the Fermi energy (dashed grey line). After reference [Ful95].

where the treatment by perturbation theory will eventually break down. T_K is the Kondo temperature, D the band width of the conduction electrons and $N(0)$ the density of states at the Fermi energy. The exponential dependence is a crucial point for heavy-fermion physics: It implies that small changes in J, which might for example be caused by the application of pressure, will have a large influence on many observable properties, which depend on the energy scale $k_B T_K$.

The solution of the single-ion Anderson Hamiltonian gives a satisfactory explanation of experimental findings in metals with dilute magnetic impurities. To understand compounds with one (or more) magnetic ions per unit cell, such as heavy-fermions, one needs to look at the Anderson lattice model. Again, the same splitting of charge and spin degrees of freedom occurs. Figure 2.2(a) illustrates this by showing schematically the spectral weight of the f-electrons in such compounds, as measured by photo emission spectroscopy. The sharp peak close to the Fermi energy is called the Kondo resonance and corresponds to spin excitations. It should be noted that an enhancement of the density of states at the Fermi level occurs also for the case of dilute impurities. However, since the concentration of f-electrons is small, the effect is not as pronounced.

Figure 2.2(a) shows only the contribution of the f-electrons to the spectral weight. For a more complete picture, the conduction electrons should also be

included. It is found that together with the Kondo resonance, quasi-particle bands form at low temperature. This is sketched in figure 2.2(b). From a cosine-like conduction electron band (which has a steep, linear dispersion around E_F) and the dispersionless f-resonance, two new bands have formed, which bend close to the Fermi energy. A gap emerges between these two bands; however, this gap arises at least partially from the mean-field approach and is expected to wash out for more thorough treatments [BPV11].

When the hybridised bands are formed, the f-electrons contribute to the Fermi volume. This will be the case at low temperatures. For $T \gg T_K$, only the conduction electron band crosses the Fermi energy. One speaks of a large and a small Fermi volume for the two limiting situations. The formation of the large Fermi volume upon lowering the temperature is not a sharp transition, but a gradual crossover [Ful95, BPV11]. When the new bands are fully formed, the respective quasi-particles form a coherent state, which displays Fermi-liquid characteristics. The shallow slope of the quasi-particle bands at E_F produces the large effective masses of the charge carriers in heavy-fermion compounds. As discussed in the beginning of this section, this is seen from the enhancement of the Pauli susceptibility and the specific heat coefficient.

Generally, the temperature below which a coherent state is formed, T_{coh}, is lower than the single-ion Kondo temperature. This leads to a typical behaviour of the resistivity, with a minimum around T_K, when Kondo scattering sets in, followed by a maximum around $T_{coh} < T_K$, when coherence is established. Below the maximum, the resistivity typically follows the Fermi-liquid expectation $\Delta\rho \propto AT^2$. Often the temperature where minimum and maximum occur are taken as experimental measures for T_K and T_{coh}. However, since both are crossover phenomena and not well separated, there is no one-to-one correspondence with definitions used in theory, such as equation 2.21. Furthermore, different experimental methods for determining these temperatures often lead to slightly different results. For example, T_K is also frequently extracted from heat capacity measurements as twice the temperature where the entropy reaches $0.5R \ln 2$ [DS82], or from spectroscopic measurements as the half-width of the Kondo resonance [CBW86]. All these measurements give similar but not identical results.

So far, interactions between the f-electrons have been neglected. This can be justified from the fact that the f-orbitals are rather localised and have little overlap with neighbouring f-orbitals or ligand-orbitals; thus, direct exchange and superexchange are usually very weak in intermetallic f-based compounds. However, the f-electrons interact with each other via the conduction electrons. This is called the Ruderman-Kittel-Kasuya-Yosida (RKKY)

interaction [Mis08]

$$H_{\mathrm{RKKY}} = -\frac{9\pi}{8} N^2(0) \frac{J^2}{\varepsilon_{\mathrm{F}}} \sum_{\langle ij \rangle} \frac{\mathbf{S}_i \cdot \mathbf{S}_j}{r_{ij}^3} \left[2k_{\mathrm{F}} \cos(2k_{\mathrm{F}} r_{ij}) - \frac{\sin(2k_{\mathrm{F}} r_{ij})}{r_{ij}} \right], \quad (2.22)$$

which describes the interaction between two localised spins $\mathbf{S}_i$ and $\mathbf{S}_j$ at distance r_{ij} through a coupling J to the conduction electrons. k_{F} is the magnitude of the wave vector at the Fermi energy ε_{F}. The coupling constant J is the same as the one appearing in the Kondo Hamiltonian. This form of the RKKY interaction was first derived by Ruderman and Kittel for the interaction of nuclear spins [RK54] and then applied to localised electron spins by Kasuya [Kas56] and Yosida [Yos57]. The cosine-dependence implies an oscillatory behaviour of the interaction, periodically changing sign with distance r. For a lattice of localised moments, the Hamiltonian 2.22 leads to a magnetically ordered ground state, which can be ferromagnetic or antiferromagnetic depending on the distances r_{ij} in the lattice.

Doniach realised that such an interaction, in a Kondo-lattice compound, is in competition with the Kondo effect [Don77]. He argued qualitatively that the competition between the Kondo energy scale, which is proportional to $\exp\left(-1/(N(0)J)\right)$, and the RKKY energy scale, which is proportional to $J^2 N(0)$, would induce a $T = 0$ phase transition from an ordered magnetic state at low J to a Kondo-state at large J. Since this transition is continuous, the ordered state close to J_{c} should have nearly-quenched ordered moments. This is indeed the situation found in many heavy-fermion compounds: Magnetic order, mostly antiferromagnetic, is found at smaller values of an experimental parameter that controls J, such as (inverse) pressure or magnetic field; the ordered moment is often substantially reduced compared to the high-temperature effective moment, which is not affected by the Kondo interaction. The size of the ordered moment scales with the transition temperature. At a critical value (pressure p_{c}, field B_{c}), quantum critical behaviour is found. On the right of the quantum critical point, the compounds enter the Fermi-liquid state.

It should be noted that the two ground states mentioned so far, i.e. the ordered state and the Fermi-liquid state, are not the only ones observed in heavy-fermion compounds. The most important of other possible ground states is superconductivity, which is frequently found close to a magnetic quantum critical point. Often, a superconducting dome appears in the J, T-phase diagram, with the maximum T_{c} at J_{c}, where the ordering temperature of the magnetic phase vanishes. The superconducting state is formed out of the heavy-fermion state, meaning that the Cooper pairs are formed by the heavy quasi-particles. This was first observed for $CeCu_2Si_2$ by Steglich and

co-workers [SAB$^+$79]. By now many other heavy-fermion superconductors are known, some without application of an external parameter, some under pressure or element substitution [Pfl09]. These superconducting phases are unconventional in the respect that the superconductivity is not mediated by phonons, but most likely by magnetic fluctuations [MPL07, Sca12].

2.4 Neutron scattering as a tool to probe critical phenomena

The neutron has an intrinsic magnetic moment and is therefore ideally suited for the study of magnetism on a microscopic level. When travelling through a sample, the spin of the neutron will interact with unpaired electrons in the sample, and might be scattered in this process. Since it is not charged, the neutron does not interact with the charge of either electrons or protons. Therefore, it has rather long mean free path of the order of 1 cm in solids, much longer than that of photons. Neutrons do, however, interact with the nuclei via the strong force, which is extremely short ranged (10^{-15} m); this can lead to either scattering or absorption of the neutron. In the following, the focus will be on scattering events, and absorption is only mentioned when necessary.

A scattering event can change both the momentum and the energy of the neutron through a transfer to or from the sample. The property of interest is the partial differential cross section, which measures the probability that a neutron with initial momentum $\mathbf{k}$ and energy E is scattered into the solid angle $\Omega + d\Omega$ with energy between E' and $E' + dE'$ [Col89]:

$$\frac{d^2\sigma_s}{d\Omega\,dE'} = \frac{k'}{k}\left(\frac{m}{2\pi\hbar^2}\right)^2 |\langle \mathbf{k}'\sigma'\Lambda'|V|\mathbf{k}\sigma\Lambda\rangle|^2\,\delta(E_\Lambda - E_{\Lambda'} + E - E'). \quad (2.23)$$

Here $\mathbf{k}'$ is the momentum of the scattered neutron, m the mass of the neutron, and Λ and Λ' are the quantum states of the scattering centre before and after scattering, with energies E_Λ and $E_{\Lambda'}$. V is the interaction potential, which depends on the type of interaction. In a typical neutron scattering experiment, the wavelength of the neutrons $\lambda = 2\pi/k$ is of the order of a few Å, so that is is compatible with lattice spacings in solid. Their energy $E = \hbar^2 k^2/(2m)$ is in the meV range, like many elementary excitations of condensed matter. Photons of the same momentum have energies that are six orders of magnitude larger. Inelastic scattering events are therefore much easier to detect with neutrons.

In case of nuclear scattering, the interaction potential can be approximated by the Fermi pseudopotential

$$V = \frac{2\pi\hbar^2}{m}\,b\,\delta(\mathbf{r} - \mathbf{R}), \quad (2.24)$$

with the nuclear scattering length b and the positions $\mathbf{r}$ and $\mathbf{R}$ of the neutron and the nucleus, respectively. The delta function gives a good approximation, since the wavelength of the neutron is much larger than the radius of the nuclei. The wave functions of the neutron before and after scattering can be described by the plane waves $\exp(i\mathbf{k} \cdot \mathbf{r})$ and $\exp(i\mathbf{k}' \cdot \mathbf{r})$, so that the matrix element $\langle \mathbf{k}'|V|\mathbf{k}\rangle$ will be proportional to $\exp(i\boldsymbol{\kappa} \cdot \mathbf{R})$, with the scattering vector $\boldsymbol{\kappa} = \mathbf{k} - \mathbf{k}'$. For an array of nuclei at positions $\mathbf{R}_j$ with scattering length b_j, equation 2.23 then takes the form:

$$\frac{d^2\sigma_s}{d\Omega\,dE'} = \frac{k'}{k}|\langle \Lambda'|\sum_j b_j \exp(i\boldsymbol{\kappa} \cdot \mathbf{R}_j)|\Lambda\rangle|^2\,\delta(E_\Lambda - E_{\Lambda'} + E - E'). \quad (2.25)$$

Here it has been assumed that the scattering is independent of the spin state, or that the spin state dependence can be incorporated in b_j.

The scattering length b_j is a constant. However, its value depends not only on the element, but also the isotope, because the neutron interacts with all nucleons. Indeed, the scattering lengths of various isotopes of the same element can differ drastically and even have opposite sign. Furthermore, if the nucleus has a non-zero spin, the scattering length also depends on its relative orientation to the spin of the neutron. For both isotope distribution and nuclear spin states, a random distribution is assumed. With the definition $F_j = \langle \Lambda'|\exp(i\boldsymbol{\kappa} \cdot \mathbf{R}_j)|\Lambda\rangle$, the effect of randomness on the matrix elements can be formalised as follows [Col89]:

$$\begin{aligned}
|\langle \Lambda'|\sum_j b_j \mathrm{e}^{i\boldsymbol{\kappa}\cdot\mathbf{R}_j}|\Lambda\rangle|^2 &= \sum_{jl} b_j b_l F_j F_l^* \\
&= \sum_{jl,j\neq l}(\bar{b})^2 F_j F_l^* + \sum_j \bar{b^2} F_j F_l^* \\
&= (\bar{b})^2\sum_{jl} F_j F_l^* + (\bar{b^2} - (\bar{b})^2)\sum_j F_j F_l^*. \quad (2.26)
\end{aligned}$$

In the second line, the sum is split up into one part that contains all terms with $j \neq l$, and one sum with $j = l$. In the first term, the square of the mean value of b is taken, while in the latter the mean of the square of b appears. In the third line, the term $j = l$ is re-inserted into the first sum and then needs to be subtracted from the second sum. $(\bar{b})^2\sum_{jl} F_j F_l^*$ is called the coherent contribution to scattering, while $(\bar{b^2} - (\bar{b})^2)\sum_j F_j F_l^*$ is the incoherent term, which causes a constant background at all scattering angles. Values of $b_{\mathrm{coh}} = \bar{b}$ and $b_{\mathrm{inc}} = \sqrt{\bar{b^2} - (\bar{b})^2}$ for all elements can be found in tables, e.g. reference [Neu03].

The interaction potential for magnetic scattering takes a slightly more complicated form, since the interaction is not point-like. The neutron's magnetic moment $\boldsymbol{\mu}_n$ interacts with the magnetic field $\mathbf{B}$ of an unpaired electron via [Col89]

$$V = -\boldsymbol{\mu}_n \cdot \mathbf{B} = \boldsymbol{\mu}_n \cdot \frac{\mu_0}{4\pi} \left[\left(\text{curl} \frac{\boldsymbol{\mu}_e \times \mathbf{R}}{|\mathbf{R}|^3} \right) - \frac{2\mu_B}{\hbar} \frac{\mathbf{p} \times \mathbf{R}}{|\mathbf{R}|^3} \right]. \qquad (2.27)$$

μ_0 is the vacuum permeability, μ_B the Bohr magneton, $\boldsymbol{\mu}_e$ the magnetic moment of the electron and $\mathbf{R}$ and $\mathbf{p}$ its position and momentum. The first term in the brackets describes the field due to the electron spin and the second term the field due to its orbital motion. Inserting the magnetic interaction potential into the partial differential cross section 2.23 leads to [Col89]

$$\frac{d^2\sigma_s}{d\Omega\, dE'} = \left(\frac{\gamma\mu_0 e^2}{4\pi m_e} \right)^2 \frac{k'}{k} |\langle \sigma'\Lambda'|\boldsymbol{\sigma} \cdot \mathbf{Q}_\perp|\sigma\Lambda\rangle|^2\, \delta(E_\Lambda - E_{\Lambda'} + E - E'), \quad (2.28)$$

with the elementary charge e and the electron mass m_e. $\mathbf{Q}_\perp$ is the component of a vector $\mathbf{Q}$ perpendicular to the scattering vector $\boldsymbol{\kappa}$, with $\mathbf{Q}$ defined by

$$2\mu_B \mathbf{Q} = \int \mathbf{M}(\mathbf{r}) \exp(i\boldsymbol{\kappa} \cdot \mathbf{r}) d\mathbf{r}, \qquad (2.29)$$

the Fourier transform of the magnetisation density $\mathbf{M}(\mathbf{r})$, which is also known as the magnetic form factor $f(\boldsymbol{\kappa})$.

The cross sections 2.25 and 2.28 will now be expressed via the nuclear and magnetic correlation functions. First the scattering function $S(\boldsymbol{\kappa}, \omega)$ is introduced, so that equation 2.25 becomes

$$\begin{aligned}
\frac{d^2\sigma_s}{d\Omega\, dE'} &= \frac{k'}{k} N b^2 S(\boldsymbol{\kappa}, \omega), \\
S(\boldsymbol{\kappa}, \omega) &= \frac{1}{N} \sum_\Lambda p_\Lambda \sum_{\Lambda'} |\langle \Lambda'| \sum_j e^{i\boldsymbol{\kappa}\cdot\mathbf{R}_j} |\Lambda\rangle|^2 \delta(E_\Lambda - E_{\Lambda'} + \hbar\omega), (2.30)
\end{aligned}$$

where $\hbar\omega = E - E'$. N is the number of nuclei, which are assumed to have the same scattering length b for simplicity, and p_Λ is the probability to find the system in state Λ initially. Now the delta function in energy is replaced by an integration over time τ, and time-dependent operators and the operator expectation value

$$\langle \mathbf{O} \rangle = \sum_\Lambda p_\Lambda \langle \Lambda|\mathbf{O}|\Lambda\rangle \qquad (2.31)$$

are introduced. Then the scattering function can be written as [Col89]

$$S(\boldsymbol{\kappa}, \omega) = (hN)^{-1} \sum_{jl} \int_{-\infty}^{\infty} \exp(i\omega\tau)d\tau$$
$$\times \langle \exp(-i\boldsymbol{\kappa} \cdot \mathbf{R}_l(0)) \exp(-i\boldsymbol{\kappa} \cdot \mathbf{R}_j(\tau)) \rangle. \qquad (2.32)$$

The term in the second line is the nuclear correlation function; it states mathematically how strongly the position $\mathbf{R}_j(\tau)$ of atom j at time τ is linked to the position $\mathbf{R}_l(0)$ of atom l at time zero. The separation into a coherent and an incoherent part can also be done within the correlation-function formalism; the incoherent part will then contain an auto-correlation function.

An analogous expression can be derived for the magnetic scattering function [Col89]:

$$S^{\alpha\beta}(\boldsymbol{\kappa}, \omega) = (2\pi N)^{-1} \sum_{jl} \exp(i\boldsymbol{\kappa} \cdot (\mathbf{R}_j - \mathbf{R}_l))$$
$$\times \int_{-\infty}^{\infty} \exp(i\omega\tau) \langle S_{l\alpha}(0) S_{j\beta}(\tau) \rangle d\tau. \qquad (2.33)$$

In this notation, the partial differential cross section for magnetic scattering is given by

$$\frac{d^2\sigma_s}{d\Omega\, dE'} = \frac{k'}{k} \frac{N}{\hbar} \left(\frac{\gamma\mu_0 e^2}{4\pi m_e} \right)^2 |f(\boldsymbol{\kappa})|^2 \sum_{\alpha\beta} (\delta_{\alpha\beta} - \hat{\kappa}_\alpha \hat{\kappa}_\beta) S^{\alpha\beta}(\boldsymbol{\kappa}, \omega). \qquad (2.34)$$

The proportionality of the neutron scattering signal to the spin-spin correlation function is a crucial point for the study of critical phenomena. It means that both the correlation length ξ and the correlation time ξ_τ can be directly measured. In this thesis, it is generally assumed that the correlation function decays exponentially in space ($\propto \exp(-|\mathbf{R}|/\xi)$) and time ($\propto \exp(-\tau/\xi_\tau)$), so that Lorentzian functions are expected for measurements in inverse space and in the frequency domain. However, the correlation function in real space might have a more complicated dependence on ξ, particularly for $d \neq 3$ [Col89]. Such effects will be disregarded in this work.

In a crystalline lattice, the atomic positions are correlated over infinite length and time scales. The scattering cross section therefore involves two delta functions: $\delta(\hbar\omega)$, which implies $E = E'$ and $|\mathbf{k}| = |\mathbf{k}'|$, and $\sum_{\mathbf{g}} \delta(\boldsymbol{\kappa} - \mathbf{g})$, which implies $\boldsymbol{\kappa} = \mathbf{k} - \mathbf{k}' = \mathbf{g}$, with the reciprocal lattice vector $\mathbf{g} = (hkl)$. In this situation, the following equality holds:

$$g = 2k \sin\theta \quad \text{or} \quad \lambda = 2d \sin\theta, \qquad (2.35)$$

which is known as Bragg's law. θ is half the angle enclosed between $\mathbf{k}$ and $\mathbf{k}'$ and d the lattice spacing given by $d = 2\pi/g$.

Bragg's law is also fulfilled for the case of magnetic scattering inside a magnetically ordered state, giving rise to magnetic Bragg peaks at $\mathbf{g} \pm \tau$, with the magnetic ordering vector $\tau = (\tau_h\ \tau_k\ \tau_l)$. For ferromagnetic order, $\tau = 0$, so that the positions of magnetic and nuclear Bragg peaks coincide. For antiferromagnetic order, the nuclear and the magnetic unit cell are generally not identical, and magnetic Bragg peaks appear at $(h \pm \tau_h\ k \pm \tau_k\ l \pm \tau_l)$. If all τ_i can be expressed as rational numbers, the order is called commensurate, otherwise one speaks of incommensurate order.

For inelastic scattering, the measured intensity depends on the occupation probability of the initial quantum state of the respective excitation. This is expressed in the Bose factor

$$n(\hbar\omega) + 1 = \frac{1}{1 - \exp(-\hbar\omega/(k_\mathrm{B}T))} \tag{2.36}$$

with the Boltzmann constant k_B. The term $\omega \cdot (n(\hbar\omega) + 1)$ is often called detailed balance [Col89]. For $k_\mathrm{B}T \gg |\hbar\omega|$, excitations are thermally populated, and the Bose factor has approximately the same value for ω and $-\omega$. Then the spectrum will look symmetric with respect to $\omega = 0$. For $k_\mathrm{B}T \ll |\hbar\omega|$, the Bose factor goes to zero for negative energy transfers: The system is in its ground state and cannot be de-excited.

To close this section, a brief description of the instruments is given which are used for the measurement of critical scattering [FMS09].

- Neutron sources: Experiments with neutrons require beams of large flux (neutrons per second per unit area). These can be produced either by nuclear reactors, where the neutrons are emitted during the fission of uranium nuclei, or by spallation sources, where a target of heavy elements, e.g. lead, is bombarded with high-energy protons, which leads to the evaporation of nucleons from the excited nuclei. A spallation source usually works in pulses with a frequency of a few 10 Hz, due to the periodical acceleration of the protons. Nuclear fission produces a continuous neutron beam, as long as a stable chain reaction is running in the reactor.

  Both fission and spallation produce high-energy neutrons which are not suitable for research with condensed matter. Therefore, they are thermalised in a moderator, usually water or heavy water, which is roughly at room temperature. These thermal neutrons will then have a Maxwellian wavelength distribution with a mean energy of $k_\mathrm{B} \cdot 300\mathrm{K}$, which peaks around $\lambda = 1$ Å. If larger or smaller wavelengths are

needed for experiments, a so-called cold source (liquid hydrogen) or hot source (heated graphite) can be used for thermalisation.

Neutrons leave the source via exit slits. To accommodate many experimental set-ups at one source, the instruments are often situated at a considerable distance, several or even a few dozen meters, from the source. To prevent flux losses according to $I \propto r^{-2}$, neutrons fly through special guides whose surfaces reflect neutrons via total reflection at small angles. Relatively large critical angles (a few degrees) can be achieved by multilayer materials, which are made from alternating layers of, e.g., Ni and Ti.

- Monochromators, analysers and detectors: A neutron beam at the end of a neutron guide has a Maxwellian energy distribution. However, many experiments require monochromatic beams with a defined incident energy. These can be produced in two different ways: Either, a certain wavelength is reflected out of the initial beam by Bragg reflection from a suitable crystal or crystal array. To fulfill the Bragg condition 2.35, at different wavelengths λ, the crystal can be rotated around an axis perpendicular to the beam. A general problem exists for this type of monochromator, which is that Bragg scattering occurs also for $\lambda/2$, $\lambda/3$ and so on. These contributions need to be filtered out of the beam by materials which are opaque for neutrons of wavelength λ, but absorb neutrons of wavelength $\lambda/2$ and smaller. Monochromator crystals are generally used at continuous neutron sources.

  The second way to produce a monochromatic beam, mainly employed at pulsed sources, are disk choppers which rotate around an axis parallel to the beam. They are coated with a neutron-absorbing material, so that neutrons can only pass through slits in the disks. A set of two or more choppers are placed successively in the beam and rotated at the same speed but with a phase difference between their opening and closing periods; this ensures that only neutrons of a certain velocity can pass. The energy of the monochromatic beam may be varied by changing the rotation speed of the choppers. Instead of a set of choppers, it is also possible to use a single drum that has long slits curved around its rotation axis, so that again the flight path of the neutrons needs to match the rotation speed; this is called a velocity selector. It can also be used in combination with a crystalline monochromator to suppress $\lambda/2$ contamination.

  Monochromator crystals are also used to analyse the energy of the beam scattered by the sample, and then are called analysers.

The detection of neutrons requires isotopes with a large cross section for nuclear reactions with thermal neutrons. The most important are ^{3}He, ^{10}B and ^{6}Li. The reactions cause ionising radiation to be emitted, and the ionisation products can be detected by conventional electronics such as Geiger counters (for gas detectors) or photo multipliers (solid scintillation detectors). The same detection principle is used for neutron monitors, which measure the flux to the sample; however, while detectors are optimised to count every incoming neutron, monitors should be insensitive and only react with a small fraction of the passing neutrons.

- Diffractometer: A diffractometer measures the differential cross section

$$\frac{d\sigma_s}{d\Omega} = \int_{-\infty}^{\infty} \frac{d^2\sigma_s}{d\Omega dE'} dE'. \tag{2.37}$$

This means that the scattered neutrons are detected irrespective of their energy and only their scattering angle is analysed. In most cases, the above integral will be dominated by elastic scattering $\hbar\omega = 0$, so that diffractometers are mainly used for the study of crystal or magnetic structures. However, also diffuse scattering from short-lived and short-ranged correlations will be visible. Inelastic scattering, for example from phonons, appears as an enhanced background in the diffractogram.

A typical powder diffractometer at a continuous neutron source uses monochromatic neutrons, so that every reciprocal lattice vector **g**, or lattice spacing d_{hkl}, gives rise to a peak at the respective scattering angle 2θ. This requires a bisecting geometry, which can generally be assumed to be fulfilled for all vectors **g** due to the random arrangement of the crystallites in a powder sample. The scattering intensity as a function of angle 2θ is usually measured with a detector bank, which can measure a large range of angles simultaneously. This is called an angular-dispersive diffractometer. At a pulsed source, it is more efficient to use a white beam and distinguish the reflections via energy dispersion.

In a single crystal, only few vectors **g** fulfill the bisecting geometry for any orientation of the crystal to the beam if a monochromatic beam is used. Thus, it is generally not necessary to have a detector bank, and instead a single counter detector is used, that can be driven to different 2θ angles. To measure a large number of reflections, the sample needs to be rotated in the beam on a goniometer. The most flexible goniometers allow the sample to be brought to any possible angle with
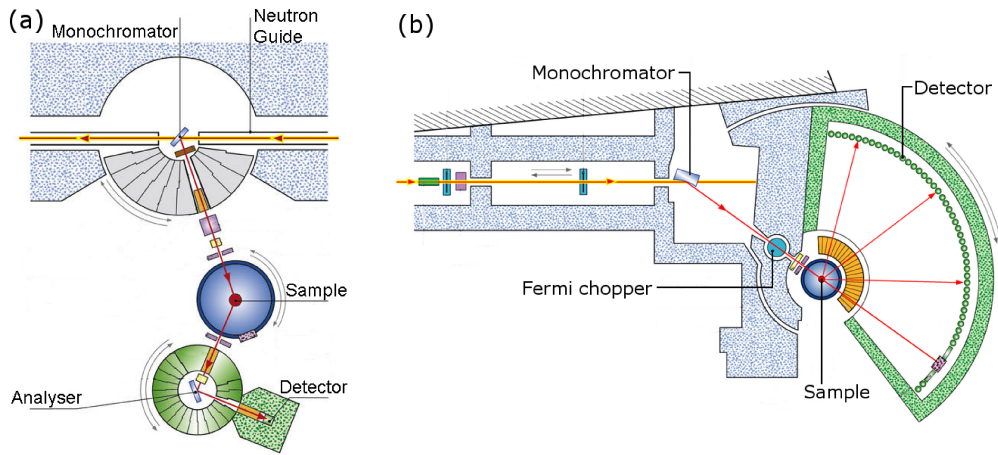
Figure 2.3: (a) Schematic set-up of the triple-axis spectrometer IN14 at ILL, Grenoble. (b) Schematic set-up of the time-of-flight spectrometer IN4 at ILL, Grenoble. Pictures taken from www.ill.eu.

respect to the beam. Alternatively, the sample can be kept in a fixed position, and a white incident beam is used for the measurement of the diffractogram. Thus, multiple reflections can be measured simultaneously, since different **g** match different λ. This latter instrument is called a Laue diffractometer.

- Triple-axis spectrometer: A triple-axis spectrometer works in principle similarly to a single crystal diffractometer, but analyses the energy of the scattered beam in addition to the scattering angle. The name is derived from the three axes monochromator - sample - analyser. They each have two characteristic angles, the rotation of the crystal around an axis perpendicular to the beam, and the 2θ angle between incoming and outgoing beam. A goniometer with additional axes for the sample will increase the flexibility of the measurement; if no further axis exists, only reflections within the scattering plane can be measured. A triple-axis spectrometer can be operated in two modes: Either, the monochromator settings and thus the incoming wavelength λ_i are fixed, and the energy of the outgoing beam is analysed by varying the analyser settings; or the analyser is set to a fixed final wavelength λ_f and the settings of the monochromator are varied to scan energy transfers. In either setting, the magnitude of λ_i or λ_f determines the resolution of the experiment.

- ToF spectrometer: A time-of-flight (ToF) spectrometer measures the

energy of the scattered neutrons through their velocity $v = h/(m\lambda)$, i.e. their flight time τ over the known distance L from sample to detector. This requires that the velocity of the neutrons before scattering is known, i.e. a monochromatic beam, as well as knowing the time when they were scattered by the sample; to achieve this, neutrons must arrive in pulses. At a spallation source, this naturally is the case. At a nuclear reactor, the continuous beam is cut into pulses by a Fermi chopper. ToF spectrometers are usually equipped with a detector bank covering a large angular segment. A ToF dataset thus consists of intensities $I(2\theta, \tau)$ for each pulse, which needs to be converted into energy and momentum transfer via

$$\hbar\omega(\tau) = \frac{mL^2}{2} \frac{\tau^2 - \tau_0^2}{\tau^2 \tau_0^2} \tag{2.38}$$

and

$$Q = \frac{mL}{\hbar} \sqrt{\frac{\tau^2 + \tau_0^2 - 2\tau_0\tau \cos(2\theta)}{\tau^2 \tau_0^2}}. \tag{2.39}$$

τ_0 is the flight time of an elastically scattered neutron.

In table 2.4, a short overview of the instruments used in this thesis is given.

instrument (source)	wavelength	sample(s)	sample environment
Triple-axis spectrometers (samples single crystals)			
IN12 (ILL)	$\lambda_f = 5.45$ Å	$CeCu_2Si_{1.96}Ge_{0.04}$	dilution cryostat
IN14 (ILL)	$\lambda_f = 5.45$ Å	$CeCu_2Si_2$	dilution cryostat $B_{max} = 2.5$ T
IN12 (ILL)	$\lambda_f = 5.45$ Å	$CeCu_2Si_{1.96}Ge_{0.04}$	dilution cryostat
V2 (HZB)	$\lambda_f = 4.19$ Å and 5.61 Å	$CeCu_2Si_{1.96}Ge_{0.04}$	dilution cryostat $B_{max} = 5$ T
Single-crystal diffractometers (samples single crystals)			
D10 (ILL)	$\lambda = 2.36$ Å	CePdAl	^{4}He flow cryostat
D10 (ILL)	$\lambda = 2.36$ Å	CePdAl	^{4}He bath cryostat
RESI (FRM2)	$\lambda = 1.03$ Å	CePdAl	^{3}He cryostat
E4 (HZB)	$\lambda = 2.45$ Å	$CePd_{0.9}Ni_{0.1}Al$	^{3}He cryostat
E4 (HZB)	$\lambda = 2.45$ Å	CePdAl $CePd_{0.9}Ni_{0.1}Al$ $CePd_{0.95}Ni_{0.05}Al$	^{3}He cryostat
Time-of-Flight spectrometers (powder samples)			
IN4 (ILL)	$\lambda_i = 1.5$ Å and 3.0 Å	$YbNi_4P_2$ $LuCo_4Ge_2$	^{4}He bath cryostat
FOCUS (PSI)	$\lambda_i = 5$ Å	$YbNi_4P_2$	dilution cryostat
ToFToF (FRM2)	$\lambda_i = 5$ Å	$YbNi_4P_2$	dilution cryostat

Table 2.3: Neutron scattering instruments used in this work. The neutron sources at ILL (Institut Laue-Langevin), HZB (Helmholtz-Zentrum Berlin) and FRM2 (Forschungsreaktor München 2) are reactor sources, at PSI (Paul Scherrer Institut) a spallation source is operated. All magnetic fields are applied vertically to the scattering plane. For triple-axis spectrometers, the wavelength λ_f refers to the scattered (final) neutron beam, since it is constant during the experiment. For Time-of-Flight spectrometers the wavelength of the initial neutron beam, λ_i, is given instead. Further details to the experimental set-ups can be found in the respective chapters.

Chapter 3

Various ground states of CeCu$_2$Si$_2$ studied by inelastic neutron scattering

3.1 The compound CeCu$_2$(Si$_{1-x}$Ge$_x$)$_2$

CeCu$_2$Si$_2$ is a model compound among the heavy fermions in at least two respects: First, it shows an antiferromagnetic quantum critical point that can be well described by the standard scenario proposed by Hertz, Millis and Moriya [Her76, Mil93, MT95], both thermodynamically [SS11] and from a microscopic point of view [ASS$^+$11]. Second, it was the first heavy-fermion superconductor ever discovered [SAB$^+$79]. The superconductivity and its relation to the magnetic phase remain intensively studied, particularly in comparison to cuprate- and pnictide-superconductors. Even though the latter have much higher transition temperatures, the mechanism behind the superconductivity is presumed to be of magnetic origin in all three compound classes [Sca12].

Although the superconducting phase [SAB$^+$79] as well as the Kondo characteristics [ABMC84] of CeCu$_2$Si$_2$ have been known for several decades, systematic studies of the low-temperature properties have long been problematic due to a strong dependence of the results on the sample: Different samples of seemingly similar composition have displayed very different properties. Later it was discovered that the ground state is highly sensitive to the exact ratio of Cu to Si, and can be tuned by using an excess of either in the synthesis [SGG$^+$96, SDJ$^+$10]: Si-rich samples have an antiferromagnetic ground state ('A-type'), while Si-deficient samples become superconducting ('S-type'), and samples with a Cu-Si ratio very close to 1 might show both phenomena, with $T_N > T_c$ ('A/S-type'). The schematic phase diagram is shown in figure 3.1;
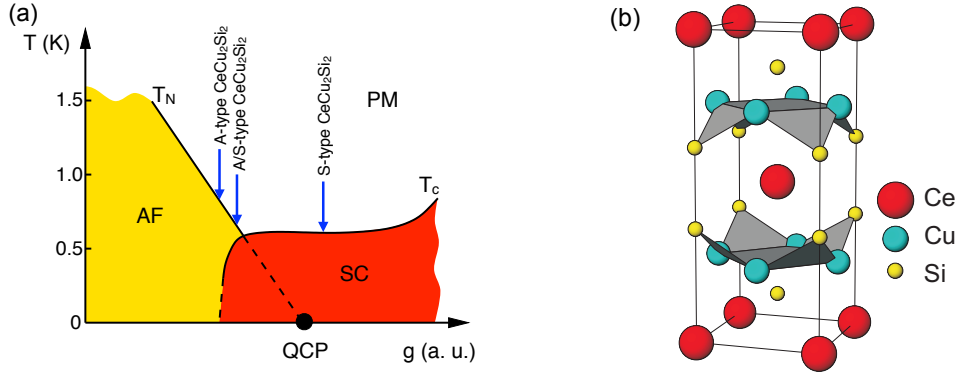
Figure 3.1: (a) Schematic phase diagram of CeCu$_2$Si$_2$. The coupling g can be tuned by varying the Cu:Si ratio, or by pressure (details see text). (b) Crystallographic unit cell of CeCu$_2$Si$_2$. Images by Oliver Stockert.

the figure also includes an image of the unit cell of CeCu$_2$Si$_2$, which crystallises in the tetragonal ThCr$_2$Si$_2$ structure. Typical transition temperatures are $T_N \approx 0.8$ K and $T_c \approx 0.6$ K, and the critical magnetic field for suppressing the superconductivity in S-type CeCu$_2$Si$_2$ is $B_{c2} = 1.7$ T [ASS$^+$11].

Pressure and germanium substitution can serve as further tools to tune the properties of CeCu$_2$Si$_2$. The isoelectronic substitution of Ge for Si acts as negative pressure, which stabilises antiferromagnetism, while pressure suppresses magnetism. Apart from the superconducting dome at the antiferromagnetic quantum critical point (see figure 3.1), another dome is observed at larger pressures, which is assumed to be related to valence fluctuations [YGD$^+$03, SS11]. In this work, all measurements were done under ambient pressure, so that they only relate to the first superconducting dome. Some of the samples in this study were doped with 2% Ge. It has been suggested that superconductivity and magnetism can coexist in Ge-doped samples [KIO$^+$02], while they compete in CeCu$_2$Si$_2$ [FAG$^+$97, FSS$^+$07]. However, data by Arndt *et al.* indicate that samples with low Ge content behave like undoped CeCu$_2$Si$_2$ [ASB$^+$09, Arn10].

The possibilities to investigate the quantum-critical fluctuations and the interplay of magnetism and superconductivity on a microscopic level were largely improved by the discovery of the antiferromagnetic ordering vector of CeCu$_2$Si$_2$: Stockert *et al.* found magnetic Bragg peaks at the incommensurate position $\tau = (0.22\ 0.22\ 0.52)$, which could be shown to be due to Fermi-surface nesting by comparison to renormalised band structure calculations [SFZ$^+$04]. Additionally, the growth of single crystals has made significant advances in recent years, so that large crystals are available which allow in-

elastic neutron experiments. Several spectroscopic measurements have been performed in the last years, most notably the study of the spin fluctuations in S-type CeCu$_2$Si$_2$ [SAF$^+$11, ASS$^+$11], which is located close to the quantum critical point.

In this chapter, several remaining questions of the inelastic response of CeCu$_2$Si$_2$ are addressed: First, the magnetic excitations of an A-type crystal are presented and compared to those of the S-type sample. Then, the study of the critical fluctuations of S-type CeCu$_2$Si$_2$ is extended to the Q-dependence of the response. In the last part, spectra of A/S-type CeCu$_2$Si$_2$ are presented, which had not been previously measured. Before the neutron data are discussed, some details will be given about the crystal growth of the A-type and the A/S-type sample, which I have synthesised for the purpose of inelastic neutron scattering experiments.

3.2 Crystal growth of CeCu$_2$(Si$_{1-x}$Ge$_x$)$_2$

Single crystal synthesis of CeCu$_2$Si$_2$ and CeCu$_2$(Si$_{1-x}$Ge$_x$)$_2$ has been established at the MPI CPfS in the group of Christoph Geibel. Using copper flux and a Bridgman-type furnace, single crystals of around 2 g could be synthesised. Hirale S. Jeevan has performed a systematic study on the influence of the composition of the starting materials on the properties of the resulting crystals [Jee10]. The S-type CeCu$_2$Si$_2$ crystal (2.0 g) used in the measurement of section 3.4 originated from these experiments. However, neither the size of the crystals nor their exact composition can be controlled very accurately. The stoichiometry of the starting materials will only make the formation of certain ground states more likely, but does not directly relate to the composition of the crystals formed during synthesis. Therefore, several attempts of synthesis might be necessary to get a large single crystal of a desired type.

With the aim of making a large single crystal of A/S-type, I have synthesised five batches of CeCu$_2$(Si$_{1-x}$Ge$_x$)$_2$. Initially, I used the starting composition Ce$_{0.95}$Cu$_2$Si$_2$, as suggested by Hirale S. Jeevan for A/S-type crystals [Jee10]. Later I also tested the influence of substituting germanium for silicon and of varying the cerium content. Similarly, the furnace parameters for the crystal growth were initially taken from Jeevans work and then slightly modified. A survey of the composition as well as some details of the synthesis for all batches can be found in table 3.1. Generally, the synthesis followed the same steps: First, the elements were weighted according to the desired starting composition and melted in an arc furnace to give a polycrystalline pellet. Due to the large total mass of the ingot (30/50 g), this was done separately for fractions of the sample of $\approx$ 6 g. These pellets were then crushed

and filled into a cylindrical Al$_2$O$_3$ crucible, together with copper shot which serves as flux in the synthesis (sample:copper 60:40 [mol]). The crucibles had a conical shape at the bottom to facilitate the growth of the first crystals in the melt. To protect the sample from oxidation, the crucible was closed with a lid and the lid wrapped in Zr foil. Then, the crucible was placed into a Bridgman furnace, which was heated to 1530°C (1510°C for batch 83104) at 150°C/h. This resulted in a sample temperature—measured at the bottom of the crucible—of 1540°C (1525°C). Keeping the furnace at constant temperature, the sample was then cooled by moving the hot zone of the furnace up. Thus, the bottom tip of the crucible is always the coldest point of the melt. After leaving the sample at maximum temperature for half an hour, the sample was cooled rapidly by about 20°C by moving the furnace at high speed.[1] Then, the furnace is moved very slowly to achieve an initial cooling speed of around 0.75°C/h. When the sample reaches approximately 1200°C, furnace and sample are cooled to room temperature at 150°C/h. In total, the crystallisation takes around one week. The slow cooling process should not only result in good crystallisation conditions but also allows for in-situ annealing. When cooled down, the single crystals can be separated mechanically from the flux and from polycrystalline material.

For all batches, the heat capacity was measured for approximately five different samples. These always included the largest single crystal(s) of the batch as well as a few others from different positions in the crucible. Generally, crystals from the same batch showed a large variety of sizes, properties and ordering temperatures. EDX (energy-dispersive x-ray spectroscopy) spectra and XRD (x-ray diffraction) patterns were measured for one crystal of each batch to confirm the formation of CeCu$_2$(Si$_{1-x}$Ge$_x$)$_2$. The accuracy of EDX does not allow for a precise determination of the Ce:Cu:(Si,Ge) ratio so that all crystals will be referred to as having stoichiometry CeCu$_2$Si$_2$ or CeCu$_2$(Si$_{0.98}$Ge$_{0.02}$)$_2$.

Summing up the experiences gained from all batches, it seems easier to make A/S-type crystals when a small amount of germanium is added. However, since germanium substitution stabilises the antiferromagnetic ground state, the cerium content should be slightly higher than Jeevan's suggestion of 95% for CeCu$_2$Si$_2$. For obtaining large single crystals it appears that thorough melting is crucial: For batch 83101 the crystallisation process seems to have been too fast, and for batch 83104 the initial temperature was probably too low. The largest single crystals could be obtained from batches 83102 and

---

[1]For the first three batches, rapid cooling was done by moving the furnace at speed 0, which takes around one minute. For the later two, the furnace was moved at speed 1, which takes over an hour; then, the waiting period of 30 minutes was omitted.

sample number, nominal composition	sample mass, flux mass	growth conditions	largest crystal
83101 Ce$_{0.95}$Cu$_2$Si$_2$	49.97 g 6.69 g	1540°C to 1516°C (fast) to 1160°C in 170 h	0.6 g
83102 Ce$_{0.95}$Cu$_2$Si$_{1.96}$Ge$_{0.04}$	29.96 g 3.99 g	1540°C to 1519°C (fast) to 1170°C in 167 h melted twice	3.5 g
83103 Ce$_{0.95}$Cu$_2$Si$_2$	29.94 g 4.02 g	1543°C to 1524°C (fast) to 1175°C in 186 h new thermocouple	1.7 g
83104 Ce$_{0.975}$Cu$_2$Si$_{1.96}$Ge$_{0.04}$	29.96 g 3.95 g	1525°C to 1500°C (fast) to 1100°C in 187 h	0.9 g
83105 Ce$_{0.975}$Cu$_2$Si$_{1.96}$Ge$_{0.04}$	29.98 g 3.95 g	1540°C to 1522°C (fast) to 1214°C in 168 h melted twice	4.5 g

Table 3.1: Details of the synthesis of CeCu$_2$(Si$_{1-x}$Ge$_x$)$_2$, aimed at making large single crystals for neutron scattering. For a description of the synthesis procedure, see main text.
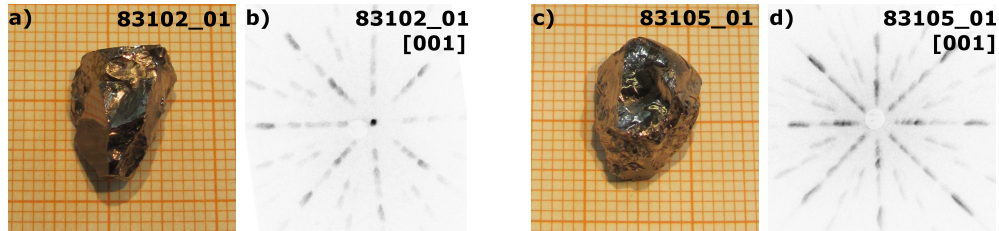

Figure 3.2: Single crystals for neutron scattering. a,c: Photos of the samples; b,d: Neutron Laue backscattering images, for incident neutron beam along the *c*-axis, taken at Orient-Express at ILL, Grenoble. a and b show the sample 83102_01, an A-type crystal of composition CeCu$_2$(Si$_{0.98}$Ge$_{0.02}$)$_2$, and c and d show sample 83105_01, an A/S-type crystal of the same nominal composition.

83105, which were both accidentally melted twice: After heating to 1540°C, the engine of the furnace failed during synthesis 83102, and a power cut occurred during synthesis 83105. Thus, the samples cooled completely before the synthesis could be restarted and proceeded as described.

From these two batches, three large single crystals, suitable for inelastic neutron scattering, were synthesised: 83102_01, an A-type single crystal of 3.5 g; 83105_01, an A/S-type single crystal of 4.5 g; 83105_02, an S-type single crystal of 3.3 g (masses before polishing). The first and the second were used for the neutron scattering experiments presented in section 3.3 and 3.5, respectively. Their pictures as well as neutron Laue images are shown in figure 3.2. The third has not been used for any experiments, since a large S-type crystal was already available. Moreover, the shape of the superconducting transition was not as sharp for 83105_02 as for the older crystal.

3.3   Magnon dispersion in A-type CeCu$_2$(Si$_{0.98}$Ge$_{0.02}$)$_2$

For S-type CeCu$_2$Si$_2$, the magnetic excitations have been studied in some detail both in the superconducting and the normal state [SAF+11, ASS+11]. They appear at the same position in Q-space where antiferromagnetic order is observed in the A-type samples. The excitations were found to be dispersive with a mode velocity of 4.4 meV Å in the superconducting state and around 7 meV Å in the normal state, for either $B > B_{c2}$ or $T > T_c$. These magnetic excitations are supposed to be the driving force of superconductivity [MPL07, Sca12]. So far, the relation of the paramagnons to the magnons of the ordered state is not known. Thus, the aim of the experiment presented in this section was to measure the magnetic excitations in an A-type crystal for comparison.

Neutron scattering experiments were performed with a crystal of composition CeCu$_2$(Si$_{0.98}$Ge$_{0.02}$)$_2$. So far, no other A-type crystal of identical stoichiometry has been studied by neutron scattering. Since a comparison with S-type CeCu$_2$Si$_2$ is intended, it needs to be verified that the Ge-substituted A-type crystal shows no principal differences to A-type CeCu$_2$Si$_2$. Therefore, the first step of the data analysis will be the comparison to neutron diffraction and neutron spectra of A-type samples without Ge substitution.

As a next step, the spin-wave dispersion of the A-type sample is analysed in detail and differences or similarities with the S-type sample are discussed. While the dispersion in the latter has only been measured along the [110] direction, this study also includes the dispersion along [001], to see if the magnetic interactions in CeCu$_2$Si$_2$ are isotropic.

Details of the experiments

Neutron scattering was performed at the cold triple axis spectrometer IN12 at ILL, Grenoble, with a doubly focussing monochromator and a doubly focussing analyser. For all measurements, the final neutron wave vector was fixed to $k_f = 1.15$ Å^{-1} ($\lambda_f = 5.45$ Å, $E_f = 2.74$ meV), which resulted in an energy resolution of 65 μeV (full width at half maximum, FWHM) at $E = 0$. Higher order contamination of the incident beam was prevented by a velocity selector in front of the monochromator. A neutron monitor in front of the sample was used for normalisation. The sample was a 3.0 g single crystal of composition CeCu$_2$(Si$_{0.98}$Ge$_{0.02}$)$_2$ (sample number 83102_01) with lattice constants $a = 4.10$ Å and $c = 10.00$ Å. The sample was glued onto a surface perpendicular to the [110] direction on a copper sample holder. Cooling to a base temperature of 100 mK was achieved by a dilution cryostat.

The heat capacity was first measured in a commercial Quantum Design PPMS (Physical Property Measurement System) on a small fraction (5 mg) of the crystal to examine the ground state. To have a proper reference for the neutron scattering data, the heat capacity of the entire crystal was also measured. This was done in a SHE dilution cryostat using the compensated heat pulse technique [WLRS04]. Due to the large sample mass it was necessary to provide an additional heat link from the sample to the thermal bath via a gold wire. Still, the sample temperature never fell below 230 mK within reasonable cooling times, even though the mixing chamber reached a base temperature of 50 mK. Furthermore, the AC susceptibility of the whole crystal was measured in a dilution cryostat down to 50 mK.

Results

The single crystal 83102_01 shows antiferromagnetic order below $T_N \approx 0.85$ K, which is evidenced by the appearance of a Bragg peak at $\tau = (0.215\ 0.215\ 0.52)$. It can be measured more easily in the second Brillouin zone, at $Q_{AF} = (0.215\ 0.215\ 1.48)$, due to a much larger signal-to-background ratio; two representative scans are shown in figure 3.3(a). The position of the peak, particularly along [110], is temperature-dependent above 0.4 K, reaching $h \approx 0.228$ around the Néel temperature (figure 3.3(c)). T_N could be confirmed by bulk heat capacity measurements (figure 3.3(b)); the transition is only mildly affected by a moderate field of 2 T ($B \parallel$ [110]), as expected for an antiferromagnet well below its critical field. The lock-in transition of the ordering vector at 0.4 K could not be resolved within the accuracy of the heat capacity data. All observations are in close agreement with the measurements on A-type CeCu$_2$Si$_2$ [SFZ$^+$04, SFS$^+$06].
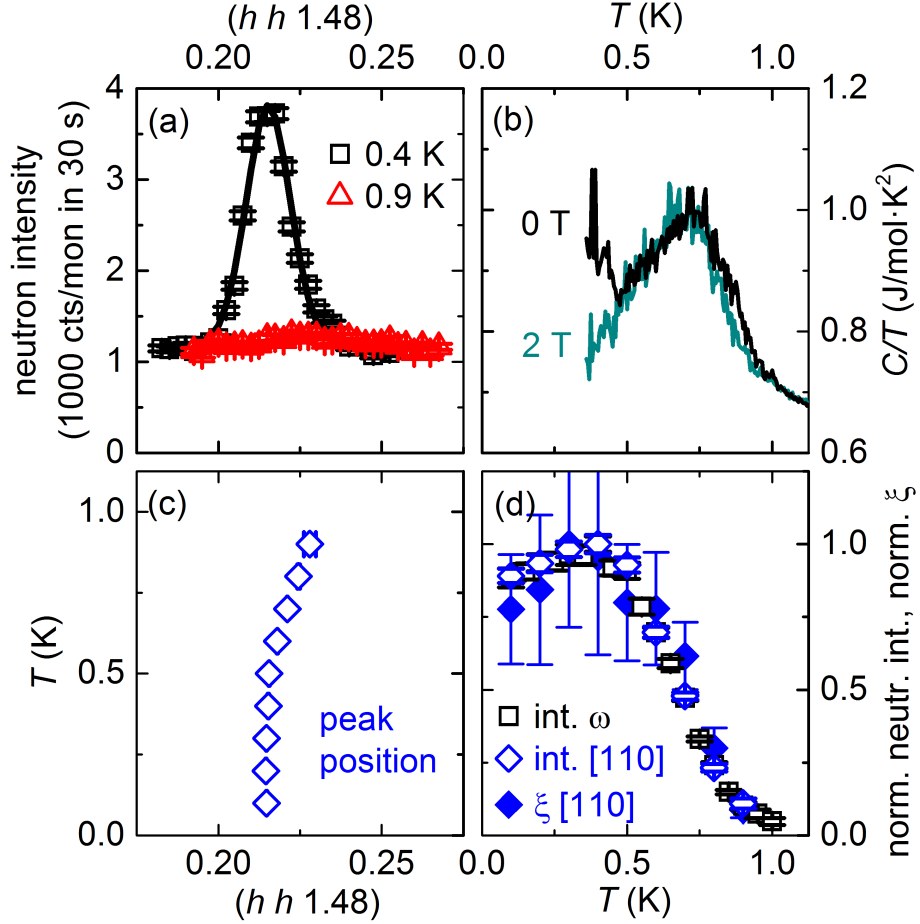
Figure 3.3: Magnetic order in A-type $CeCu_2(Si_{0.98}Ge_{0.02})_2$ (crystal 83102_01). (a) Scans across the magnetic Bragg peak at $Q_{AF} = (0.215\ 0.215\ 1.48)$, at 0.4 K and 0.9 K; the solid line is a Lorentzian fit. (b) Bulk heat capacity measured in zero field and in 2 T ($B \parallel [110]$), plotted as C/T vs. T. (c) Fitted value of the h component of Q_{AF} for different temperatures. (d) Normalised integrated intensity of the magnetic Bragg peak for scans along ω (sample rotation) or along [110], as well as normalised correlation length, vs. temperature.

Temperature-dependent measurements of the magnetic Bragg peak have been performed both as a function of sample rotation ω and in scans along [110]. Figure 3.3(d) shows the fitted intensity, extracted from Lorentzian fits to both types of scans. Also included is the normalised correlation length, which has been extracted from the Lorentzian width of the scans along [110]. The fits involve a convolution with the instrument resolution, which is slightly smaller than the total peak width. Both intensity and correlation length pass through a weak maximum at around 0.4 K. It has been reported earlier that the lock-in transition is coincident with the appearance of a superconducting minority phase, which limits the domain size [SFS$^+$06], and also the lifetime [ASF$^+$10], of the magnetic order. In a measurement of the AC susceptibility it was confirmed that the crystal is not bulk superconducting at low temperatures. Instead, a slight gradual decrease of the susceptibility is observed below 0.4 K. A broadened transition is also seen in the zero-field heat capacity data (figure 3.3(b)). In earlier neutron measurements only a broadening of the Bragg peak, but not a reduction of its intensity was observed [SFS$^+$06]. This suggests that a larger fraction of this crystal becomes superconducting than in the measurement of A-type CeCu$_2$Si$_2$.

The inelastic response can also be compared to prior measurements. Spectra taken at Q_{AF} show that the response is quasi-elastic for temperatures between 0.1 K and 5 K. It can be fitted with Lorentzian functions centred at zero and multiplied with the Bose-factor:

$$S(E) = \frac{1}{1 - \exp(-\frac{E}{k_{\mathrm{B}}T})} \cdot \frac{2E\chi}{\pi\Gamma \left(1 + \frac{2E}{\Gamma}\right)^2}. \tag{3.1}$$

Here Γ is the full width of the fluctuations, and χ their susceptibility. This function is then convoluted with a Gaussian function for the instrument resolution. All spectra also feature a temperature-independent, incoherent elastic line, and the spectra below T_{N} include a magnetic Bragg peak. Two spectra, measured at 0.4 K and 5 K, are shown in figure 3.4(a), together with the total fit function and the magnetic contribution to the fit.

The fitted inverse susceptibility $1/\chi$ and width Γ (FWHM, inverse lifetime) of the A-type crystal are displayed in figures 3.4(b) and 3.4(c), respectively. The figure also includes the fit results for the S-type sample from reference [ASS$^+$11], which will be discussed later. $1/\chi$ and Γ of the A-type crystal decrease with decreasing temperature; a divergence of susceptibility and lifetime $\tau \propto 1/\Gamma$ is expected on entering the ordered phase, but the fits suggest small residual values for $1/\chi$ and Γ. The exact magnitude of susceptibility and width is difficult to extract from a fit according to equation 3.1, because the separation of the inelastic magnetic signal and the magnetic
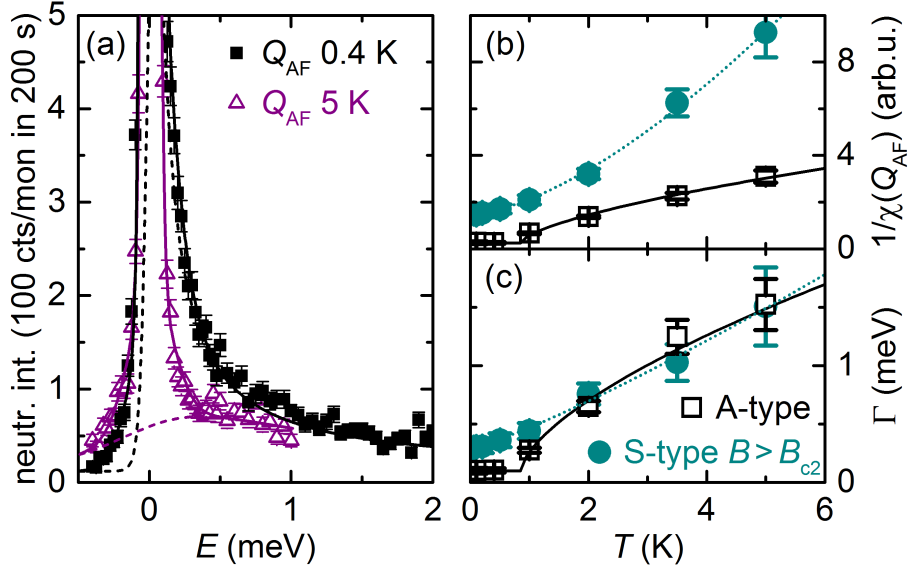
Figure 3.4: (a) Spectra of the A-type crystal at 0.4 K (black) and 5 K (purple), measured at Q_{AF} = (0.215 0.215 1.48); solid black/purple lines show total fit functions, dashed the inelastic magnetic contribution, which was fitted with a Bose-weighted Lorentzian function. (b) Fitted inverse susceptibility $1/\chi$ and (c) width Γ (FWHM) of the inelastic magnetic signal at Q_{AF}, for the A-type crystal and for the S-type crystal at 1.7 T (taken from reference [ASS$^+$11]). $\chi(Q_{AF})$ is normalised to the intensity of the incoherent elastic line. Lines are guides to the eye.

Bragg peak becomes problematic when Γ is small, i.e. close to the instrument resolution. In earlier measurements on A-type CeCu$_2$Si$_2$, a triple-axis experiment suggested a truly elastic signal well below T_N [SFS$^+$06], while spin-echo data, which have a better energy resolution, indicated that the lifetime of the magnetic order in A-type CeCu$_2$Si$_2$ is limited in the presence of filamentary superconductivity [ASF$^+$10]. In the A-type crystal studied here, the lifetime-broadening seems to be more significant, so that it can already be detected with the resolution of a triple-axis spectrometer. It is worth noting that the effect can be observed not only at 0.1 K, but also at 0.4 K, where filamentary superconductivity only just sets in.

It can be concluded that the Ge-substituted crystal investigated here shows magnetic order very similar to A-type CeCu$_2$Si$_2$, with the restriction that the influence of domains and minority phases is stronger. The probable reason is a larger sample inhomogeneity. However, the order is still

long-ranged and long-lived on the length- and time-scales of the studied excitations, which are strongly damped (see below). This is also supported by the comparison of dispersion measurements at 0.1 K and 0.4 K, which are nearly identical. Nevertheless, the discussion of the magnons in the following will be based on the data at 0.4 K, to minimise any possible influence of the minority phases. Such, the new CeCu$_2$(Si$_{0.98}$Ge$_{0.02}$)$_2$ crystal can serve as a reference to S-type CeCu$_2$Si$_2$ in the same way as an A-type crystal without Ge doping could.

Now the dispersion of the magnetic excitations will be discussed, i.e. the magnons ($T < T_N$) or paramagnons ($T > T_N$). For this purpose, scans were taken along (h h 1.48) or along (0.215 0.215 l) at fixed energy transfers between 0.125 meV and 1.1 meV. Measurement temperatures were $T = 0.4$ K, where the antiferromagnetic ordering is strongest, and $T = 1$ K, just above the Néel temperature.

The measured dispersion along [110] is shown in figure 3.5 and the measured dispersion along [001] is shown in figure 3.6. Only the data at 0.4 K are displayed, since the scans at 1 K look very similar. Scans at 0.9 meV and 1.1 meV were not performed along [001] because the peaks are very broad already at 0.7 meV. Also shown in each figure are fits with two Lorentzian curves (red lines) of identical width. They were convoluted with a Gaussian function for the resolution, which was taken to be the elastic width at Q_{AF}. At 0.125 meV, the signal was fitted with the restriction that the two branches of the dispersion should have the same intensity, which avoids unphysical solutions for the dispersion at this low energy transfer. The asymmetric line shape at 0.125 meV is most likely due to the mosaicity of the sample. At all other energy transfers, Lorentzian fits without fitting restrictions provide a very good description of the data. An alternative fitting procedure, which yields the blue lines in figures 3.5 and 3.6, will be discussed below. Figure 3.5 also includes a constant-Q scan at the magnetic zone boundary, $Q = $ (0.5 0.5 1.48).

Within the (h h l) plane, a conical dispersion is expected at low energy transfers. A cut along a certain direction, which corresponds to the experimental set-up, then yields two lines, which will be referred to as branches in the following. The cone does not need to be symmetric with respect to the high-symmetry directions [110] and [001], but could be tilted or distorted, leading to different mode velocities along different directions.

The two branches of the dispersion along [110] are asymmetric in intensity, which is particularly visible at 0.5 meV and 0.7 meV. This has already been observed for S-type CeCu$_2$Si$_2$ [SAF+11, ASS+11]. Such an intensity difference may be caused by a different intersection angle of the two dispersion branches with the resolution ellipsoid of the spectrometer. Indeed,
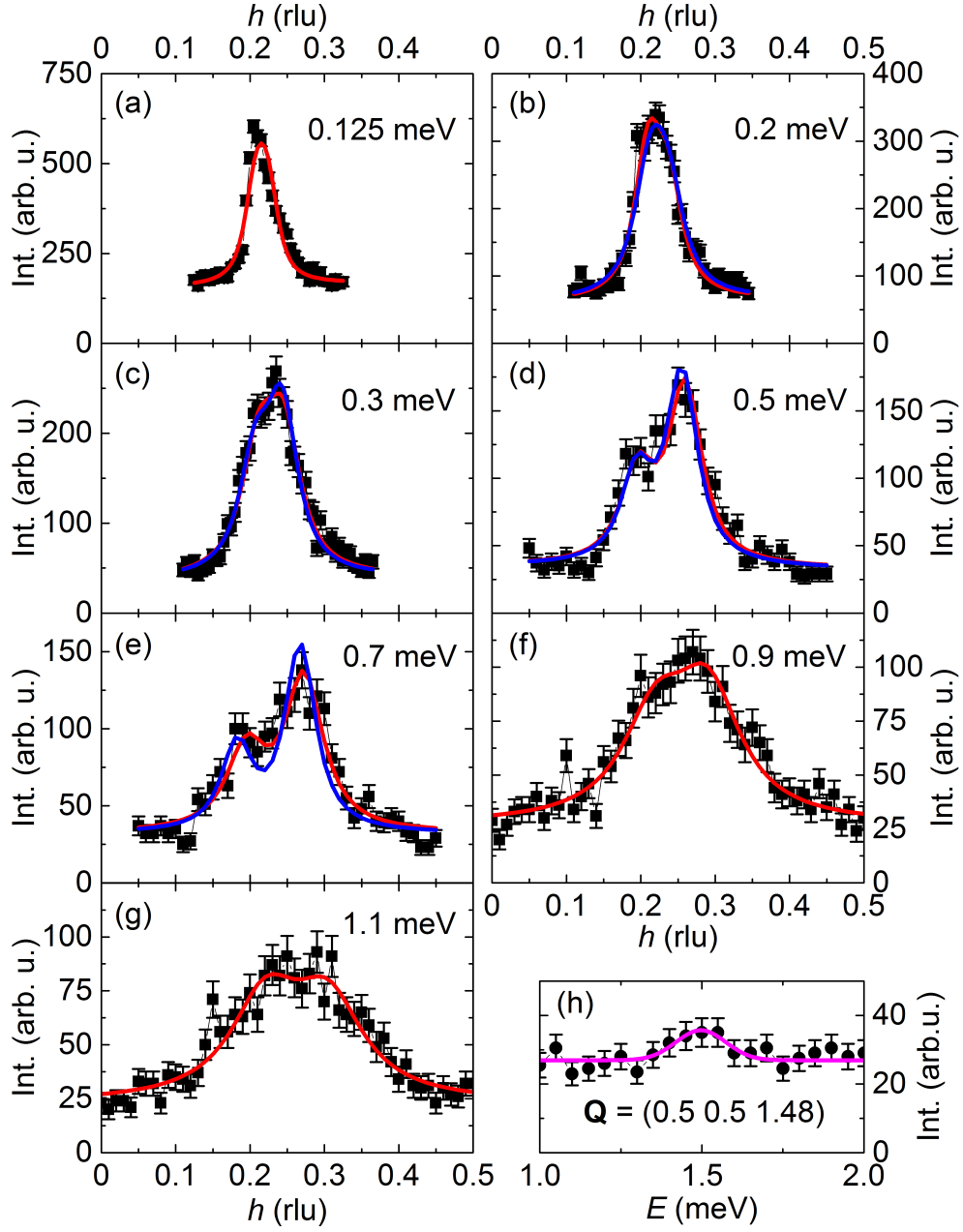
Figure 3.5: Dispersion of A-type CeCu$_2$(Si$_{0.98}$Ge$_{0.02}$)$_2$ along [110] at 0.4 K. Images (a)-(g) display constant-E scans at different energy transfers. Measured data points are shown in black, Lorentzian fit curves in red and fits according to equation S11 of [SAF$^+$11] in blue. The fits consider an appropriate background for each energy transfer. (h) shows a constant-Q scan at the magnetic zone boundary; the pink line is a Gaussian fit.
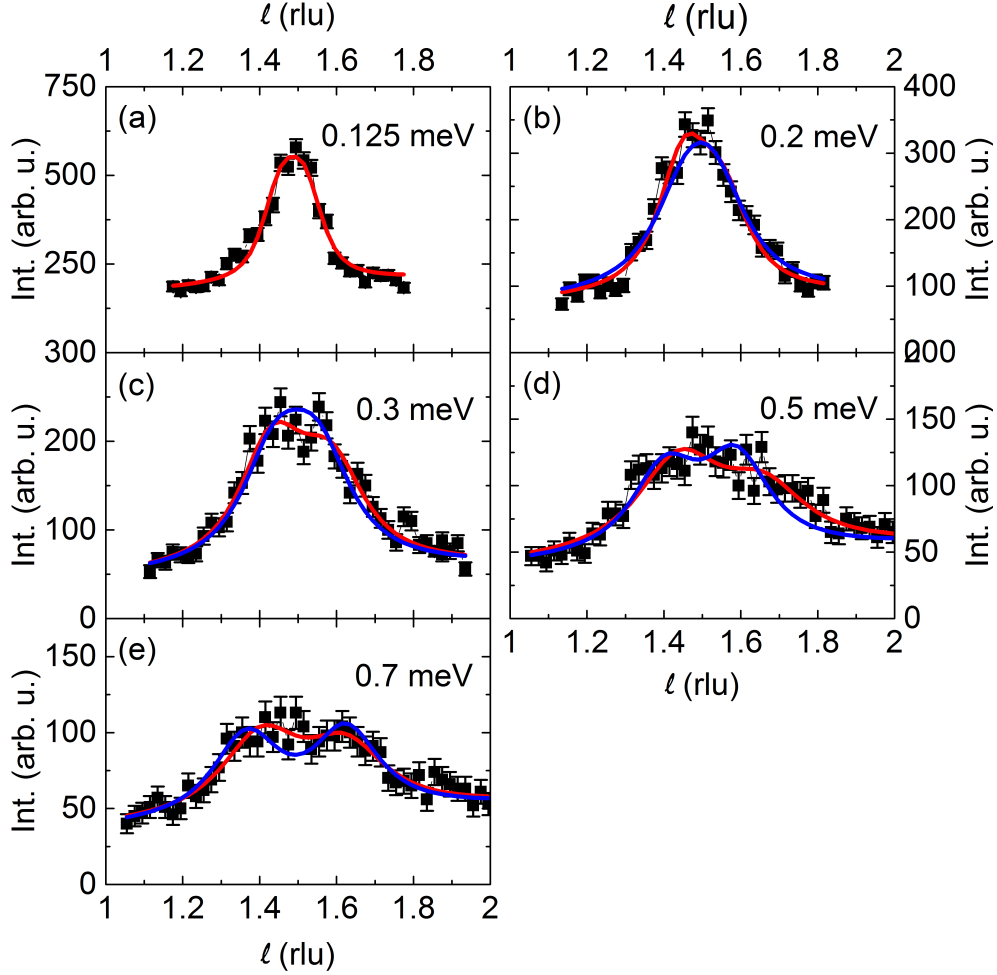
Figure 3.6: Dispersion of A-type $CeCu_2(Si_{0.98}Ge_{0.02})_2$ along [001] at 0.4 K. Images (a)-(e) display constant-E scans at different energy transfers. Measured data points are shown in black, Lorentzian fit curves in red and fits according to equation S11 of [SAF$^+$11] in blue. The fits consider an appropriate background for each energy transfer.
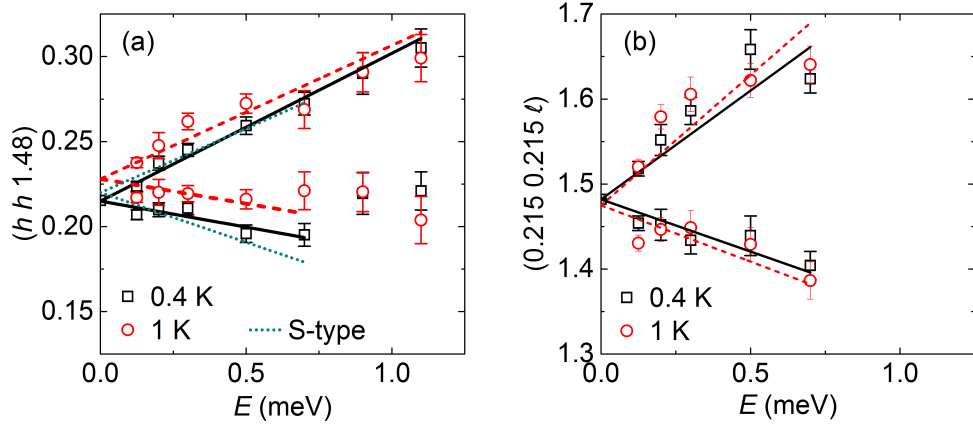
Figure 3.7: Inelastic peak positions as extracted from Lorentzian fits to the constant-E scans shown in figures 3.5 and 3.6, measured along [110] (a) and [001] (b). Additionally the fit results for scans at 1 K are shown, as well as the position of the Bragg peak at 0.4 K. The solid/dashed lines show linear fits for both dispersion branches at 0.4 K and 1 K, respectively. For comparison, the dispersion of the S-type crystal is added in dotted green lines ($T = 60$ mK, $B > B_{c2}$, new fits to data from reference [ASS$^+$11]).

simulations of the resolution using the programme Restrax [res, Sar96] show that the resolution of the lower branch is around a factor of 2 larger than that of the upper branch. However, the inelastic peaks are generally much broader than the resolution due to damping, so that resolution effects, even of a factor of 2, should not have a major impact on the data. Furthermore, it is not observed that the weaker branch is broader. Therefore, the asymmetry in the intensity along [110] does not seem to be merely an effect of the instrumentation. Along [001], the intensity is symmetric for the two dispersion branches.

The fitted peak positions for all Q-scans are shown in figure 3.7. Looking first at the upper branch, the dispersion is linear up to the highest measured energy transfer, with a spin-wave velocity of 5.3±0.3 meV Å along [110] and 6.2±0.8 meV Å along [001] at 0.4 K. Thus, within error bars the spin-wave velocity is the same along [110] and [001]. The dispersion of the lower branch is more difficult to determine due to the suppression of intensity in the scans along [110]; at 0.9 meV and 1.1 meV, the peak positions of the weaker branch cannot be fitted reliably, so that they were not included in the dispersion fit. The fits up to 0.7 meV indicate that the spin-wave velocity is increased by a factor of 2 in the [001] direction and roughly a factor of 3 in the [110] direction.

A possible explanation for the asymmetry of the two branches could be that the order is incommensurate and therefore the distance to the magnetic zone boundary is different when h or l are increased or decreased. However, the effect seems rather large considering that 0.215 and particularly 1.48 are not very far from the zone centres 0.25 and 1.5, respectively. Therefore, it has to be concluded that the origin of the asymmetry is not understood at present. It is somewhat reminiscent of the spin-wave dispersion of chromium [Faw88], but whether the underlying physics is the same is not clear. It is also interesting to note that CeCu$_2$Ge$_2$, which is isostructural and isoelectronic to CeCu$_2$Si$_2$ and has a similar ordering wave vector, does not show the strong asymmetry of the two dispersion branches [Sto].

The data give no indication of an anisotropy gap in the ordered state of A-type CeCu$_2$Si$_2$, as it was observed in the dispersion of the heavy-fermion compounds CePd$_2$Si$_2$ [vDFC+97], CeIn$_3$ [KRF+03], CeRhIn$_5$ [DLG+14] and CeCu$_2$Ge$_2$ [GFR+]. This probably relates to the very close proximity of A-type CeCu$_2$Si$_2$ to the quantum critical point, which is also reflected in the small ordered moment of 0.1 μ_{B}/Ce [SFZ+04]: It is expected that excitations become soft close to the quantum critical point. It is still possible that an anisotropy gap exists which is smaller than the resolution of the experiment (65 μeV).

Figure 3.8 shows the fitted susceptibility and Q-width (FWHM) of the constant-E-scans for both the [110] and the [001] direction. Here the reciprocal lattice units (rlu) have been transformed into momentum transfer (Å^{-1}) for an easier comparison. The susceptibility is obtained by dividing the integrated intensity of the Lorentzian fits by the Bose factor; it gradually falls off with energy transfer. The width at all energy transfers is much larger than the elastic Q-width: The inelastic correlation length at low energy transfers is around 25 Å at 0.4 K, an order of magnitude smaller than the elastic correlation length. This hints at strong damping of the spin fluctuations by the conduction electrons. The damping increases towards higher energy transfers, where the inelastic correlation length drops to values corresponding to about twice the nearest-neighbour distance. The origin of this effect might be enhanced Kondo scattering, since the energy scale $\approx$ 1 meV is similar to the local spin-fluctuation temperature of CeCu$_2$Si$_2$, which was observed in powder neutron spectroscopy [HHML+81]. Due to the strong broadening of the signal, it is difficult to follow the dispersion further towards the magnetic zone boundary. In the constant-Q scan at (0.5 0.5 1.48) (cf. figure 3.5), a weak maximum can be seen at 1.5 meV, which might be related to the bending of the dispersion. However, the peak seems rather sharp considering the damping observed in the constant-E scans, so that its interpretation remains doubtful.
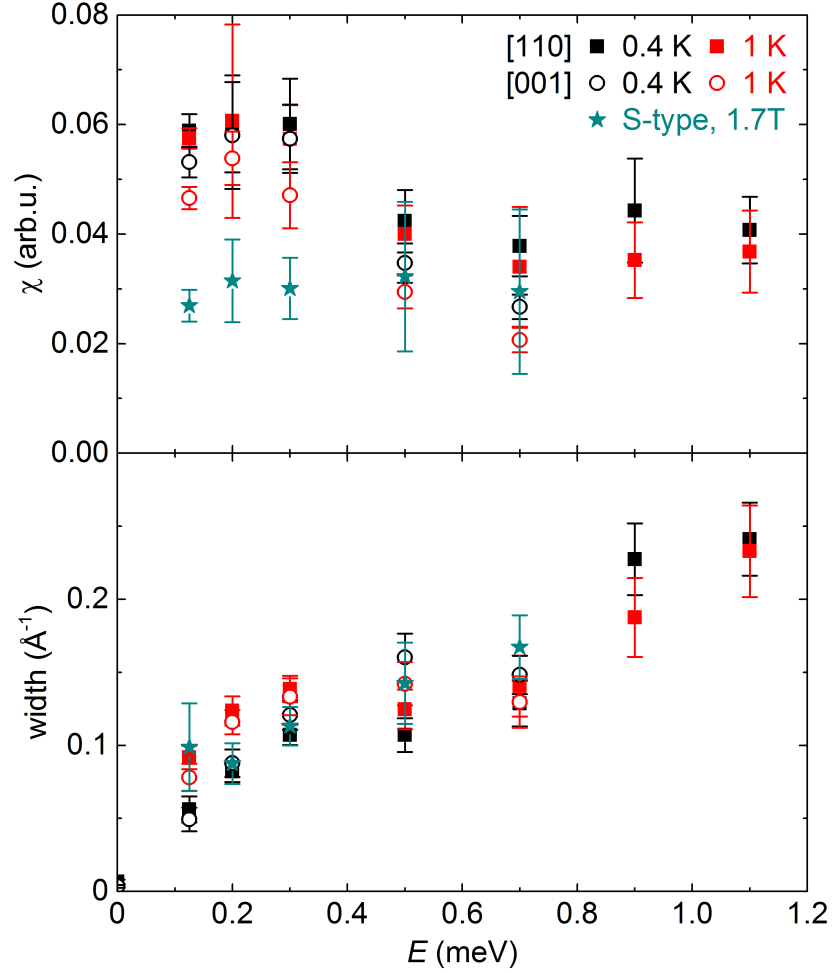
Figure 3.8: Susceptibility χ and width (FWHM) of Lorentzian fits to the dispersion of A-type CeCu$_2$(Si$_{0.98}$Ge$_{0.02}$)$_2$ along [110] and [001]. The susceptibility is the sum of the integrated intensity of both branches of the dispersion, divided by the Bose factor. To be able to compare the results from scans along [110] and [001], the x-axis was transformed from reciprocal lattice units (comp. figures 3.5, 3.6 and 3.7) to Å^{-1}. Fit results for the S-type crystal ($T = 60$ mK, $B > B_{c2}$) are also shown (new fits to data from reference [ASS$^+$11]).

The comparison of susceptibility and Q-width for the [110] and the [001] direction reveals that they are identical within the error bars. The apparent difference in the width of the original data, see figures 3.5 and 3.6, stems from the different conversion factor from rlu to Å^{-1} (2.17 Å^{-1}/rlu along [110] and 0.63 Å^{-1}/rlu along [001]), in combination with a slightly poorer resolution along [001]. The striking similarities of the excitations measured along [110] and [001], in terms of mode velocity, intensity and Q-width, speak for truly 3-dimensional interactions in CeCu$_2$Si$_2$. Similar behaviour has been reported for the cubic compound CeIn$_3$ [KRF$^+$03], but is not generally expected for a compound with tetragonal crystal structure such as CeCu$_2$Si$_2$.

In figures 3.7 and 3.8, also the fit results for $T = 1$ K are included. The dispersion is nearly unchanged, the only difference being a shift of Q_{AF}, the centre of the dispersion; the spin-wave velocity is unchanged within error bars for both the [110] and the [001] direction. Figure 3.8 shows that also the Q-width and the susceptibility are similar at 0.4 K and 1 K. The excitations in the ordered phase are slightly more intense and sharp, but that does not reflect the (near) divergence of susceptibility and correlation length which is observed in the elastic channel. Thus, the response of the antiferromagnetic and the paramagnetic state seem to differ only at very low energy transfers $\Delta E \lesssim 0.15$ meV.

So far, the magnetic response has been fitted independently for each energy transfer. It would be useful to have a fit function that describes the whole dispersion. In the appendix of reference [SAF$^+$11], it was suggested that the inelastic response in the presence of (para-)magnons takes the form

$$\chi'' = \frac{\chi_0 \; E/\Gamma}{4 \cdot \xi^4 (Q - Q_{exc})^2 (Q_{exc} - Q_{AF})^2 + E^2/\Gamma^2} \tag{3.2}$$

for a fixed energy transfer E and in the vicinity of Q_{AF}. Here Γ is the energy width which can be extracted from the spectra[2], ξ is the correlation length and Q_{exc} is the position of the peak at energy transfer E. Based on equation 3.2, a common fit function for all energy transfers can be constructed, with two peaks at $Q_{AF} + \Delta Q$ and $Q_{AF} - \Delta Q$ for each constant-E scan. χ_0, Γ and ξ are common variables for all energy transfers, and a linear dispersion relation is implied, with the same spin-wave velocity for both branches. Different intensities of the two branches are allowed by the fit function, and it includes the Bose factor and the instrument resolution.

Figure 3.8 already shows that the assumption that χ_0 and ξ are independent of the energy transfer is not verified in experiment. To get reasonable fit

---

[2]The slightly modified form of equation 3.2 compared to S11 in reference [SAF$^+$11] originates from different definitions of Γ; Γ in equation S11 should be replaced by $\Gamma \cdot \xi^2$ to get to equation 3.2.

results, the function was modified such that it allows for a different value of χ_0 for each energy transfer. On the other hand, ξ can be assumed to be constant if the data at 0.9 meV and 1.1 meV are omitted, which are significantly broader. The data at 0.125 meV were also omitted, due to their irregular peak shape. Thus, the data at 0.2 meV, 0.3 meV, 0.5 meV and 0.7 meV were fitted with the same correlation length, dispersion relation and energy width Γ, the latter taken from the fits to the spectra. The resulting fit curves are shown in blue in figures 3.5 and 3.6. Their agreement with the data is satisfactory.

These fits result in spin wave velocities of 7.6±0.3 meV Å along the [110] direction and 8.6±0.4 meV Å along the [001] direction at 0.4 K. At 1 K, they change to 9.0±0.6 meV Å and 8.7±0.5 meV Å, respectively. All values are in between the fit results for the upper and the lower branch from the Lorentzian fits, but much closer to the values for the upper branch. As in the Lorentzian fits, the dispersion is the same along [110] and [001] and nearly unaffected by the transition from the antiferromagnetic to the paramagnetic state. The correlation lengths extracted from these fits are 23 Å at 0.4 K and 13 Å at 1 K (for both directions), similar to the results from Lorentzians fits.

In summary, the model underlying equation 3.2 does not fully describe the physics of A-type CeCu$_2$Si$_2$. It clearly fails to describe the data at 0.9 meV and 1.1 meV, where an additional damping mechanism is probably active. At lower energy transfers, a reasonable description of the data is possible, however only when χ_0 is made energy-dependent, which is actually a strong modification of the original model. Equation 3.2 also does not capture the asymmetry of the two dispersion branches, so that fitted mode velocities are a compromise between the upper and the lower branch.

The inelastic response of the A-type crystal can now be compared to that of S-type CeCu$_2$Si$_2$ [ASS+11, SAF+11]. For this purpose, data of the S-type crystal in the normal state ($B > B_{c2}$) are included in figures 3.4, 3.7 and 3.8. The fits of the spectra in figure 3.4 were taken directly from reference [ASS+11], while the fits to the dispersion, shown in figures 3.7 and 3.8, originated from new, Lorentzian fits to the data presented in reference [ASS+11]. This was done to ensure comparability by an analogous fitting procedure (Arndt *et al.* have fitted Gaussian peaks, and assumed the same mode velocity for both branches). To be able to compare the susceptibilities of both crystals, all intensities have been normalised to the incoherent elastic line; it mainly originates from the copper nuclei in CeCu$_2$Si$_2$ and thus provides a reference which is independent from the ground state of the sample. Explicit comparisons will only be made to the normal state data of S-type CeCu$_2$Si$_2$. However, intensity, width and peak positions of the constant-E scans are

similar for the superconducting and the normal state, as long as data are not too close to the spin gap of 0.2 meV [ASS$^+$11, SAF$^+$11]. Thus, much of the following discussion would also apply to the superconducting state.

A pronounced difference is observed for the susceptibility of the A- and the S-type sample: Even above T_N, it is about a factor of 2.5 larger in the A-type CeCu$_2$Si$_2$, which can be seen by comparing the spectra (figure 3.4) and the constant-E scans at small energy transfers (figure 3.8). The origin of this difference lies in the enhancement of the Kondo effect in S-type CeCu$_2$Si$_2$ compared to A-type CeCu$_2$Si$_2$.

However, the dispersion relation of S-type CeCu$_2$Si$_2$ in the normal state behaves very similarly to that of A-type CeCu$_2$Si$_2$: Figure 3.7 shows that the fitted dispersion relations nearly fall on top of each other. The fits shown for the S-type crystal correspond to mode velocities of 6.1 ± 0.5 meV Å and 7.9 ± 0.6 meV Å for the upper and the lower branch of the dispersion. Arndt *et al.* reported 7.1 ± 1.9 meV Å assuming identical mode velocities [ASS$^+$11]. Using a new data set, measured on the same crystal under similar conditions, 7.0 ± 0.9 meV Å was obtained for the upper branch and 10.8 ± 2.9 meV Å for the lower branch (see section 3.4). All these numbers suggest that the asymmetry between the two branches is somewhat weaker for the S-type crystal, but otherwise the dispersion relation in the measured energy range is nearly identical to the A-type sample.

The damping for A-type and S-type samples is also very similar, which is evident from the Q-width (figure 3.8). As long as both samples are in the paramagnetic state, the lifetime $1/\Gamma$ is also very similar (figure 3.4). This can be explained by the fact that both samples are metallic and feature strong local Kondo interactions of the conduction electrons with the 4f moments.

It is interesting to compare these results to recent measurements of the magnetic excitations in cuprate and pnictide superconductors by Resonant Inelastic X-ray Scattering (RIXS): Le Tacon *et al.* [LTGC$^+$11] compared undoped antiferromagnetic Nd$_{1.2}$Ba$_{1.8}$Cu$_3$O$_6$ to several doped members of the same family and found that the paramagnons observed in the latter show a very similar dispersion relation to the magnons. Furthermore, the spectral weight of the spin excitations is not strongly affected by doping. The excitations are, however, much broader in the doped samples, due to the damping induced by the charge carriers. For the pnictides, Zhou *et al.* [ZHM$^+$13] compared undoped BaFe$_2$As$_2$ with optimally hole-doped Ba$_{0.6}$K$_{0.4}$Fe$_2$As$_2$. They also found that the magnetic excitations persist in the superconducting phase with almost identical intensity. Here, the dispersion relation is more strongly influenced by doping than in the cuprate study: Significant softening is observed for the doped sample. On the other hand, damping is not affected by doping, as the parent compound is already metallic.

Thus, there is evidence for these three classes of unconventional super-conductors that the inelastic magnetic response is similar for the antiferro-magnetic and the superconducting state. This is remarkable, considering the drastic changes in the elastic magnetic response and the ground-state properties. It is particularly interesting that these compound classes behave somewhat similar even though the mechanisms for the suppression of magnetic order are different. In the heavy fermions, the mechanism is the enhancement of the Kondo effect, evident from the data by the loss in inelastic magnetic intensity in the S-type sample. In the cuprates, the order is suppressed by doping, which strongly increases the damping rates in the inelastic response, as seen by their larger width [LTGC$^+$11]. The origin of the softening observed for the pnictide superconductor is not explained by the authors in reference [ZHM$^+$13]. Further measurements on other pnictide compounds might clarify the matter.

LeTacon *et al.* [LTGC$^+$11] also discuss important differences in the magnetic response between antiferromagnetic and superconducting cuprate samples, using earlier data from inelastic neutron scattering [HBP$^+$07]. Strong deviations appear at energy transfers $\lesssim 75$ meV, which is around one quarter of the full energy span of the dispersion. This is roughly comparable to the energy scales in CeCu$_2$Si$_2$, where the response is modified close to the gap size of 0.2 meV, while the full energy span is estimated to be around 1.5 meV. For the pnictides, the low-energy difference between the antiferromagentic and the superconducting state has not been shown [ZHM$^+$13], but must be smaller than ≈ 80 meV, for a full energy span of 200 meV. Interestingly, the authors report that the inelastic response in the measured range is not sensitive to raising the temperature above T_c, similar to the observations for S-type CeCu$_2$Si$_2$ for energies larger than the gap size [SAF$^+$11].

The data presented here, particularly in analogy with cuprates and pnictides, show that the magnetic excitations are stable through large areas of the phase diagram around the quantum critical point. Above a certain low-energy scale, they are neither sensitive to the ground state of the compound, nor to crossing the critical temperatures T_N and T_c. This supports the idea that magnetic fluctuations, well outside the antiferromagnetic phase, can be the driving force of superconductivity.

3.4   Critical magnetic scattering in S-type CeCu$_2$Si$_2$

The dispersion of S-type CeCu$_2$Si$_2$ has already been discussed in some detail in the previous section based on data measured by Julia Arndt and Oliver Stockert [ASS$^+$11, SAF$^+$11]. In this section, the focus is on a different aspect of the inelastic response, the scaling behaviour on approaching the quantum

critical point. S-type CeCu$_2$Si$_2$ is located close to the critical value r_c of the tuning parameter, and quantum critical behaviour as a function of temperature can be studied if superconductivity is suppressed.

The scaling of the lifetime of the magnetic fluctuations has been analysed in reference [ASS$^+$11]: A $T^{-3/2}$ power law was observed, which is in agreement with the predictions of the Hertz-Millis-Moriya scenario for a 3D-antiferromagnetic quantum critical point [Mil93]. The same theory predicts ν, the critical exponent of the correlation length, to take the value $3/4$, since the dynamical critical exponent z is expected to be 2 [Her76] (see equation 2.16). The aim of the experiment presented in the following was therefore to measure the Q-dependence of the fluctuations as a function of temperature to verify the values of ν and z.

Details of the experiments

The measurements on S-type CeCu$_2$Si$_2$ were performed on the cold neutron spectrometer IN14 at ILL, Grenoble. Since they were a continuation of prior measurements by Julia Arndt and Oliver Stockert, the experimental set-up was very similar: A vertically focussing monochromator followed by 60' collimation, a Be filter to prevent higher order contamination, a monitor for normalisation in front of the sample, and a doubly focussing analyser. The final neutron wave vector k_{f} was fixed during the measurement to 1.15 Å^{-1}. The same 2.03 g sample ($a = 4.09$ Å, $c = 9.88$ Å) and the same copper sample holder were used as in the previous experiment, and also the same vertical magnet ($B_{\mathrm{max}} = 2.5$ T). The sample was glued such that the field was parallel to the $[1\bar{1}0]$ direction. Cooling to a base temperature of 60 mK was achieved by a dilution cryostat.

Results

This section is concerned with the quantum critical scaling and not the superconducting properties of S-type CeCu$_2$Si$_2$. Therefore, all data discussed in the following were measured at 1.7 T in the normal phase. Thus, the quantum critical cone of the phase diagram is probed, as can be seen by a comparison of figures 2.1 and 3.1.

S-type CeCu$_2$Si$_2$ does not show any long-range magnetic order. However, at low temperatures fractions of the sample exhibit short-range magnetic correlations, which show up in neutron scattering as elastic reflections with substantial broadening in Q ($\xi \approx 60$ Å) [SAS$^+$08]. In combination with a poor signal-to-background ratio, this hinders measurements of the order parameter fluctuations in the elastic channel. Instead, the fluctuations can

be measured in Q-scans at a small finite energy transfer. Spectra at Q_{AF} show that the maximum of the fluctuations is between 0.1 and 0.3 meV in the relevant temperature range [ASS$^+$11], so that it would be sensible to study the Q-dependence of the fluctuations at ≈ 0.2 meV.

However, the matter is further complicated by the appearance of spin waves in the paramagnetic state [SAF$^+$11, ASS$^+$11]. They show a linear dispersion, so that the response at any non-zero energy transfer should be fitted with two peaks, as explained in section 3.3. Therefore, Q-scans were performed not only at 0.2 meV, but also at 0.3 meV, 0.5 meV, 0.7 meV and 0.9 meV to obtain a thorough understanding of the inelastic response of S-type $CeCu_2Si_2$.

Constant-E scans around $Q_{AF} \approx (0.22\ 0.22\ 1.46)$ were measured along [110] at fixed $l = 1.458$; they were fitted in two different ways, just as for the A-type crystal: Fits for each energy transfer were done with two Lorentzian curves, under the constraint that they have the same Q-width. A common fit for all energy transfers measured at one temperature was done with equation 3.2. Both fitting procedures include a convolution with a Gaussian for the Q-resolution of the spectrometer, which was assumed to be constant in the considered range of momentum and energy transfers.

In figure 3.9, the magnetic intensity in the Q-E-plane around the nesting wave vector Q_{AF} is shown for different temperatures. The figure displays not the original data, but the fit curves from the two-Lorentzian fit, which provide a very good description of the data. An interpolation has been performed for intermediate energy transfers. At $T = 60$ mK, the two branches of the dispersion are clearly visible, the lower one being much weaker and less dispersive than the upper. This is very similar to the data of the A-type crystal (see section 3.3). At higher temperatures, only the upper branch of the dispersion can be unambiguously identified.

Fitting the dispersion is more difficult for the S-type crystal than for the A-type crystal, not only due to the smaller signal-to-background ratio, but also because the centre of the dispersion is not known a priori. At 60 mK, the dispersion is fitted to be 7.0±0.9 meV Å for the upper branch and 10.8±2.9 meV Å for the lower branch, if the centre of the dispersion is set to 0.228 rlu. This value of the centre is a compromise for the two branches, since fitting each branch independently does not yield the same centre. The fitted dispersion is similar to the one of the A-type crystal (see section 3.3) and in good agreement with prior results of Arndt *et al.* for the S-type crystal, who found 7.1±1.9 meV Å assuming symmetric spin wave velocities for both branches [ASS$^+$11].

At higher temperatures, fitting the dispersion becomes increasingly difficult. However, the splitting of the peaks at 0.5 meV and 0.7 meV can be
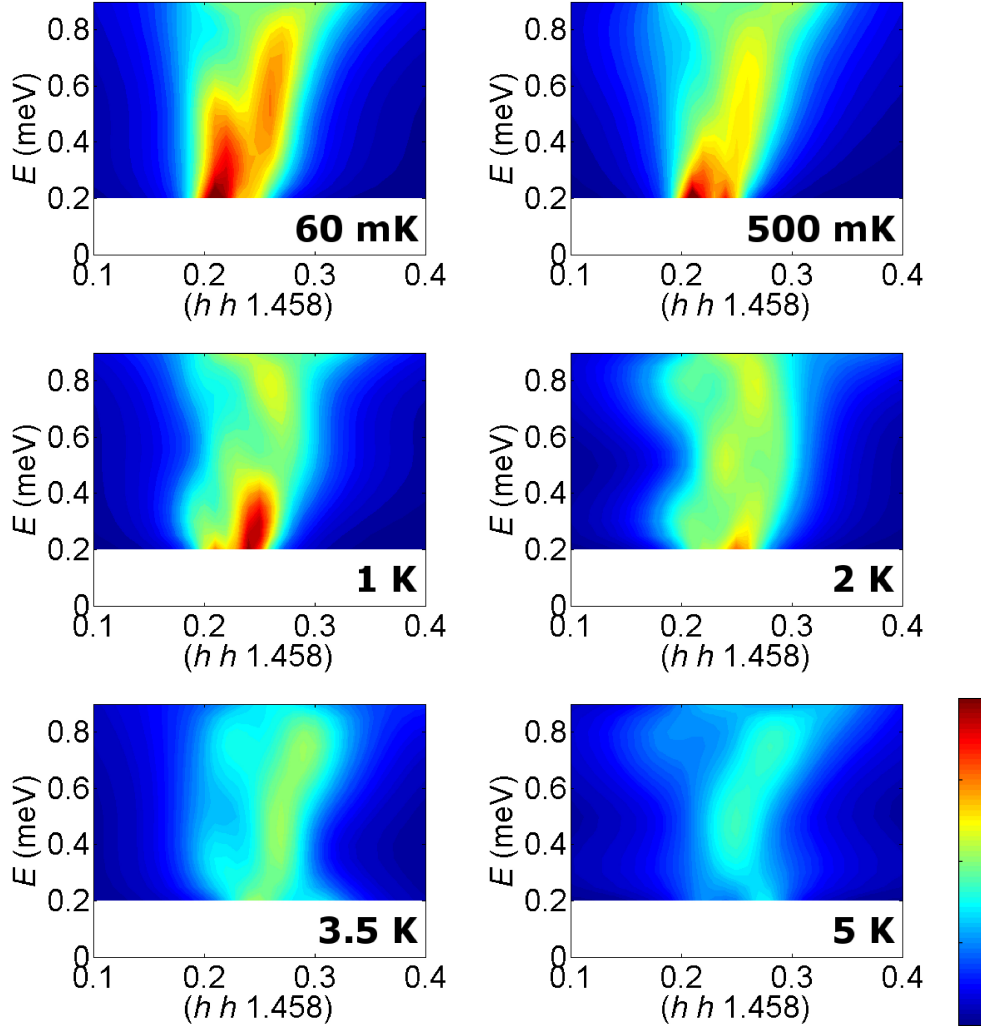
Figure 3.9: Inelastic magnetic intensity of S-type CeCu$_2$Si$_2$ at (h h 1.458) at different temperatures, B = 1.7 T. The intensity of the fit curves at 0.2 meV, 0.3 meV, 0.5 meV, 0.7 meV and 0.9 meV has been interpolated to intermediate values. The same colour scale is used for all plots (bottom right, intensity units arbitrary).

fitted up to 2 K and stays roughly constant throughout the whole temperature range, suggesting that the mode velocity is not strongly temperature dependent. At 0.2 meV, 0.3 meV and 0.9 meV the splitting cannot be resolved since it is too small compared to the width of the peaks. Data at 0.9 meV are significantly broadened at all temperatures, which has also been observed in the A-type crystal and is probably related to enhanced Kondo scattering. At 3.5 K and 5 K, the splitting cannot be fitted reliably at any energy transfer, but the intensity distribution shown in figure 3.9 suggests that the mode stays dispersive.

The centre of the dispersive mode shifts considerably with temperature. At the highest measured temperatures, the centre is around $h = 0.26$. This means that the spectra taken at (0.22 0.22 1.46) in reference [ASS$^+$11] were not measured at the position of maximum intensity. However, since the signal is rather broad in Q, the decrease in intensity from the maximum to $h = 0.22$ amounts to only about 25%, which should not strongly affect the reliability of the analysis.

Following the analysis of the dispersion, the correlation length of the magnetic fluctuations $\xi = 2/\kappa$ can now be discussed, κ being the full Q-width of the fluctuations. As explained above, it will be defined as the average of the width at 0.2 meV and 0.3 meV, where the intensity as a function of energy is strongest. For this purpose, the fits presented in figure 3.9 have been slightly modified: The data at 0.2 meV and 0.3 meV were re-fitted with a fixed splitting which is determined from the splitting at 0.5 meV and 0.7 meV assuming a linear dispersion. This is done to minimise the error arising from the competition between Q-width and Q-splitting which is present in the two-Lorentzian fits. As said above, the dispersion cannot be fitted at 3.5 K and 5 K; however, the Q-width is much larger at these temperatures than the approximate dispersive splitting at 0.2 meV and 0.3 meV, so that the fitted value of κ is rather insensitive to the exact value of the splitting. The resulting values for the Q-width are plotted as a function of temperature in figure 3.10(a).

Another possibility for analysing the correlation length is using fit function 3.2, S11 from reference [SAF$^+$11]. As for the A-type crystal (section 3.3), the data at 0.9 meV need to be excluded since the peaks are too broad. Also, it is again apparent that fitting the data with a constant χ_0 for all energy transfers is not possible. Therefore, χ_0 is fitted independently for each scan. The fit functions, using common values for κ and the spin-wave velocity, provide a satisfactory description of the data. The fitted spin-wave velocity at the lowest temperature is 9.0±0.6 meV Å, in reasonable agreement with the Lorentzian fits, considering that a symmetric velocity for both branches is assumed. The spin-wave velocity shows only minor changes with
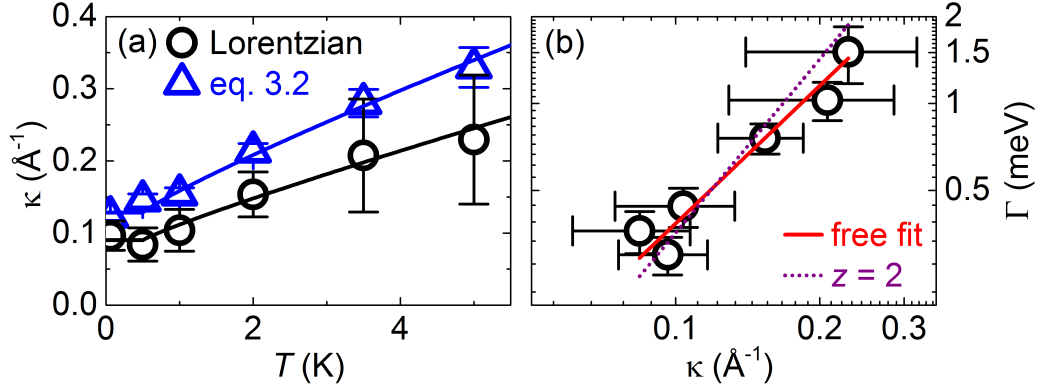
Figure 3.10: (a) Fitted Q-width κ (FWHM) of the magnetic fluctuations in S-type CeCu$_2$Si$_2$ as a function of temperature ($B = 1.7$ T). The black circles are extracted from Lorentzian fits to the constant-E scans, while the blue triangles are from fits according to equation 3.2. The lines show power-law fits, assuming a constant value for κ below 0.5 K. (b) Energy width Γ (FWHM, from [ASS+11]) plotted over Q-width κ (FWHM, Lorentzian fits) in a log-log plot. Two power-law fits are shown, one with free exponent (red line) and one where the exponent is fixed to $z = 2$ (purple dotted line).

temperature, with a slight increase towards higher temperatures; the centre of the dispersion shifts towards higher h values. Thus, the results from fits following equation 3.2 give the same trends as the Lorentzian fits. In figure 3.10(a), the fitted width κ for both fit procedures is compared. The absolute values differ, since Γ in equation 3.2 influences the fit of κ; here values for Γ are taken from the measurements of Arndt *et al.* [ASS+11].

Both fitting procedures show that the correlation length $\xi = 2/\kappa$ increases towards low temperatures, but does not diverge. At the lowest temperature the correlation length was fitted to be 20 Å (Lorentzian fits) or 16 Å (equation 3.2), slightly below the value in the antiferromagnetic state. The finite value of κ at low temperatures is in line with the finite value of the energy width Γ reported in reference [ASS+11]. There it was explained by the fact that the sample is not located exactly at the quantum critical point in the phase diagram, but slightly further on the paramagnetic side, so that the Fermi-liquid regime is entered at low temperatures.

This might also imply that there is a certain low-temperature interval where the values of κ and Γ are constant, as is suggested by both datasets (compare figure 3.10(a) and reference [ASS+11]). Then, a power-law fit ac-

cording to

$$\kappa = \kappa_0 + a \cdot (T - T_0)^b \quad \text{or} \quad \Gamma = \Gamma_0 + a \cdot (T - T_0)^b \tag{3.3}$$

does not necessarily yield $T_0 = 0$. Indeed, the temperature dependence of κ cannot be described well by a power-law fit with $T_0 = 0$. Instead, a good description of the data, for both sets of κ values, can be obtained by setting $T_0 = 0.5$ K. Then the power-law exponent is fitted to be 0.90 ± 0.27 (κ from Lorentzian fits) or 0.88 ± 0.26 (κ from fits with equation 3.2). It is thus compatible with the exponent of 0.75 expected in the Hertz-Millis-Moriya scenario [Her76, Mil93, MT95]. However, this exponent cannot be compared directly to the exponent for Γ, 1.38 ± 0.16, given in reference [ASS$^+$11], since the authors assumed $T_0 = 0$. Re-fitting the dataset for Γ with finite T_0 strongly modifies the exponent and thereby also the value of z.

A more reliable procedure to obtain z is a direct comparison of κ and Γ, as shown in figure 3.10(b). This does not depend on any model for the temperature dependence of κ and Γ and thus avoids introducing further parameters. If Γ scales with κ (compare equation 2.11), a linear dependence is expected in a log-log plot. This is roughly confirmed by the data. A fit according to $\Gamma = a \cdot \kappa^z$ yields $z = 1.59\pm0.22$, slightly smaller than the value of 2 given by Hertz [Her76]. The fit is shown by the red line in figure 3.10(b). For comparison, also a fit with $z = 2$ is shown in purple, which is still compatible with the data. The same analysis has also been done for the other set of κ values, with no remarkable differences.

The results discussed here, in combination with the analysis in reference [ASS$^+$11], present a direct measurement of the dynamical critical exponent in a quantum phase transition. Unfortunately, the measurements suffer from multiple difficulties that limit the certainty of the analysis: The temperature range for the exponent fit is confined from above by the Kondo scale (compare reference [ASS$^+$11]) and from below by the onset of Fermi-liquid behaviour, leaving a rather narrow temperature window for the fit. In this window, the change in κ is only about a factor of 2 (the relative change observed in Γ is much larger). Such a small effect is difficult to measure with high precision, given the small signal-to-background ratio of inelastic scattering for S-type $CeCu_2Si_2$. Despite these limitations, the analysis suggests that dynamical scaling exists in S-type $CeCu_2Si_2$, and the power-law exponent is roughly as expected in the Hertz-Millis-Moriya scenario. It is possible that a larger value of z, closer to $z = 2$, would be observed for a sample with $r = r_c$, while this sample is located slightly too far on the Fermi-liquid side of the phase diagram.

3.5 Inelastic magnetic response in A/S-type $CeCu_2(Si_{0.98}Ge_{0.02})_2$

So far, the inelastic response in the antiferromagnetic phase and the superconducting phase have been discussed for samples that display (mainly) one of the two groundstates. In A/S-type $CeCu_2Si_2$, both phases can be found in the same sample: A magnetic phase is entered at $T_N \approx 0.8$ K, followed by a superconducting phase at lower temperatures. In neutron diffraction experiments, both on $CeCu_2Si_2$ and on $CeCu_2(Si_{0.98}Ge_{0.02})_2$ samples [SNT+07, FSS+07, ASB+09, Arn10], it was found that superconductivity and magnetism compete with each other on a microscopic level, since the Bragg peak intensity is suppressed below T_c. Inelastic neutron scattering has so far not been performed.

The aim of the experiments presented in this section was to get a first impression of the spectral response of an A/S-type crystal, and to compare the spectra in both phases to those of the A-type and the S-type samples. For the superconducting gap in A/S-type $CeCu_2Si_2$, one difference is expected in comparison to S-type $CeCu_2Si_2$: While the transition from the paramagnetic to the superconducting state is second order, the transition from the antiferromagnetic to the superconducting state is assumed to be first order if T_c is not much smaller than T_N [KM88]. This was confirmed in thermodynamic measurements in reference [Arn10].

Details of the experiments

The first neutron measurement of the A/S-type crystal 83105_01 was done at IN12, Grenoble, with the same set-up as the experiment with the A-type crystal (section 3.3). For the measurement of the spectra the final neutron wave vector was reduced from $k_f = 1.15$ Å^{-1} ($\lambda_f = 5.45$ Å, $E_f = 2.74$ meV) to $k_f = 1.07$ Å^{-1} ($\lambda_f = 5.87$ Å, $E_f = 2.37$ meV) to resolve the superconducting gap: This improved the energy resolution at $E = 0$ from 65 μeV to 50 μeV. The sample had a mass of 4.05 g and a composition $CeCu_2(Si_{0.98}Ge_{0.02})_2$; the lattice constants were determined to be $a = 4.09$ Å and $c = 10.00$ Å.

A second measurement on the same crystal was performed at the triple-axis spectrometer V2 (FLEXX) at the BER II reactor at the Helmholtz-Zentrum Berlin. A dilution refrigerator with a base temperature of 60 mK was used, as in the IN12 experiment. The set-up at V2 also allowed a magnetic field of up to 5 T vertical to the $(h\ h\ l)$ scattering plane to be applied. Furthermore, the bulk AC susceptibility of the sample was measured simultaneously to the neutron scattering data. The V2 set-up uses a doubly focussing graphite (002) monochromator, a horizontally focussing graphite

(002) analyser and a ^{3}He detector. Higher order contamination is avoided by a velocity selector in front of the monochromator, and a collimator is installed in front of the analyser mainly for reducing the background. The data were normalised to a monitor in front of the sample. Two different wavelengths were set during the experiment, with fixed final neutron wave vector k_f in both cases: $k_f = 1.5$ Å^{-1} ($\lambda_k = 4.19$ Å, $E_f = 4.66$ meV) was used for elastic scans across the magnetic Bragg peak and $k_f = 1.12$ Å^{-1} ($\lambda_f = 5.61$ Å, $E_f = 2.60$ meV) was used for inelastic measurements. At $k_f = 1.12$ Å^{-1}, the energy resolution at the elastic line was 65 μeV.

The heat capacity was, as for the A-type crystal, first measured in a PPMS on a fraction of the sample and then in a SHE dilution cryostat for the whole crystal. A magnetic field was applied along the [110] direction. To improve cooling, the sample was linked to the thermal bath by three gold wires, which resulted in sample base temperatures below 60 mK.

Results

In the A/S-type crystal 83105_01, antiferromagnetic order was observed with the ordering vector $\tau = (0.215\ 0.215\ 0.52)$, which is temperature-dependent above 400 mK, in agreement with other A- and A/S-type crystals (references [SNT+07, FSS+07, ASB+09, Arn10] and section 3.3). Again, the measurements could best be performed in the second Brillouin zone. Figure 3.11 shows the integrated intensity of the magnetic Bragg peak in comparison with the heat capacity and AC susceptibility data measured on the entire crystal. The heat capacity shows two transitions in zero field, the antiferromagnetic transition at $T_N \approx 720$ mK and the superconducting transition at $T_c \approx 600$ mK; the latter is also clearly seen in the susceptibility. The superconducting transition is suppressed in a field of 2 T ($B \parallel [110]$), while T_N is only slightly shifted. For the neutron data, figure 3.11 includes both the measurement at IN12 (only zero field) and the measurement at V2 ($B = 0$ and $B = 2$ T). The integrated intensity is gained from Lorentzian fits to ω-scans, which also account for the instrument resolution by a convolution with a Gaussian function of appropriate width. The two datasets have been scaled to match at the lowest measured temperatures for $B = 0$; a normalisation to the incoherent elastic line is not possible since the data at V2 contain a rather large background contribution.

The intensity of the magnetic Bragg peak is strongly reduced in the superconducting phase, indicating that in this crystal, as in the other crystals studied by neutron scattering, magnetism and superconductivity do not coexist on a microscopic level [SNT+07, FSS+07, ASB+09, Arn10]. For the crystal under investigation here, the intensity of the magnetic Bragg peak
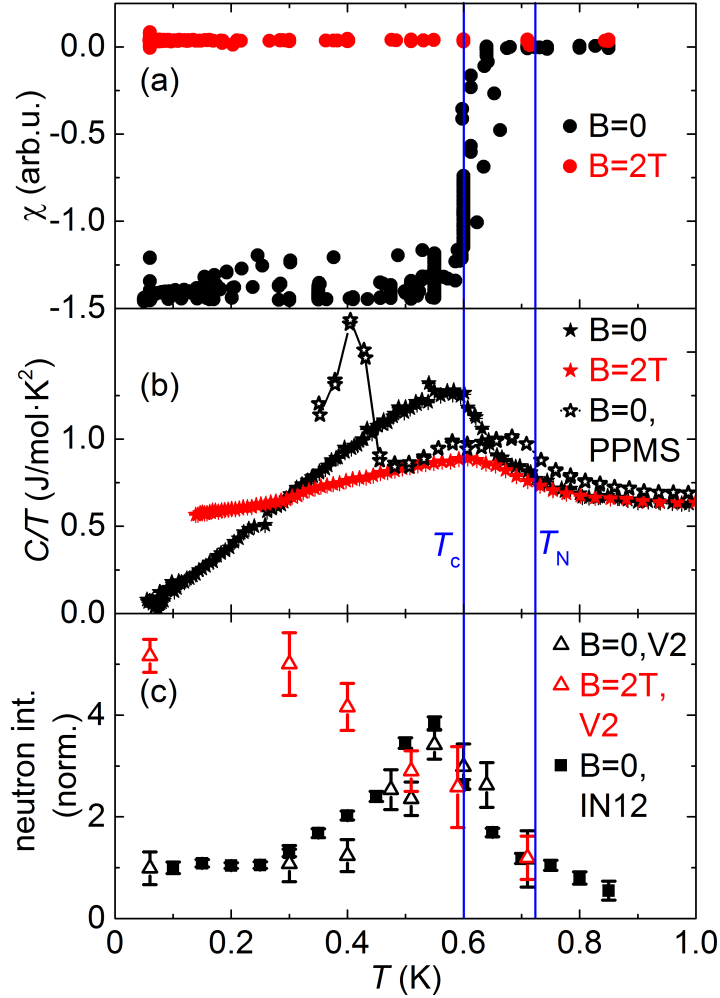
Figure 3.11: Phase transitions of A/S-type CeCu$_2$(Si$_{0.98}$Ge$_{0.02}$)$_2$: (a) AC susceptibility data, which were measured simultaneously with the neutron data at V2. The graph includes data points collected over a whole week, which scatter due to limited long-term stability of the set-up. (b) Heat capacity, plotted as C/T, of the entire crystal (filled stars, SHE data) and of a 0.1% fraction of the sample (open stars, PPMS data). (c) Normalised, integrated intensity of the magnetic Bragg peak at $Q_{AF} = (0.215\ 0.215\ 1.48)$, measured at IN12 (filled squares) and V2 (open triangles). Data measured at zero field are plotted in black, those measured at $B = 2$ T are plotted in red. Blue vertical lines mark the transition temperatures in zero field.

at low temperatures is not completely suppressed, but reduced to 25% of its maximum value. This indicates that part of the sample stays magnetically ordered well below T_c. In a magnetic field of 2 T, the intensity rises to a saturation value at low temperature which is around 40% larger than the maximum value in zero field. Assuming that the saturation value in 2 T is not strongly suppressed compared to a putative zero-field, low-temperature AF state, the magnetic volume fraction of the crystal for $T \rightarrow 0$ is around 15%. This fraction is larger than what was observed in references [SNT$^+$07] and [ASB$^+$09], where all or nearly all the intensity of the magnetic Bragg peak had vanished at the lowest temperature. This hints towards a stronger inhomogeneity in the new sample, which causes different parts of the crystal to have slightly different stoichiometry and thus potentially different ground states. This is more likely to happen in larger samples, such as the crystal used in this work.

Disorder also appears to be relevant for the transition from the antiferromagnetic to the superconducting phase. For the crystals previously studied, both heat capacity measurements [ASB$^+$09, Arn10] and muon spin rotation [SAA$^+$06] give good evidence that the transition is first order. However, the heat capacity data of this crystal show a much broader transition at T_c, which is also not symmetric, as expected for a first-order transition. Furthermore, the magnetic Bragg peak continues to gain intensity below $T_c \approx 600$ mK. The reduction in intensity only starts below 550 mK and then proceeds gradually, reaching the low-temperature value at 250 mK. In contrast, in the earlier studies [SNT$^+$07, ASB$^+$09], the maximum of the magnetic intensity at zero external field coincides with T_c, and a sharp drop-off is observed below. Two possible explanations exist for the deviating behaviour of this sample: The transition is second order, possibly disorder-induced; or the transition is first order, with a very large distribution of ordering temperatures. The PPMS-measurement of a small fraction of the crystal (4 mg or 0.1% of the crystal) indicates that the second scenario is realised. Here, a sharp, symmetric transition into superconductivity is observed, which is as low as 420 mK. Still, the maximum in the heat capacity data and the rather sharp transition observed in the AC susceptibility imply that a significant part of the sample becomes superconducting at ≈ 600 mK.

The width of the antiferromagnetic Bragg peak can give insight into the size of magnetic domains in the dominantly superconducting state. Surprisingly, the width is constant below 500 mK, where it seems to be resolution-limited. Antiferromagnetic domains, even at lowest temperatures, therefore have a size $\gtrsim 200$ Å, similar to the A-type crystals.

At V2, the magnetic order was studied also as a function of field. In figure 3.12, the integrated intensity of the magnetic Bragg peak is shown
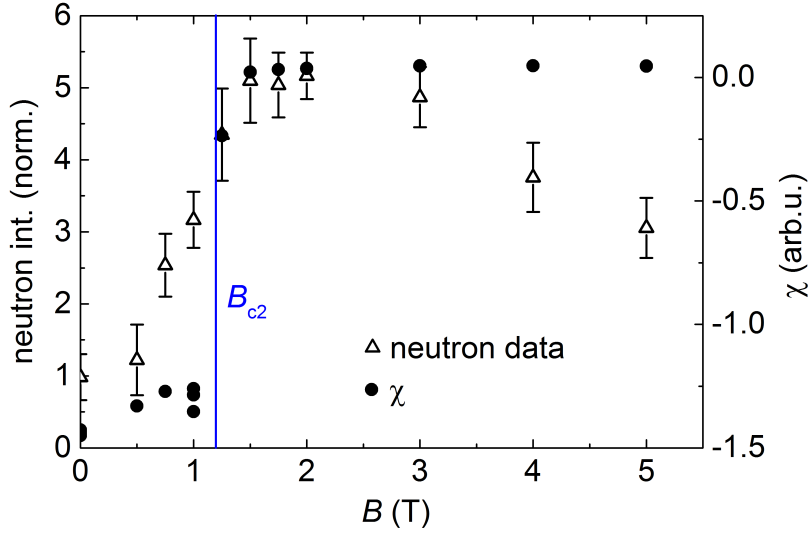
Figure 3.12: Normalised intensity of the magnetic Bragg peak of A/S-type CeCu$_2$(Si$_{0.98}$Ge$_{0.02}$)$_2$, measured at V2, compared with the AC susceptibility χ which was measured simultaneously. The blue vertical line marks the critical field B_{c2}, deduced from the jump in the AC susceptibility.

together with the AC susceptibility. A critical field B_{c2} of around 1.2 T can be deduced from the jump in the AC susceptibility data, in good agreement with other A/S-type samples [Arn10]. In larger fields $\gtrsim 3$ T, a suppression of the antiferromagnetic order parameter is visible in the neutron data.

Now the inelastic response of the A/S-type crystal shall be discussed. At IN12, spectra at zero field have been measured with $k_f = 1.15$ Å^{-1} and $k_f = 1.07$ Å^{-1}. The following discussion will be based on the latter dataset, since the analysis of the superconducting gap can be done more thoroughly with the high-resolution data. In figure 3.13, the inelastic response at 100 mK, 350 mK, 650 mK and 850 mK is shown, i.e. in the superconducting state well below T_c, in the superconducting state closer to T_c, in the antiferromagnetic state above T_c and in the paramagnetic state. The figure includes fits with different functions for the different states, which will be explained in the following.

Above T_c, the response is quasi-elastic and can thus be fitted with a Bose-weighted Lorentzian function (equation 3.1). As in section 3.3, the total fit function consists of the quasi-elastic Lorentzian, convoluted with a Gaussian for the resolution, an elastic magnetic signal and an incoherent signal. The latter is mainly elastic, but also includes small background features at
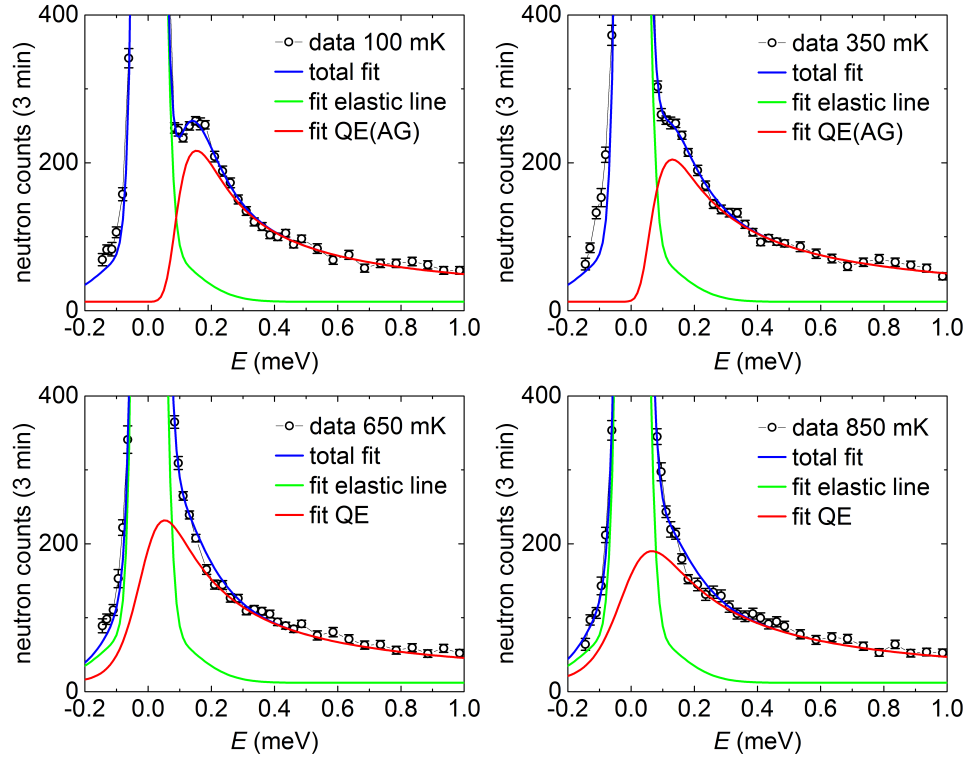
Figure 3.13: Spectra of A/S-type $CeCu_2(Si_{0.98}Ge_{0.02})_2$ at the magnetic ordering vector, measured at IN12. The response in the superconducting phase (at 100 mK and 350 mK) is gapped, with a gap that is smeared out as described in the theory of Abrikosov and Gorkov (AG). The response is quasi-elastic (QE) in the antiferromagnetic (650 mK) and the paramagnetic (850 mK) state. Shown in blue is the total fit function, in red the inelastic magnetic response, and in green the elastic contribution, which consists of an incoherent background plus an elastic magnetic component.

finite energy transfers, which have been fitted to a spectrum taken at the position (0.1 0.1 1.6). Such a fit function gives a good description of the data at 850 mK and 650 mK (see figure 3.13), with a fitted width and intensity that are very similar to those of the A-type crystal (Γ(850mK) = 0.265$\pm$0.016 meV, Γ(650mK) = 0.202$\pm$0.013 meV).

Below T_c, the response is gapped, as in S-type CeCu$_2$Si$_2$ [SAF$^+$11]. Stockert *et al.* have accounted for the modified density of states in the superconducting phase by multiplying the Lorentzian part of the fit function by $E/\sqrt{E^2 - E_\mathrm{gap}^2}$ for $E \geq E_\mathrm{gap}$ and with zero otherwise (see [SAF$^+$11] supplementary material). However, a fit function of this type does not give a satisfactory description of the spectra of the A/S-type sample, since the measured intensity in the gap is too high and the intensity at $E \geq E_\mathrm{gap}$ is too low. A first idea to account for this deviation is to assume that the inelastic signal is a superposition of a gapped response (from the superconducting majority phase) and a quasi-elastic response (from the antiferromagnetic minority phase). In such a fit, it is sensible to fix the intensity of the quasi-elastic signal relative to the integrated intensity of the magnetic Bragg peak. In the A-type sample, the inelastic magnetic intensity at lowest temperatures is around twice as large as the elastic magnetic intensity, and it is assumed that this ratio holds for the A/S-type sample as well. Thus, the estimated inelastic signal from the antiferromagnetic grains can be added as a further background signal and a fit attempted of the remaining inelastic intensity with a gapped function. However, this procedure also does not lead to good fits to the data.

Instead, it is necessary to assume that the gap in the density of states is smeared out. For this purpose, the theory of Abrikosov and Gorkov (AG) can be used. They developed an expression for the density of states of a superconductor in the presence of magnetic impurities [AG61]. An analytic expression was later given in reference [ST08]; here the density of states is calculated as $\mathrm{Re}(u/\sqrt{u^2 - 1})$ with

$$
\begin{aligned}
u \;=\; & \frac{r}{2} + \frac{\sqrt{3}}{6} \cdot \sqrt{A + B/C + C} \\
& - \frac{\sqrt{3}}{6} \cdot \sqrt{2A - B/C - C - \frac{6\sqrt{3}(1+\alpha^2)r}{\sqrt{A + B/C + C}}},
\end{aligned}
\tag{3.4}
$$

where r is the energy given in units of the gap size E_gap and α is the Abrikosov-Gorkov parameter. A,B and C are lengthy analytic expressions of α and r, which can be found in reference [ST08]. The AG equation for the density of states can be multiplied with the quasi-elastic Lorentzian 3.1 to fit the magnetic response in the superconducting state. The function then

includes the fit parameters E_{gap} and α. α is zero in case of a BCS-type gap in the density of states, and takes values of the order of 0.1 to 1 in the presence of magnetic impurities. The theory was developed for randomly distributed paramagnetic impurities, while the sample actually includes domains of antiferromagnetic order. Nevertheless, an Abrikosov-Gorkov-type fit gives a good description of the data in the superconducting state. In figure 3.13, fit functions of this type are shown for the data at 100 mK and 350 mK. Again, it would be possible to include a fixed contribution from the antiferromagnetic impurity phase. However, this does not significantly alter the fit quality or the fitted parameters, so that this contribution will be neglected in the following.

At 100 mK, a gap $E_{\text{gap}} = 0.15\pm0.03$ meV is fitted, with an AG parameter $\alpha = 0.25\pm0.08$ and a Lorentzian width $\Gamma = 0.21\pm0.06$ meV. The values for α and Γ seem reasonable, which supports the use of this particular fit function. This fit is shown in red in figure 3.13. The gap in A/S-type CeCu$_2$Si$_2$ is thus slightly smaller than the gap of 0.2 meV observed in S-type CeCu$_2$Si$_2$ [SAF$^+$11].

At 350 mK, a free fit with the AG equation yields $E_{\text{gap}} = 0.11\pm0.03$ meV, $\alpha = 0.32\pm0.22$ and $\Gamma = 0.24\pm0.05$ meV. A larger value for α, corresponding to an increased number of magnetic impurities, is expected due to the increase of intensity of the magnetic Bragg peak. However, an increased value for Γ, compared to both the superconducting and the antiferromagnetic state, does not appear reasonable. Therefore, it is more constructive to perform a fit with fixed $\Gamma = 0.21$ meV, as there is a strong interdependence between Γ, α and E_{gap} (in figure 3.13, the free fit is shown, but the form of the total fit function looks very similar for both fits). Then α takes the value $\alpha = 0.43\pm0.16$ and the gap is fitted to be $E_{\text{gap}} = 0.13\pm0.02$ meV. This relatively small reduction in the gap size compared to 100 mK would be in line with a first-order transition.

At V2, the inelastic response of the A/S-type crystal was also measured in field. Due to a lower flux, and thus longer count rates, spectra were measured only for $E \leq 0.3$ meV. For these smaller energy windows and due to increased scattering of the data, the fits obtained are less reliable, so that the V2 data will only be discussed qualitatively. Figure 3.14 shows the spectra measured at zero field, 1 T and 2 T. To serve as a guide to the eye, fit functions are included which take the width Γ from the IN12 fits. In the zero field data, the dip around 0.14 meV clearly shows the presence of a superconducting gap. This is not seen in the data at 1 T and 2 T, where the count rates are higher for $E < E_{\text{gap}}$. At 2 T, the sample is in the antiferromagnetic state, so that a quasi-elastic response is expected. However, at 1 T, the measurement of the susceptibility and the magnetic Bragg peak (figure 3.12)
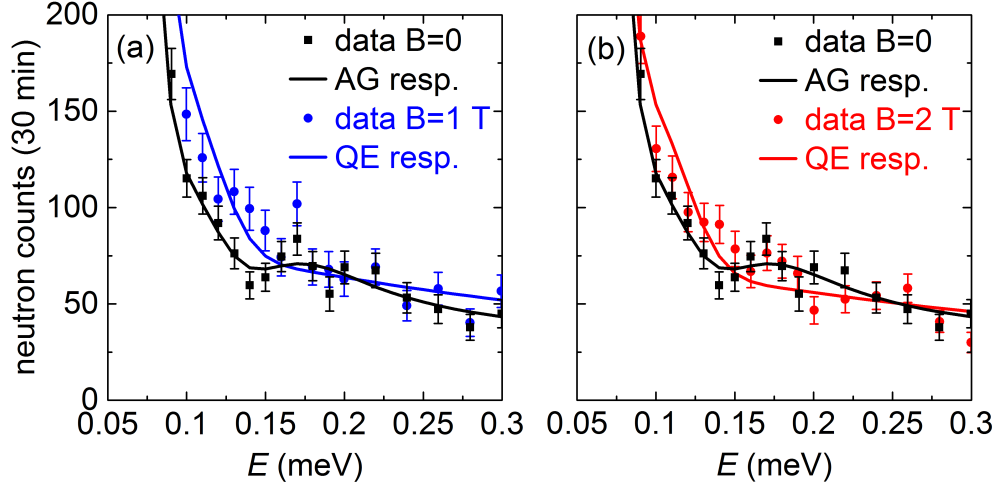
Figure 3.14: Spectra of A/S-type $CeCu_2(Si_{0.98}Ge_{0.02})_2$ at the magnetic ordering vector, measured at V2 ($T = 100$ mK). Zero field data are compared to the data at (a) 1 T and (b) 2 T. Fit functions according to the AG theory ($B = 0$) or quasi-elastic functions ($B = 1$ T and 2 T) are shown as a guide to the eye; these are not free fits, but fix the width Γ to the value fitted in zero field to the IN12 data.

suggest that the sample is still in the superconducting state. The seemingly quasi-elastic response therefore indicates that either the gap size is strongly reduced, or that there is a large concentration of in-gap states. The second explanation appears more conclusive, as a gradual closing of the gap should not be observed for a first-order transition, but a large number of in-gap states is expected for a type-II superconductor close to B_{c2}.

For the A/S-type sample, the inelastic response is very similar to the A-type sample for $T > T_c$, and somewhat similar to the S-type sample for $T < T_c$. The smearing out of the gap might not be an intrinsic effect of A/S-type $CeCu_2Si_2$, but due to the disorder in this particular crystal. Similarly, it is difficult to judge whether the transition into the superconducting state is first order because of the observed distribution of transition temperatures.

Chapter 4

The interplay of geometric frustration and Kondo physics in CePdAl

4.1 The compound CePdAl

The general route to quantum criticality in heavy-fermion systems is the suppression of magnetic order via tuning of the Kondo effect, which counteracts the magnetic exchange interaction. However, it is also possible that an ordered magnetic phase is suppressed by the competition of magnetic interactions, i.e. magnetic frustration. Theoretically, this new route to quantum criticality has been discussed in the framework of a new axis to the Doniach phase diagram, which measures frustration [Si06, Voj08, CN10].

From an experimental point of view, the question of suitable model systems remains to be settled. General concepts for frustration are based on localised spins in insulators, i.e. they require the presence of direct exchange, super- or double-exchange. In 4f-based intermetallics, however, magnetic order is mediated by the RKKY interaction, which has a long spacial extension (equation 2.22). Furthermore, the applicability of the frustration parameter, the ratio of the Weiss temperature to the Néel temperature, is questionable. The frustration parameter implies that magnetic frustration is the only way to suppress the ordering temperature compared to the magnetic exchange interactions, but metals with Kondo interaction frequently have reduced Néel temperatures even in the absence of frustration.

CePdAl might be a good model system for frustrated heavy fermions, as there is microscopic evidence for the presence of (partial) frustration: In powder neutron diffraction experiments it was shown that only two thirds of the cerium moments participate in the long-range magnetic order below
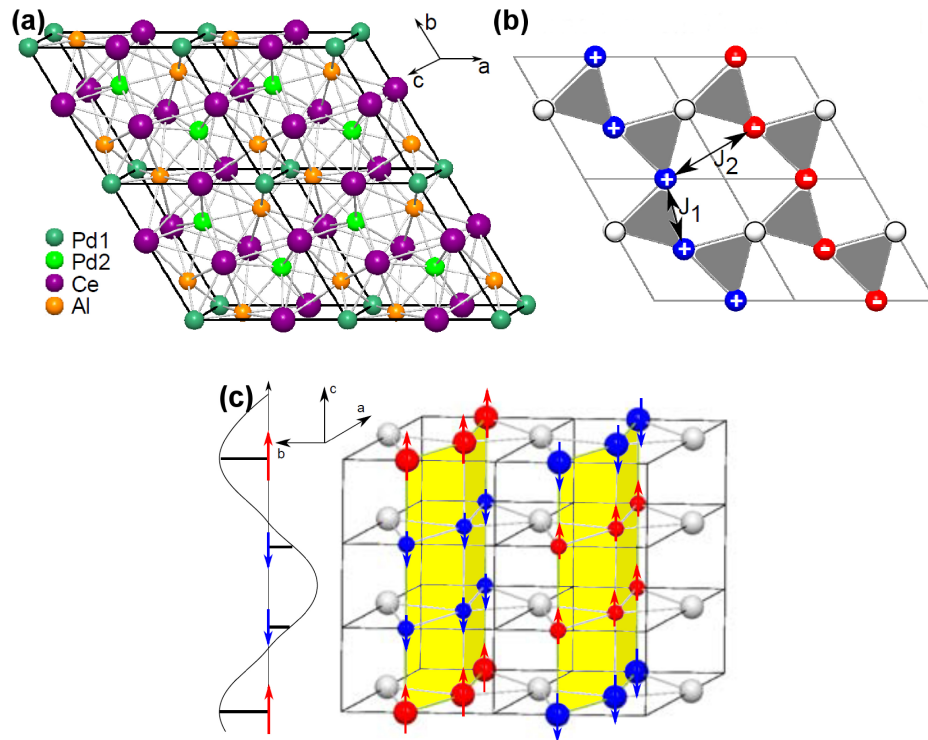
Figure 4.1: (a) Hexagonal crystal structure of CePdAl; lattice constants are $a = 7.20$ Å and $c = 4.24$ Å [DEM$^+$96]. (b) Schematic view of the magnetic order in the *ab*-plane. (c) Schematic 3D view of the magnetic order, showing antiferromagnetically ordered planes separated by frustrated cerium moments. Images by V. Fritsch, (b) and (c) reprinted from reference [FSH$^+$15] with kind permission of EPJ.

$T_{\mathrm{N}} = 2.7$ K [DEM$^+$96, KDKvdB02]. This is despite the fact that all cerium atoms sit in crystallographically equivalent sites, and their high-temperature magnetic behaviour is identical [OMN$^+$08]. The frustration is presumably caused by a combination of the hexagonal crystal structure [XSH94], with a Kagomé-like arrangement of the cerium atoms, and competing interactions between the Ce moments in the ab-plane. In a 2-dimensional model, neglecting the c-direction, it was suggested that the nearest-neighbour interaction Ce-Ce is ferromagnetic and the next-nearest neighbour interaction antiferromagnetic [NnRLC97]. This leads to ferromagnetic chains that are antiferromagnetically coupled, but separated by frustrated moments. Figure 4.1 shows models of the magnetic structure, which can be described by the ordering wave vector $(0.5\ 0\ \tau_l)$ with $\tau_l \approx 0.35$. Since τ_l is incommensurate, it is more difficult to establish a model that includes the out-of-plane component of the magnetic order. In figure 4.1 (c) a sinusoidal modulation along the c-axis is shown, as proposed by Dönni *et al.* [DEM$^+$96]. However, since τ_l is not exactly 1/3, this model requires a different size of the magnetic moments for each ab-plane. Alternatively, from a more localised point of view one can assume stacking defaults along c which cause τ_l to be incommensurate.

The Kondo properties of CePdAl are well established from a maximum in the resistivity and an enhanced specific heat coefficient of around $\gamma_0 = 270$ mJ/(mol·K^2) [KMMS94, SJL$^+$94, GHU$^+$02, FHB$^+$13]. In the paramagnetic phase, Curie-Weiss behaviour is observed, with an effective moment of 2.53 μ_{B} corresponding to the Ce^{3+} ion [DEM$^+$96], or slightly reduced at intermediate temperatures of order 100 K due to the crystal electric field [FHB$^+$13]. At all temperatures, the crystal field causes a strong magnetic anisotropy with the c-axis as the easy axis [OKH$^+$96, DEM$^+$96].

The Néel temperature of CePdAl can be suppressed to zero by application of either pressure [TMKM96, GHU$^+$02, PMA$^+$07], magnetic field [GHU$^+$02, PMA$^+$06] or Ni substitution on the Pd site [FBG$^+$14]. In magnetic fields close to the critical field, metamagnetic first-order transitions occur, making the observation of a field-induced quantum critical point problematic. In the pressure and substitution studies, however, there is good evidence that a quantum critical point is reached at around 0.9 GPa or 14% Ni substitution, respectively. Fritsch *et al.* [FBG$^+$14] observed a logarithmic increase of C/T at low temperatures in CePd$_{0.86}$Ni$_{0.14}$Al samples, as predicted for a 2-dimensional QCP within the Hertz-Millis-Moriya scenario [Mil93]. The proposed explanation for the appearance of 2-dimensional magnetic fluctuations in a 3-dimensional magnetic structure are the planes shown in figure 4.1, which are separated by frustrated cerium moments. Thus, the frustration would enter the quantum critical behaviour of the system by changing the effective dimensionality. However, it is also possible that the Hertz-Millis-

Moriya scenario is not applicable in the presence of strong frustration, and new theories are required to explain the observations.

For CePdAl under pressure, it was found that the magnetic ordering vector is stable for all pressures $p < p_c$ [PMA$^+$07]. For CePdAl under chemical pressure, i.e. Ni substitution, no studies have been published so far. The investigation of the influence of Ni on the magnetic order will form part of the following chapter. All neutron experiments were performed on single crystals so that anisotropy effects can be studied. First a detailed analysis of the magnetic order in the parent compound CePdAl is given.

4.2   Magnetic order in CePdAl

Details of the diffraction experiments

The data discussed in this section originated from three different single crystal neutron diffraction experiments, two at the diffractometer D10 (ILL, Grenoble) and one at the diffractometer RESI (FRM2, Munich). The first of the D10 measurements was performed by Sarah Woitschach. For all experiments, the same 1.8 g single crystal was used. It was cut out of the batch VF541, which was synthesised by Veronika Fritsch by Czochralski growth at Karlsruhe University. The sample was glued to a copper sample holder on a polished surface perpendicular to the [110] direction. Thus, the scattering plane was the $(h\ 0\ l)$ plane, which includes the magnetic ordering vector $(0.5\ 0\ \tau_l)$, $\tau_l \approx 0.35$.

The experiments at D10 were performed with an incident neutron wavelength of $\lambda = 2.36$ Å. In the first experiment, a ^{4}He flow cryostat was used which allowed cooling to a base temperature of 1.8 K and yielded a large flexibility for measuring different magnetic reflections $(h\pm0.5\ k\pm0.5\ l\pm\tau_l)$, also outside of the scattering plane. The second D10 experiment was performed using a conventional ^{4}He bath cryostat with a base temperature of 1.6 K. While the cryostat could not be tilted, the detector could be rotated out of plane by up to 15°, which allowed scans along k across the $(h\pm0.5\ 0\ l\pm\tau_l)$ reflections to be measured. The detector was a 8x8 cm^2 area detector, which was used like a single counter by integration over the central section.

The experiment at RESI was performed with a smaller wavelength ($\lambda = 1.03$ Å) and at lower temperatures using a ^{3}He cryostat (base temperature 0.43 K). The RESI set-up yields a very high momentum resolution. The detector was a single counter. The measurement of reflections outside of the scattering plane was not possible.

Fits of the D10 data yielded a width of around 0.3° for the nuclear Bragg peaks. The measurement at RESI showed that all peaks, both nuclear and

magnetic, were split into (at least) three different reflections, each of which is around 0.24° wide. They can be attributed to grains in the crystal that are missaligned by a fraction of a degree. This splitting can be accounted for by peak functions that consist of a sum of three peaks, whose splitting and intensity ratio is fixed and whose width is identical. All fit results presented for this crystal refer to the averaged fitted position and the summed fitted intensity of the three contributions.

The measured data were normalised to a monitor that was placed in the beam in front of the sample. Comparison between experiments performed at different instruments was done by normalisation to the integrated intensity of nuclear reflections. Thus, it was ensured that the datasets from D10 and RESI are consistent. Nevertheless, the datasets will mainly be looked at separately in the following. The analysis of phenomena around the Néel temperature will be based on the D10 datasets, since they have a better signal-to-background ratio. The discussion of the ordered phase can be done more accurately based on the data measured at RESI, due to the improved Q-resolution and the lower base temperature.

Results

The first step of the single crystal experiments on CePdAl was to compare the results to those that were reported from neutron powder diffraction [DEM+96, KDKvdB02]. Therefore, a variety of magnetic Bragg peaks were recorded by performing ω scans at the expected positions at $T = 1.8$ K (well below $T_N = 2.7$ K). The measured positions are in good agreement with the ordering vector $(0.5\ 0\ \tau_l)$ found in the powder measurement (or, equivalently, $(0\ 0.5\ \tau_l)$ or $(0.5\ 0.5\ \tau_l)$). The comparison of the intensity of different magnetic Bragg peaks showed that reflections with a large l-component are strongly suppressed, which confirms that the spins are oriented along the c-axis. Along the h- or k-direction the intensity decrease with increasing momentum transfer is moderate, following the magnetic form factor.

Dönni *et al.* also reported that reflections at the positions $(^h/_2\ -h\ l{\pm}\tau_l)$ are forbidden in CePdAl [DEM+96], which is related to the absence of an ordered magnetic moment on one out of three cerium ions. However, in the single crystal data these reflections do appear, even though they are about an order of magnitude weaker than other magnetic reflections. One example is shown in figure 4.2. This suggests that those cerium ions which are supposed to be paramagnetic in the ordered phase actually do have a finite ordered moment, at least on the time scale of the neutron experiment ($\approx 10^{-12}$ s). Considering that the intensity is proportional to the square of the ordered moment, the ordered moment on the third cerium ion is significant. However,
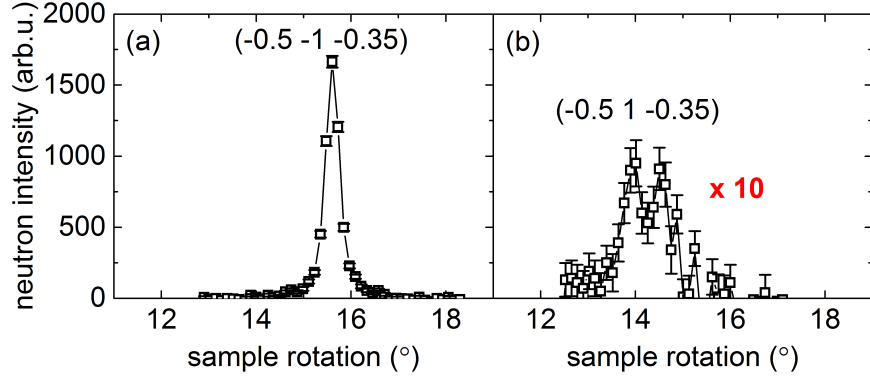
Figure 4.2: A magnetic Bragg peak of CePdAl (a), compared to a forbidden reflection (b). The Q vectors differ only in the k component, which is $2h$ for the allowed reflection and $-2h$ for the forbidden reflection. The background has been subtracted for both scans. They are plotted on the same intensity scale, but the data of the forbidden reflection have been multiplied by a factor of ten. The peak splitting is caused by the mosaicity of the sample.

the order is apparently short-ranged, since the reflections are broadened.

As a next step, the temperature dependence of the magnetic Bragg peaks was studied. The single crystal measurement made it possible to look at the anisotropy of the reflections by taking scans along the three principal reciprocal space directions. Such scans were performed at temperatures between 0.43 K and 10 K (for the lowest temperatures, scans along k are missing, since the experiment at RESI did not allow out-of-plane measurements). Because the incommensurate component τ_l of the ordering vector is temperature dependent, scans along l were measured first so that the scans along h and k could be done at the value of l that corresponds to the maximum intensity. All scans were fitted with Voigt functions, where the Gaussian component describes the resolution of the diffractometer and the Lorentzian component the correlation length of the magnetic correlations. The resolution width is not known exactly, since it depends on 2θ and is thus not identical to the width of the nuclear reflections. This uncertainty necessarily affects the absolute values of the Lorentzian width (and thus correlation length), especially when Lorentzian and Gaussian widths are comparable in magnitude.

The position along l as well as the magnetic moment per cerium atom, extracted from the Voigt fits to the magnetic Bragg peak $(0.5\ 0\ \tau_l)$, are shown in figure 4.3. Since the data do not yield absolute units, the square root of the integrated intensity is plotted and normalised it to the value at lowest temperature. Both the incommensurate component, including the position
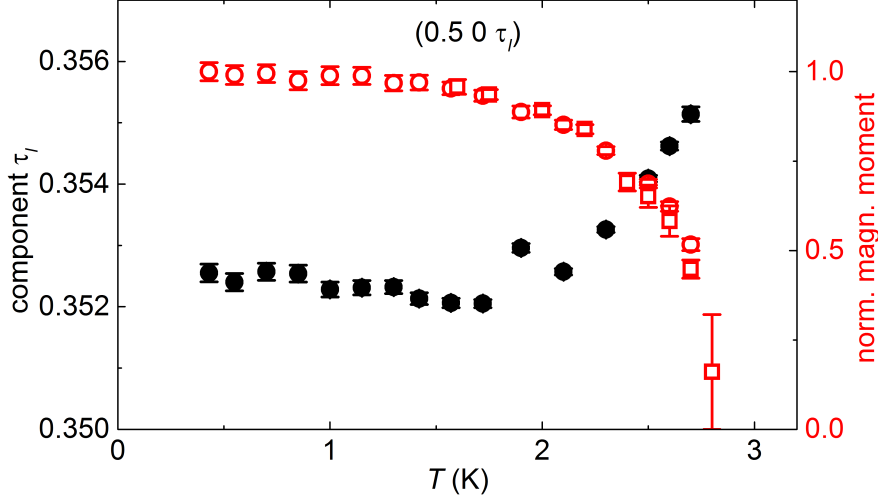
Figure 4.3: Fitted incommensurate component τ_l and normalised magnetic moment per cerium of CePdAl, derived from l-scans over the $(0.5\ 0\ \tau_l)$ reflection. Circles depict data from RESI while squares show data from D10. The data shown here refer to the long-range magnetic order.

of the lock-in value, and the ordered moment are in very good agreement with the powder data from reference [KDKvdB02]. The respective fit results for the fits along h and k are not shown, since the position is temperature independent and the intensity follows the same trend as the l-scans.

The shape of the magnetic signal has an interesting temperature dependence, which has not been observed by powder neutron diffraction. This can be seen in figure 4.4, which shows exemplary scans along l around the position $(0.5\ 0\ \tau_l)$, $\tau_l \approx 0.35$, at different temperatures. In the following paragraphs the temperature dependence of the magnetic signal is discussed, starting from temperatures above the Néel temperature and then gradually lowering the temperature.

Short-ranged magnetic correlations at $(0.5\ 0\ \tau_l)$ could be traced up to a temperature of 5 K, which is almost a factor two larger than the ordering temperature. As an example, a scan at 3.1 K is shown in figure 4.4. Strong magnetic correlations above the Néel temperature are expected for systems with magnetic frustration, and were already observed for CePdAl in NMR measurements [OMN+08]: The correlation length at 3 K was estimated to be $2.3 \cdot a = 16.5$ Å, which was measured in powder so that the reference to the a-axis is only an assumption. The single crystal neutron measurement yields 15.8 Å along h, 12.6 Å along k and 21.4 Å along l at 3 K, in very good
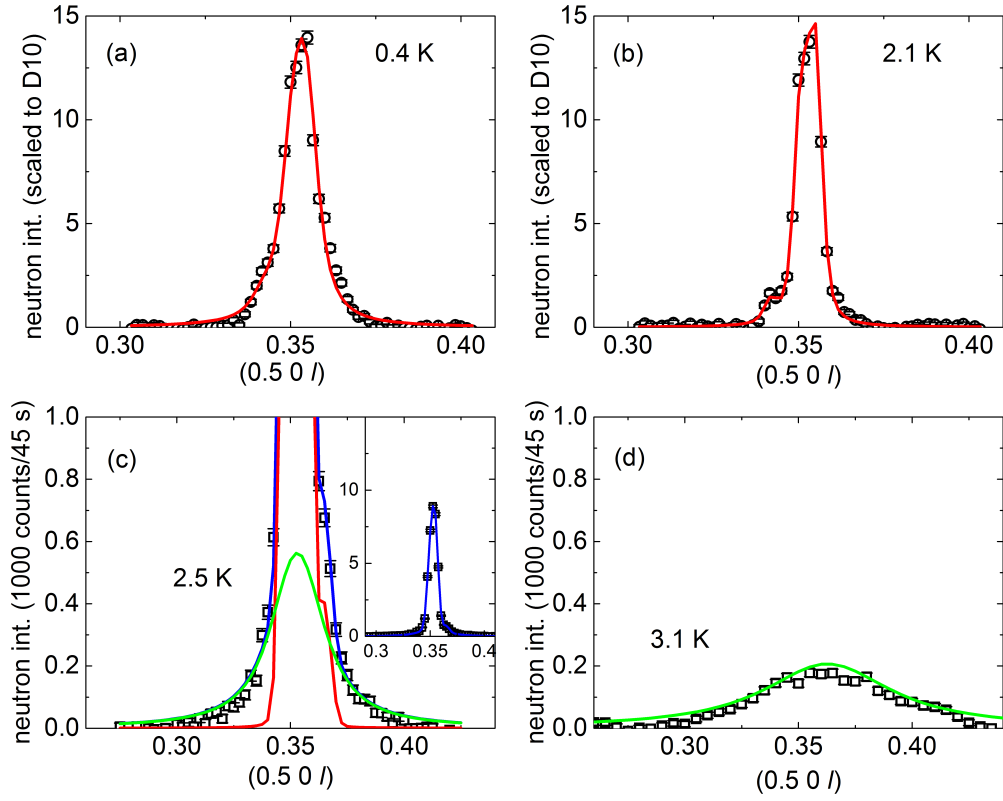
Figure 4.4: Scans along l around $(0.5\ 0\ \tau_l)$, $\tau_l \approx 0.35$, measured at RESI (images (a) and (b)) and D10 (images (c) and (d)). The data measured at RESI have been multiplied with a constant factor to bring them to the same intensity scale as the D10 data. A background has been subtracted from all scans. The inset in panel (c) shows the same data as the main image on the axis scale of panel (a) and (b). Plotted in red are fit functions for the long-range order, in green fit functions for short-range order, and their sum for the scan at 2.5 K is plotted in blue (see main text for details).
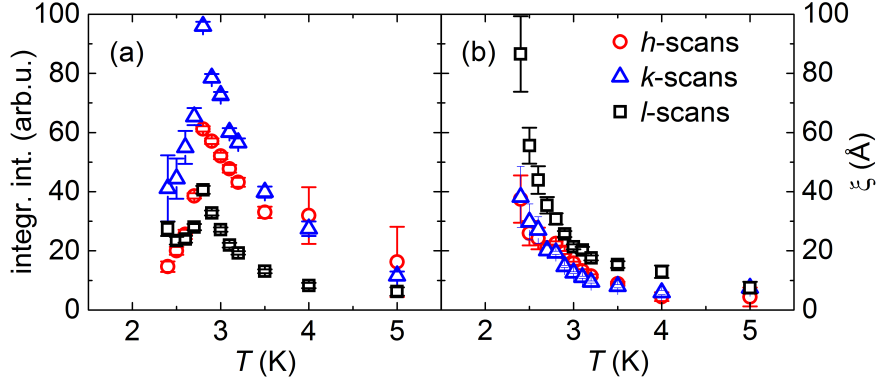
Figure 4.5: (a) Fitted integrated intensity and (b) correlation length ξ of the short-range order in CePdAl, for scans measured along h (red), k (blue) and l (black) at D10. The integrated intensity along k is increased mainly due to the poorer resolution outside of the scattering plane.

overall agreement with the NMR data.

On lowering the temperature below $T_N = 2.7$ K, a sharp signal, corresponding to long-range order, appears; the temperature dependence of its intensity has been discussed above (figure 4.3). For a certain temperature range, short-range correlations coexist with the long-range signal, so that the measured data need to be described by two Voigt functions. In figure 4.4, this is shown for a scan at 2.5 K. The origin of the broad signal are critical fluctuations associated with the phase transition. The fitted intensity and correlation length are shown in figure 4.5, for scans from below and above T_N. The fit accuracy is problematic below T_N due to the large interdependence of the width of both peaks, as well as a competition between the short-range order signal and the background level[1]. The intensity of the broad signal reaches a maximum at T_N, as expected for critical fluctuations. The correlation length does not diverge at T_N, but instead becomes increasingly longer as the temperature is lowered. This might be an effect of limited fit accuracy. Interestingly, the correlation length of the short-range order is not strongly anisotropic: Fitted values are nearly identical for the h and k direction and are only around 50% larger for the l-scans. Below 2.4 K the two signals can no longer be reasonably separated.

At $T \approx$ 2-2.2 K, the magnetic Bragg peak of CePdAl can be described with a single sharp peak, whose intrinsic width is smaller (along l) or of

---

[1]The background was fixed for scans at all temperatures, but its absolute value is not exactly known, since fluctuations persist to high temperatures.
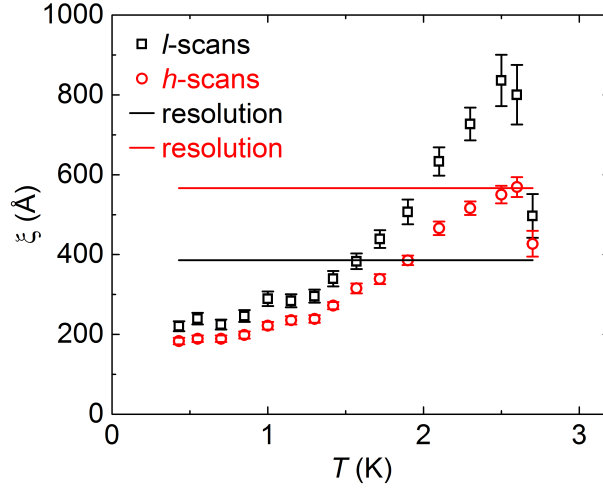
Figure 4.6: Fitted correlation length ξ of the long-range order signal in CeP-dAl, for scans measured along h (red) and l (black) at RESI. The lines show the correlation length which corresponds to an equality of the fitted Lorentzian width with the Gaussian resolution width.

the same order (along h) as the resolution width. However, an interesting and unusual observation is made as the temperature is lowered further: The width of the magnetic signal clearly becomes larger. In figure 4.4, this can be seen when comparing the scan at 2.1 K with the scan at 0.4 K. As it is apparent from figure 4.3, this is not accompanied by a loss in magnetic intensity. The temperature development of the correlation length ξ, which is extracted from fits to l- and h-scans, is shown in figure 4.6. The RESI dataset is used here, since it has a very good Q resolution. ξ gradually becomes smaller on lowering the temperature, both in the l-direction and in the h-direction. At the lowest measured temperature, the fitted correlation length is around 200 Å, i.e. the ordered magnetic regions are still rather large. The shrinking of the correlation length is contrary to what is expected for a conventional antiferromagnet, so that a relationship to the magnetic frustration seems likely. A possible explanation are correlations that involve the one third of the spins which (supposedly) do not participate in the long-range order, which interfere with the order of the other two thirds of the spins.

Summing up the results on the pure CePdAl sample, magnetic Bragg peaks are observed which indicate a partially ordered state, in agreement with earlier powder data [DEM$^+$96, KDKvdB02]. Strong short-range correlations are observed above the Néel temperature, which is a sign of frustration.

They persist for a limited temperature range below T_{N} in co-existence with the long-range order. The long-range order itself has a finite correlation length or domain size at the lowest temperatures. This might be a sign that correlations occur between the frustrated moments, and would be in agreement with the observation of a broad, weak signal at the position of nominally forbidden reflections.

4.3 Magnetic order in CePd$_{0.9}$Ni$_{0.1}$Al

Details of the diffraction experiment

The experiment was performed at the diffractometer E4 (BER II, Helmholtz-Zentrum Berlin) with an incident neutron wavelength of $\lambda = 2.45$ Å. The sample was a 7.0 g single crystal of composition CePd$_{0.9}$Ni$_{0.1}$Al which was synthesised by Veronika Fritsch by Czochralski growth (batch number VF563). Nuclear Bragg peaks are rather broad (1.2°) due to disorder induced by the Ni substitution.

The sample was glued to a copper sample holder on a polished surface perpendicular to the [110] direction to yield (h 0 l) as horizontal scattering plane, in analogy to the experiments performed on CePdAl. Cooling was achieved with a ^{3}He cryostat (base temperature 0.25 K). The detector was a 20x20 cm^2 area detector; intensities were obtained by integrating over the central section of the detector. Tilting of the sample or the detector out of the scattering plane was not possible. All measurements were normalised to a monitor that was placed in the beam in front of the sample.

Results

The experiment was performed analogous to the measurements on CePdAl. Scans were measured at temperatures between 0.25 K and 5 K along l and h (scans along k are not allowed by the geometry of the set-up). A first important observation is that the magnetic ordering vector in CePd$_{0.9}$Ni$_{0.1}$Al is the same as for the pure compound, $\tau = (0.5\ 0\ \tau_l)$, $\tau_l \approx 0.35$. An exemplary scan at $(1.5\ 0\ \tau_l)$ is shown in figure 4.7. The incommensurate component τ_l appears again to be temperature dependent, with the magnitude decreasing with decreasing temperature. However, the error bars of the fitted position are of a similar size as the absolute change in position, so that a more detailed discussion, e.g. of the lock-in temperature, is not possible. This is not due to a smaller variation of τ_l compared to pure CePdAl, but due to a strong increase of the size of the error bars, caused by the increased width of the magnetic Bragg peaks.
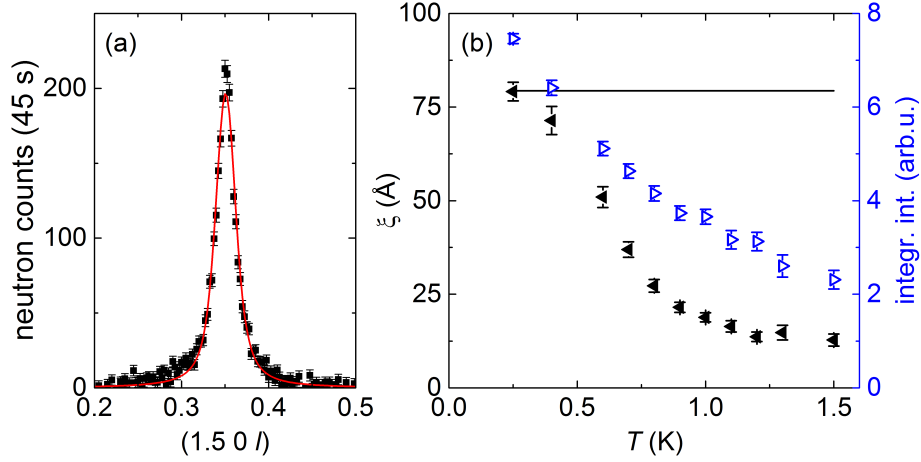
Figure 4.7: Magnetic Bragg peak of $CePd_{0.9}Ni_{0.1}Al$, measured at E4. (a) l-scan at $(1.5\ 0\ \tau_l)$ with Lorentzian fit. (b) Fitted correlation length (black) and integrated intensity (blue) of l-scans at different temperatures. The black line shows the correlation length which corresponds to an equality of the fitted Lorentzian width with the Gaussian resolution width.

The h- and l-scans were again fitted with Voigt functions, where the Gaussian component describes the resolution. It should be noted that its width is mainly given by the mosaicity of the sample, rather than the instrument resolution, due to the inhomogeneity of the single crystal. Still, the magnetic Bragg peaks are broader than the nuclear Bragg peaks at all measured temperatures. The fitted intensity and correlation length ξ of the magnetic signal are shown in figure 4.7 for scans along l. Results for scans along h are nor shown, since they show a similar trend. Both correlation length and intensity become gradually larger as the temperature is lowered, but they display no sharp signature at the ordering temperature $T_N = 0.8$ K [Luc14], and do not seem to reach a saturation value at the lowest measured temperature of 0.25 K. The absolute correlation length is rather short (below 100 Å). This broadening cannot be associated with the same mechanisms as discussed for CePdAl: Neither does it correspond to the short-range order observed around the ordering temperature—the signal of $CePd_{0.9}Ni_{0.1}Al$ is too broad to observe that—nor is it reminiscent of the signal broadening of CePdAl at low temperatures. It is therefore likely that the broadening observed in $CePd_{0.9}Ni_{0.1}Al$ is caused by disorder. This is supported by the comparison of the data shown here with neutron scattering data of a CePdAl crystal under a pressure of 0.65 GPa, published in reference [PMA+07]: This

has a comparable ordering temperature, but a very sharp transition into the ordered state.

4.4 Ordered magnetic moment in the series CePd$_{1-x}$Ni$_x$Al

Details of the diffraction experiment

The aim of this experiment was the comparison of the ordered magnetic moment of CePdAl, CePd$_{0.95}$Ni$_{0.05}$Al and CePd$_{0.9}$Ni$_{0.1}$Al. For this purpose, all samples were measured at the same instrument (E4, Berlin) under identical settings and with the same sample environment (^{3}He cryostat). The CePdAl and the CePd$_{0.9}$Ni$_{0.1}$Al crystal were the same as in the experiments described in section 4.2 and 4.3, respectively. The CePd$_{0.95}$Ni$_{0.05}$Al sample was a 3 g single crystal synthesised by Veronika Fritsch (sample number VF573). The diffraction experiment revealed that the 5% Ni substituted sample contains two major grains of similar size, which are missaligned by around 13°. All results presented here thus refer only to one of the two grains, which was chosen for the sample orientation. Even within this grain, nuclear reflections are rather broad ($\approx 1.8°$), showing that the crystalline quality of this sample is poorer than that of both other crystals.

The settings at the diffractometer E4 were very similar to the experiment of the last section. However, the data analysis was done in a modified way by making explicit use of the area detector: Intensity maps in the (h 0 l) plane were constructed, from which cuts along h or l could be derived. This analysis was done by Stefan Lucas, who mainly conducted the experiment.

Results

The analysis of the magnetic Bragg peaks of CePdAl and CePd$_{0.9}$Ni$_{0.1}$Al are in line with the results presented in the last two sections. Only a few temperatures were measured in the current experiment, but the trends for intensity, peak position τ_l and correlation length ξ are the same as already reported. For CePd$_{0.95}$Ni$_{0.05}$Al, measurements were performed at 20 different temperatures. Magnetic Bragg peaks appear at the same positions as for the other two samples. The temperature development of the magnetic intensity shows the expected behaviour, similar to pure CePdAl, and confirms the Néel temperature $T_N = 1.8$ K found in thermodynamic measurements [Luc14]. Since the resolution of the experiment is rather poor, due to the crystalline quality, no statements can be made about the lock-in transition or about possible short-range order effects.

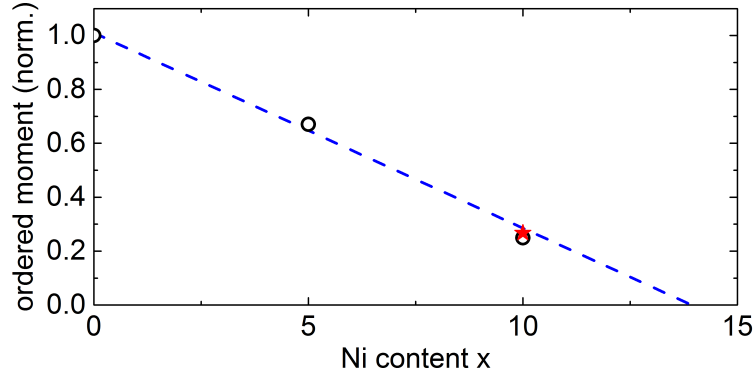For the three samples, fits were done to the magnetic reflections (0.5 0 0.35),

Figure 4.8: Ordered magnetic moment for CePdAl, $CePd_{0.95}Ni_{0.05}Al$ and $CePd_{0.9}Ni_{0.1}Al$, normalised to the moment of CePdAl. Plotted in black are data points measured at 0.25 K, while the red star shows the extrapolated value at $T = 0$ for the sample with 10% Ni content. The linear trend is demonstrated by the blue dashed line.

(0.5 0 0.65), (1.5 0 0.35) and (1.5 0 0.65) at 0.25 K, and their integrated intensity was averaged for each sample. This magnetic intensity was then normalised to the averaged integrated intensity of the nuclear reflections (1 0 0), (1 0 1) and (0 0 1). In figure 4.8, the ordered moment is shown, which is proportional to the square root of the neutron intensity. Here the ordered moment of the pure sample is set to 1 because the data do not yield absolute units. In powder neutron diffraction, the ordered moment of CePdAl was found to be 1.58 μ_B (reference [DEM+96]) or 1.77 μ_B (reference [KDKvdB02]). It should be noted again that this moment refers to two out of three cerium positions, and the ordered moment on the third cerium position is supposed to be zero.

While CePdAl and $CePd_{0.95}Ni_{0.05}Al$ have reached their saturation moment at 0.25 K, it can be assumed that the intensity of the magnetic Bragg peaks of $CePd_{0.9}Ni_{0.1}Al$ would rise further for $T \to 0$ (compare figure 4.7). The estimated additional increase is 15%. The resulting ordered moment is shown as a red star in figure 4.8. Then it can be concluded that the suppression of the ordered moment with Ni substitution is linear. This is demonstrated by the blue line, which ends at the critical concentration $x = 0.14$. Since also the Néel temperature is linearly reduced with Ni content, this implies a proportionality of the ordered moment and the ordering temperature.

In summary, the magnetic ordering vector in $CePd_{1-x}Ni_xAl$ samples is the same for all Ni concentrations, and the ordered moment is linearly suppressed with Ni content and Néel temperature. No conclusions can be drawn to the

development of possible frustration effects in the substituted samples, as observed for the pure compound; the crystalline quality of samples with Ni substitutions results in large peak widths, which make it difficult to study the intrinsic width of the magnetic reflections in detail.

Chapter 5

Magnetic excitations and fluctuations of $YbNi_4P_2$

5.1 The compound $YbNi_4P_2$

The study of magnetic quantum critical points in intermetallic systems has mostly been based on antiferromagnetic compounds. This is not only because ferromagnetic order is rarer in intermetallics, but also because it has proven to be difficult to suppress a second order transition into ferromagnetism to very low temperature. Instead, it was often observed that the transition turns first order when it is suppressed to low enough temperatures, or that the formation of other ordered phases prevents the observation of a ferromagnetic (FM) quantum critical point. This behaviour has been explained from a theoretical point of view by a coupling of the fluctuations of the FM order parameter to fermionic particle-hole excitations [KB03, GSS08, YS10, BBGK15]. Therefore, it has been an exciting discovery that $YbNi_4P_2$ has a second order transition into ferromagnetism as low as 170 mK, which can be suppressed to zero by arsenic doping on the phosphorus site [KLS+11]. The compound contains magnetic Yb^{3+} ions, while Ni is non-magnetic, and shows Kondo characteristics with $T_K \approx 8$ K. It is the first 4f-based intermetallic compound that allows ferromagnetic quantum criticality to be studied.

$YbNi_4P_2$ crystallises in the tetragonal $ZrFe_4Si_2$ structure which has several remarkable features [KCB00]: The lattice parameter $c = 3.59$ Å is only about half as large as the lattice parameter $a = 7.06$ Å, so that quasi-1D chains of Yb ions are formed along the c-axis (see figure 5.1). Neighbouring chains are shifted by $c/2$, and the Yb ions in one chain experience a crystal electric field (CEF) that is rotated by 90° with respect to the next chain. This structure leads to a strong anisotropy of the magnetic properties, as studies on $YbNi_4P_2$ single crystals have shown [KG12, SKL+13]. At high
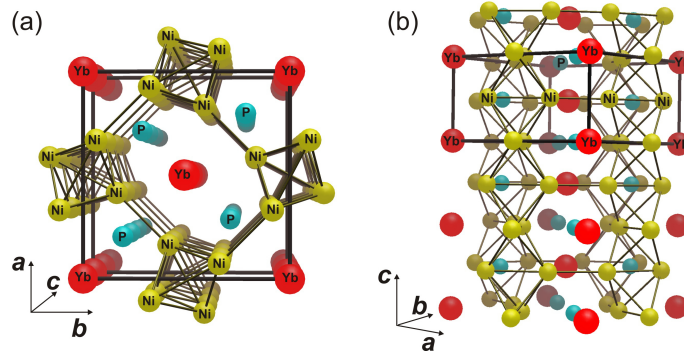
Figure 5.1: Crystal structure of YbNi$_4$P$_2$, looking along the c-axis (panel a) and with the c-axis upright (panel b); pictures by Cornelius Krellner, taken from reference [KG12]. Note that the site symmetry of the Yb sites is orthogonal, while the crystal structure is tetragonal.

temperatures, the CEF causes the c-axis to be the easy axis of the magnetisation, but below T_C, the ordered moment is oriented perpendicular to the c-axis. A suggested explanation of this unusual behaviour is the enhanced role of transverse spin fluctuations close to a QCP: The driving force for the hard-axis order is the maximisation of phase space for the transverse fluctuations, which was nicknamed the "quantum Indian rope trick" by the authors [KPG14].

At the time of the experiments, no large single crystals were available to study this interesting magnetic anisotropy on a microscopic level by neutron scattering. Still, neutron experiments can make important contributions to understanding the properties of YbNi$_4$P$_2$. In the first part of this chapter, an analysis of the crystal-electric-field excitations in YbNi$_4$P$_2$ is presented. This analysis combines data from powder neutron spectroscopy and heat capacity with susceptibility measurements: The former reveal the level scheme, while the latter contain information about the anisotropy. To handle the complexity that results from the orthorhombic site symmetry of Yb in YbNi$_4$P$_2$, the programme package McPhase was used to fit the experimental data [RLK$^+$13].

In the second part, high-resolution neutron spectra of YbNi$_4$P$_2$ are presented, which show the quasi-elastic magnetic fluctuations. Again, the data cannot reveal any directional dependence since they were measured on powder. Nevertheless, the ferromagnetic nature of the fluctuations can be demonstrated by comparing the local response (at all momentum transfers) to the $Q = 0$ response.

5.2 Crystal electric field scheme

The Yb^{3+} ion has the electron configuration $[Xe]4f^{13}$ and a total angular momentum of $J = 7/2$ in the ground state according to Hund's rules. For J to be a good quantum number, the spin-orbit coupling needs to be much stronger than the effect of the CEF, which is generally true for 4f-compounds [Blu01, JM91]. The measured effective moment at high temperatures suggests that this is also the case for $YbNi_4P_2$: It is found to be 4.52 μ_B in a linear fit to $1/\chi$ between 50 K and 400 K [KLS+11], very close to the theoretical value of 4.53 μ_B for an Yb^{3+} ion [Blu01]. The eight-fold multiplet of the $J = 7/2$ state is expected to split into four Kramer's doublets due to the orthorhombic crystalline environment around the ytterbium ions. All Yb ions are located on equivalent crystallographic positions, even if the main in-plane axis is rotated by 90° between the corner and the body-centred sites. Therefore, one expects the same CEF scheme for all Yb ions. The inelastic neutron scattering data shown in this section have been published in [HSK+13].

5.2.1 Inelastic neutron scattering

Experimental details

For the neutron measurements of the CEF excitations, several polycrystalline samples have been united to yield a total mass of 5.39 g. These included parts of the batches 63522, 63523, 63524 and 63529, which were all synthesised by Cornelius Krellner. Due to the self-flux growth, polycrystalline $YbNi_4P_2$ samples contain grains of Ni, Ni_3P and other Ni-P binary compounds. The contamination can be reduced by scanning a permanent magnet over the carefully ground samples, which will attract the ferromagnetic nickel grains. Since the samples are prepared in glassy-carbon crucibles, graphite appears as a further contaminant. This is evident from the neutron diffractogram which shows graphite Bragg peaks.

To quantify the amount of contamination, atom absorption spectroscopy has been performed on a fraction of the neutron sample. This analysis has not been performed on this particular sample, but for a later sample used for the measurement of the quasi-elastic scattering (see section 5.3). This later sample included the 5.4 g used in the CEF measurements and around 10 g of additional polycrystalline material. Its composition was found to be $Yb_1Ni_{4.47}P_{2.20}C_{0.57}$. The content of elemental nickel was separately determined by magnetisation measurements to be about 3 mol%. Apparently, the sample contains a rather large amount of Ni-P binary compounds. Also the carbon content is surprisingly high; however, from the intensity of the

graphite (002) Bragg peak, it can be deduced that the carbon content in the 5.4 g sample was around 2.5 times smaller than that of the analysed sample.

Despite these contaminants, the low-temperature, low-energy magnetic neutron scattering can be considered to originate only from YbNi$_4$P$_2$. Since Ni$_3$P is a Pauli paramagnet [ZJ93], Ni is a ferromagnet that orders well above room temperature and graphite is diamagnetic, none of these compounds are expected to show a temperature-dependent magnetic signal in the relevant temperature range well below room temperature.

The measurement of the CEF excitations was performed at the thermal-neutron time-of-flight spectrometer IN4 at ILL, Grenoble. The incident neutron energy was $E_i = 36$ meV ($\lambda_i = 1.5$ Å), which led to a measurable range of wavevector transfer of about $Q = 1.0 - 7.3$ Å^{-1} at the elastic line. A few measurements were also taken with $E_i = 68$ meV ($\lambda_i = 1.1$ Å). A 3x4 cm rectangular sample holder made from aluminium was used; it was also measured separately without sample so that its signal could be subtracted from all data. The self-absorption of the sample was accounted for with a Paalman-Pings correction [PP62], and the efficiency of each ^{3}He detector was determined by measuring a vanadium reference. All scans were normalised to a monitor that was placed in the beam in front of the sample. An orange cryostat allowed a base temperature of 1.6 K to be achieved.

For the subtraction of the phonon contribution, the non-magnetic reference LuCo$_4$Ge$_2$ was also measured, which has the same crystal structure as YbNi$_4$P$_2$[1]. Polycrystals from batches 42541 and 42542 (also produced by Cornelius Krellner) were ground to yield a total powder mass of 7.61 g. The same sample holder and measuring conditions were used.

Results

Figure 5.2 shows the measured scattering intensity of YbNi$_4$P$_2$ as a function of energy and wavevector transfer at 1.6 K. Two main features can be distinguished in the inelastic regime: Intensity maxima due to magnetic excitations can be found at $E \approx 5 - 15$ meV, while intensity maxima due to phonon excitations are at $E \approx 12 - 22$ meV. The distinction can be made on the basis of the Q dependence: The intensity of the magnetic excitations follows the magnetic form factor and therefore decreases with increasing momentum transfer, while the phonons show a $I \propto Q^2$ relationship.

For a quantitative analysis of the magnetic signal a subtraction of the phonon contribution was done according to the procedure of Murani [Mur83] with the non-magnetic reference compound LuCo$_4$Ge$_2$. In Murani's method,

---

[1]At the time of the experiment, the reference compound LuNi$_4$P$_2$ was not yet available.
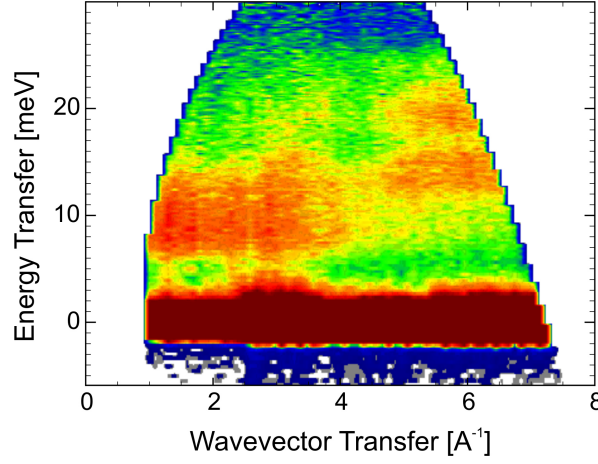
Figure 5.2: Colour plot of the measured neutron scattering intensity of $YbNi_4P_2$ at 1.6 K as function of energy and wavevector transfer. Blue indicates low intensity and red high intensity; the intensity in the elastic line is above the cut-off limit. Published in reference [HSK+13].

spectra at high momentum transfer (where only phonons have significant intensity) are subtracted from the low momentum transfer spectra (where magnetic excitations are dominant). The high-Q-spectra need to be scaled with the phonon intensity ratio Int(low-Q)/Int(high-Q) which is determined through the non-magnetic reference. This procedure should be reliable despite the large differences in the atomic masses between $YbNi_4P_2$ and $LuCo_4Ge_2$ since their spectra are not directly subtracted. Murani's method also requires that there is no pronounced Q dependence of the phonons, other than the proportionality to Q^2; this is the case for incoherent phonons or for sufficient averaging over the Brillouin zone. This condition is reasonably met for the $YbNi_4P_2$ powder spectra.

For the evaluation of the CEF levels, all spectra with $Q = 2.5 \pm 0.5$ Å^{-1} are summed up. This choice allows both a good ratio of magnetic to phonon intensity and a large range of energy transfers. Subtraction of phonon intensity, as outlined above, then yields the magnetic intensity. The subtraction is not meaningful at small energy transfers below about 4 meV due to the varying intensity along the elastic line. Figure 5.3 shows the data at the lowest measured temperature. It is now apparent that the broad feature at $E \approx 5 - 15$ meV is composed of at least two overlapping peaks. These can be identified as two or three CEF transitions. Other magnetic excitations, such as magnons, are not expected in this energy and temperature range, since the ordering temperature is only 170 mK. A two-peak fit yields tran-
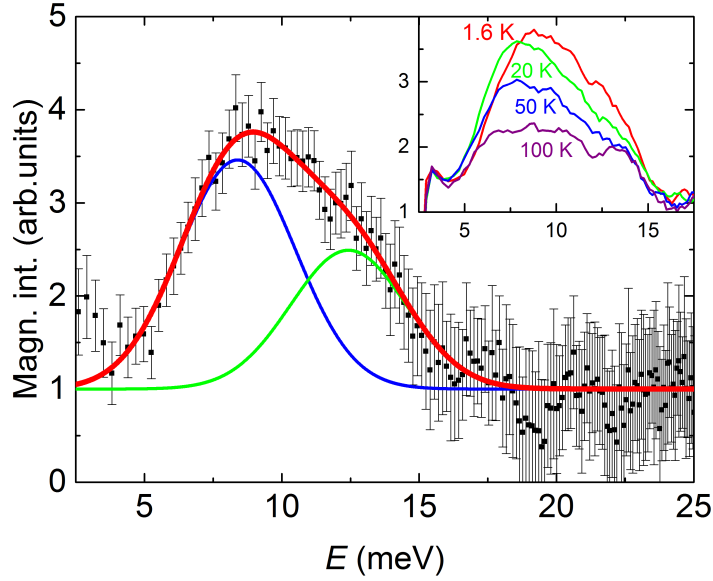
Figure 5.3: Magnetic intensity of YbNi$_4$P$_2$ at $Q = 2.5 \pm 0.5$ Å^{-1} and $T = 1.6$ K. A two-peak fit is also shown. In the inset, the same data are plotted together with spectra taken at higher temperatures. Published in reference [HSK+13].

sition energies of 8.5 ± 0.5 meV and 12.5 ± 0.5 meV and an energy width (FWHM) of 5.0 meV at 1.6 K. The width exceeds the energy resolution of the spectrometer by far, which might be a result of Kondo broadening. Alternatively, or rather additionally, the peak broadening could be caused by a dispersion of the CEF levels along certain crystallographic directions since only the polycrystalline average is measured.

In the inset of figure 5.3, the temperature development of the CEF feature is shown. The overall intensity decreases with temperature, as expected for transitions from the ground state due to its thermal depopulation. Furthermore, there seems to be a slight shift to lower energies when the temperature is increased from 1.6 K to 20 K. Since the CEF level scheme should be temperature independent, such an apparent shift might indicate a further transition at slightly lower energies, which does not originate from the ground state and becomes measurable when higher CEF levels start to be thermally populated.

It was also confirmed in a measurement with an incident neutron wavelength of $\lambda = 1.1$ Å that no further transitions can be observed up to 60 meV. Krellner and Geibel [KG12] suggest that the highest CEF level is below

40 meV. Therefore, it seems unlikely that a transition occurs at $E > 60$ meV. Later measurements on $YbNi_4P_2$ with better energy resolution (see section 5.3) also showed that there is no transition from the ground state at $E < 3$ meV. Thus, there must either be three excited levels in the range from 7 to 13 meV, or one transition has a vanishing transition matrix element for neutron scattering.

Comparison to heat capacity measurements

Transitions to excited CEF levels give a Schottky-contribution to the heat capacity. For a 4-level scheme with equal degeneracy of all levels, the contribution is given by:

$$C_{\text{Schottky}} = \frac{R}{(k_B T)^2} [\Delta_1^2 e^{-\frac{\Delta_1}{k_B T}} + \Delta_2^2 e^{-\frac{\Delta_2}{k_B T}} + \Delta_3^2 e^{-\frac{\Delta_3}{k_B T}}$$
$$+ (\Delta_2 - \Delta_1)^2 e^{-\frac{\Delta_1 + \Delta_2}{k_B T}} + (\Delta_3 - \Delta_1)^2 e^{-\frac{\Delta_1 + \Delta_3}{k_B T}} + (\Delta_3 - \Delta_2)^2 e^{-\frac{\Delta_2 + \Delta_3}{k_B T}}]$$
$$[(1 + e^{-\frac{\Delta_1}{k_B T}} + e^{-\frac{\Delta_2}{k_B T}} + e^{-\frac{\Delta_3}{k_B T}})^2]^{-1}$$

$$(5.1)$$

To account for the low-temperature heat capacity properly, the Kondo effect needs to be included in the model. The contribution to the heat capacity of the ground-state doublet has been calculated and tabulated by Desgranges and Schotte [DS82], as a function of T/T_K. This contribution can simply be added to the Schottky term 5.1. However, this only considers the Kondo broadening of the ground state, while Kondo broadening of all levels is expected to occur. Romero *et al.* have given an empirical approach which improves the description by including the broadening of the first excited level as well [RASN14]. For the heat capacity of two doublets with half width Γ_0 and Γ_1 their approach gives:

$$C_{2d} = -\frac{R}{2(\pi k_B T)^2} \mathbf{Re} \sum_{j=0}^{1} \left\{ (\Gamma_j + i\Delta_j)^2 \right.$$
$$\left[4\psi' \left(1 + \frac{\Gamma_j + i\Delta_j}{\pi k_B T} \right) - \psi' \left(1 + \frac{\Gamma_j + i\Delta_j}{2\pi k_B T} \right) \right] \right\} \qquad (5.2)$$
$$+ \frac{R}{k_B} \frac{\Gamma_0 + \Gamma_1}{\pi T}$$

Here ψ' is the derivative of the digamma function. The Kondo temperature implicitly enters in this expression, since it is proportional to Γ_0. The second and third excited level are included by adding the Schottky expression
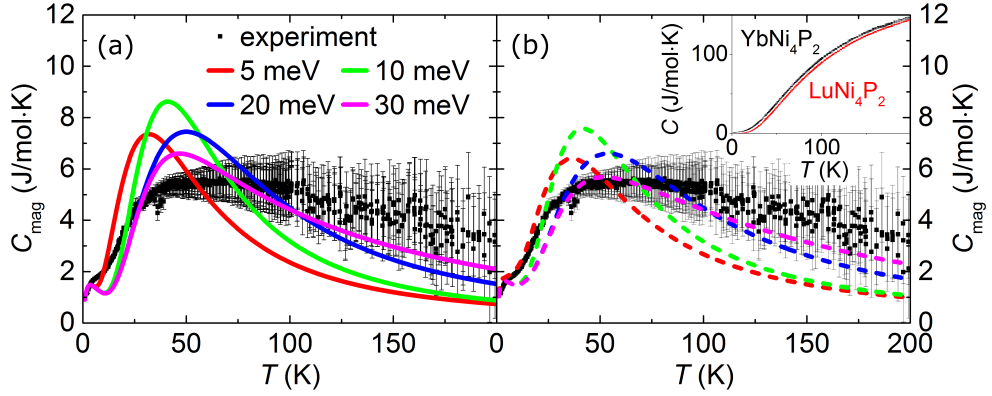
Figure 5.4: Magnetic heat capacity of YbNi$_4$P$_2$. The measured data (black squares) are gained from a subtraction of the heat capacity of LuNi$_4$P$_2$ from the total heat capacity of YbNi$_4$P$_2$ (original data shown in the inset, measured by Kristin Kliemt). (a) Lines show the calculated heat capacity according to the Schottky model (plus Kondo contribution from [DS82]), with transition energies 8.5 meV, 12.5 meV and a third level as indicated in the plot. (b) The same plot is shown, but this time the heat capacity is calculated according to the formula of Romero *et al.* [RASN14].

5.1. The total heat capacity for CEF transitions in the presence of Kondo broadening is thus given by

$$C_{\text{CEF}} = C_{\text{2d}} + C_{\text{Schottky}} - \frac{R}{(k_B T)^2} \left[\frac{\Delta_1^2 e^{-\frac{\Delta_1}{k_B T}}}{(1 + e^{-\frac{\Delta_1}{k_B T}})^2} \right], \qquad (5.3)$$

where the last term avoids double counting of the transition between the ground state and the first excited level.

To compare experimental data to either of these models, it is necessary to extract the magnetic contribution to the heat capacity from the total heat capacity. For this purpose, the non-magnetic reference compound LuNi$_4$P$_2$ was recently synthesised by Kristin Kliemt (Goethe University Frankfurt am Main). It has the same crystal structure as YbNi$_4$P$_2$ and there is only a minor difference in the atomic masses, so that the phonon contribution to the specific heat is expected to be very similar for both compounds. Therefore, the difference of the measured heat capacity of YbNi$_4$P$_2$ to that of LuNi$_4$P$_2$ yields to a good approximation the magnetic heat capacity of YbNi$_4$P$_2$.

The data, measured by Kristin Kliemt, are shown in figure 5.4, together with several calculated curves: On the left side, the heat capacity has been

calculated from equation 5.1 (plus Kondo contribution, taken from [DS82]), while on the right side equation 5.3 was used. All calculations include energy levels at 8.5 meV and 12.5 meV, while the third is set to different values. The values for Γ_0 and Γ_1 in equation 5.3 are taken from the neutron scattering data (Γ_0, the width of the quasi-elastic signal, is discussed in section 5.3; $2\Gamma_1$, the width of the CEF excitations, is 5 meV, as stated above). None of the two approaches fit the experimental data very well; the approach of Romero *et al.* yields a slightly better agreement with the experiment, as the maximum value of C_{mag} is too large in the Schottky model. Both models suggest that the third level is at higher energy than the two observed with neutron scattering. Unfortunately, an exact determination of this level is not possible, since the heat capacity data are not very accurate at temperatures higher than 100 K. In this temperature range, the magnitude of the phonon contribution is at least a factor 10 larger than that of the magnetic signal.

The combination of neutron and heat capacity data suggests a level scheme $E_1 = 8.5$ meV, $E_2 = 12.5$ meV and $E_3 \approx 25$ meV, where the transition from the ground state to the latter has a small or vanishing neutron scattering cross section.

5.2.2 Simulations

Model Hamiltonian and fitting procedure

To gain better insights into the crystal electric field of $YbNi_4P_2$, susceptibility data measured on single crystals were fitted in combination with the results for the energy scheme presented above. For this purpose, the programme "so1ion" of the McPhase package (version 5.1) was used. It is based on the assumption that the CEF is weak compared to spin-orbit coupling and thus acts as a perturbation to the $J = 7/2$ state, as it is generally the case for 4f-compounds [Blu01, JM91]. The CEF is parametrised by the Stevens operator formalism [Hut64, JM91, RLK$^+$13], so that the Hamiltonian of the Yb^{3+} ion can be written as

$$H_{\mathrm{single\,ion}} = \sum_{lm} B_l^m O_l^m(\mathbf{J}) - g_{\mathrm{J}}\mu_{\mathrm{B}}\mathbf{J}\mathbf{B} \tag{5.4}$$

with the crystal field parameters B_l^m and the Stevens operators $O_l^m(\mathbf{J})$; the last term accounts for the Zeeman effect in a magnetic field $\mathbf{B}$. Equation 5.4 ignores exchange interaction and hyperfine coupling, which is justified at sufficiently high temperatures if their energy scales are small compared to the CEF. Both the ordering temperature of 170 mK and characteristic temperatures for hyperfine interactions are around three orders of magnitude smaller

$O_2^0 = 3J_z^2 - X$
$O_2^2 = \frac{1}{2}[J_+^2 + J_-^2] = J_x^2 - J_y^2$
$O_4^0 = 35J_z^4 - (30X - 25)J_z^2 + 3X^2 - 6X$
$O_4^2 = \frac{1}{4}[(J_+^2 + J_-^2)(7J_z^2 - X - 5) + (7J_z^2 - X - 5)(J_+^2 + J_-^2)]$
$O_4^4 = \frac{1}{2}[J_+^4 + J_-^4]$
$O_6^0 = 231J_z^6 - (315X - 735)J_z^4 + (105X^2 - 525X + 294)J_z^2$ $\qquad -5X^3 + 40X^2 - 60X$
$O_6^2 = \frac{1}{4}[(J_+^2 + J_-^2)(33J_z^4 - \{18X + 123\}J_z^2 + X^2 + 10X + 102)$ $\qquad + (33J_z^4 - \{18X + 123\}J_z^2 + X^2 + 10X + 102)(J_+^2 + J_-^2)]$
$O_6^4 = \frac{1}{4}[(J_+^4 + J_-^4)(11J_z^2 - X - 38) + (11J_z^2 - X - 38)(J_+^4 + J_-^4)]$
$O_6^6 = \frac{1}{2}[J_+^6 + J_-^6]$

Table 5.1: Stevens operators relevant for the CEF acting on the Yb^{3+} ion in YbNi$_4$P$_2$; $X = J(J-1)$ [Hut64].

than the CEF, so that this assumption should hold for all temperatures considered in the fits (the lowest temperature was chosen to be 14 K).

The Stevens operators can be expressed in terms of components of the total angular momentum **J** and **J**$_\alpha$ with α = x,y,z (commonly, **J**$_\mathbf{x}$ and **J**$_\mathbf{y}$ are replaced by the raising and lowering operators **J**$_+$ and **J**$_-$). Generally, only even terms appear due to the orthogonality of the spherical harmonics, and for f-electrons, terms with $l > 6$ vanish. m can generally take values from $-l$ to $+l$, but the appropriate choice of axis will ensure that only parameters with either the positive or the negative values of m appear. In case of YbNi$_4$P$_2$, setting z parallel to the c-axis, but x and y at an angle of 45° with respect to the a-axis ensures $B_l^m = 0$ for $m < 0$. No further symmetry restrictions apply in the case of orthorhombic site symmetry. Thus, for the Yb ion in YbNi$_4$P$_2$, nine Stevens operators need to be considered: O_2^0, O_2^2, O_4^0, O_4^2, O_4^4, O_6^0, O_6^2, O_6^4 and O_6^6. Their expressions are given in table 5.2.2.

This set of 9 parameters defines the CEF Hamiltonian 5.4 of the Yb^{3+} ion in YbNi$_4$P$_2$. McPhase will determine its eigenfunctions as linear combinations of the m_J states (with $m_J = \pm 7/2, \pm 5/2, \pm 3/2, \pm 1/2$) as well as the energy eigenvalues by diagonalisation of the Hamiltonian. Observable quantities such as the susceptibility or the neutron scattering cross section can be cal-

culated in the next step and compared to experimental data. To perform a fit, the difference between calculated and experimental values needs to be quantified by a standard deviation s [RLK$^+$13]:

$$s^2 = 1/N \sum_i \delta_i / \mathrm{err}_i \qquad (5.5)$$

δ_i is the difference between an experimental data point and the respective calculated quantity, err_i is the error of the data point and N the total number of points considered. In the CEF analysis, the following quantities have been used for δ_i:

- The deviation of the calculated to the measured inverse susceptibility for 20 linearly spaced data points between 40 K and 400 K. This was done both for the *c*-direction and for the *ab*-plane, while the latter requires to average the calculated susceptibilities in the [110] and the [1$\bar{1}$0] direction. This is necessary because McPhase calculates all quantities based on a single Yb ion, which has orthorhombic site symmetry, while the crystal has tetragonal symmetry and any macroscopic measurement averages over the two Yb ions in the unit cell which are rotated by 90° with respect to each other.

- The deviation of the calculated to the measured susceptibility for 20 linearly spaced data points between 14 K and 180 K. For the *c*-direction, the same data set was used as for the fit of the inverse susceptibility, but for the *a*- and *b*-axis data from NMR measurements of Rajib Sakar *et al.* were used [SBKG]. Unlike macroscopic measurements, the local probe NMR allows the orthorhombic symmetry of the Yb site to be observed. However, the assignment of the two signals to the *a*- or the *b*-axis, or any other direction within the *ab*-plane, is arbitrary. The Knight shift has been converted to susceptibility units by comparing the average of the two in-plane signals to the AC-susceptibility data.

- The deviation of the energy eigenvalues of the first and second excited state to the values 8.5 meV and 12.5 meV, the excitations measured by neutron scattering. This implies that the third excited state is at higher energy than 12.5 meV, which is justified from the heat capacity measurements.

- The deviation of the neutron scattering cross section for the transition to the third excited state from zero.

The relative importance of the different contributions to the standard deviation can be influenced by using artificial errors err_i in 5.5.

The Hamiltonian 5.4 does not include the conduction electrons, so it cannot describe the Kondo effect. However, the Kondo effect influences the susceptibility of YbNi$_4$P$_2$ even at high temperatures, so that the measured data needed to be corrected before they could be compared to the single ion simulations. It has been shown that the Kondo effect leads to a deviation from Curie's law, which can be parametrised with an effective $\theta = 4.5\ T_K$, describing the intersection of a high-temperature linear fit to the $1/\chi$-data with the T-axis [GZ74]. This is very similar to the molecular-field approach taken for antiferromagnets and ferromagnets. (Due to the low ordering temperature, the *ferromagnetic* molecular field in YbNi$_4$P$_2$ is expected to be very small.) Fitting the $1/\chi$-data of YbNi$_4$P$_2$ leads to a θ of 26 K in polycrystalline average (for a linear fit in the temperature range 200 to 400 K), corresponding to a Kondo temperature of around 6 K, in good agreement with data from heat capacity measurements [KLS+11] and neutron scattering (see section 5.3). Therefore, the measured $1/\chi$-data were shifted by -10 mol/cm^3, so that a fit to the shifted data gives a θ of zero. This has been done prior to fitting with McPhase for all susceptibility data, including the NMR data, assuming an isotropic Kondo effect.

Results

The values of the symmetry-allowed B_l^m parameters have been fitted to susceptibility and neutron data of YbNi$_4$P$_2$ using a grid search, which is necessary since the nine parameters are inter-dependent. Within McPhase, the search is performed using the command "searchspace", which proceeds stepwise by making the grid progressively finer. Regions of parameter space that have a very poor agreement to experimental values can be excluded in later levels, thus allowing a fine grid in interesting parameter regions while keeping the simulation time at a feasible level.

The size of the parameter space needs to be defined by giving maximum and minimum values for all parameters. An idea of their order of magnitude, and possibly also their sign, can be obtained from microscopic models. The simplest of those is the point charge model, which calculates the CEF scheme assuming point charges at the nuclear positions determined from x-ray powder diffraction. For the values of the charges, Mulliken charges from DFT calculations by Helge Rosner were used [KLS+11][2]: -0.135 e (Ni), +0.015 e (P) and +0.51 e (Yb). The electric field of these charges on a central Yb ion was calculated for a large sphere of radius 16 Å which includes 1350 ions. A more sophisticated model of the CEF scheme, also based on DFT

---

[2]The publication includes the DFT calculations, but not the Mulliken charges themselves, which were obtained through private communication with Helge Rosner.

calculations, was performed by Pavel Novák and Jan Kuneš [NK]. Their method was originally developed for oxides [NKK13, NKM$^+$13]. The crystal field parameters for both models are given in the first two rows of table 5.2. The point charge model predicts the B_2^0 parameter to be dominant, while it is very small in the DFT-based parameter set, which is instead dominated by a large B_2^2 parameter. Neither of the two parameter sets can reproduce the experimental data: The point charge model strongly overestimates the anisotropy between the *c*-axis and the *ab*-plane, while the DFT-based parameter set leads to an easy plane system rather than an easy *c*-axis, the latter of which is observed by experiment. The neutron spectra can also not be reproduced. Nevertheless, both models result in transitions energies that are in rough agreement with experiment, so that it can be assumed that they predict the right order of magnitude for the B_l^m parameters.

The B_l^m parameters which were fitted to experiments with McPhase are given in the right column of table 5.2, along with calculated transition energies and neutron intensities. The fitted inverse susceptibility and susceptibility corresponding to this B_l^m parameter set is shown in figure 5.5. Satisfactory agreement can be achieved for reproducing the anisotropy of $1/\chi$ between *c*-axis and *ab*-plane and the in-plane anisotropy in the NMR data. The latter shows that for $T > 40$ K, the local susceptibility of one of the in-plane components is as large as that of the *c*-axis. Some notable deviations of the fitted curves occur for the in-plane average of $1/\chi$ at high temperatures and for the in-plane splitting of χ at low temperatures.

The corresponding level scheme is 8.1 meV - 12.1 meV - 29.5 meV, very close to the scheme deduced from neutron scattering and heat capacity. For the first two levels, this is necessarily the case, since the fit aimed to approach the values 8.5 meV and 12.5 meV, using an artificial error of 0.25 meV which is relatively similar to a realistic experimental error. The third level was free in the fit, apart from the restriction that it should be larger than the second. It is encouraging that its value is fitted rather close to what has been suggested by the heat capacity data. More information can be obtained by a comparison of simulated and measured transition intensities. This comparison is confined to intensity ratios, since the determination of absolute neutron intensities is problematic in case of strong absorption effects. To also include the quasi-elastic (QE) signal, data at $\lambda = 1.5$ Å need to be considered (see section 5.3). They yield a measured intensity ratio 1:0.89:0.62 (QE:ΔE_1:ΔE_2) which is in reasonable agreement with the simulated intensity ratio 0.76:1:0.53. The fit also satisfies the condition that no intensity can be detected for the third transition.

The wave functions and energy eigenvalues corresponding to the global

[meV]	PCM	Novák/Kuneš	fit	(confidence interval)
B_2^0	-9.2e-1	-6.0e-3	-3.0e-1	(-3.4e-1 ... -2.6e-1)
B_2^2	8.3e-2	-1.4	-0.99	(-1.08 ... -0.89)
B_4^0	7.3e-4	2.3e-3	1.06e-2	(0.98e-2 ... 1.13e-2)
B_4^2	-2.1e-3	3.1e-3	7.1e-3	(0.2e-2 ... 1.3e-2)
B_4^4	2.8e-3	1.1e-2	1.9e-2	(1.1e-2 ... 2.9e-2)
B_6^0	-1.0e-6	1.2e-6	1.5e-4	(0.9e-4 ... 2.1e-4)
B_6^2	-1.3e-5	2.9e-4	-1.8e-5	(-5.2e-4 ... 5.5e-4)
B_6^4	-1.5e-5	-3.4e-4	1.2e-3	(0 ... 2.3e-3)
B_6^6	-2.0e-6	1.7e-4	1.1e-3	(0 ... 2.1e-3)
	(QE 9.7 b)	(QE 9.4 b)	(QE 4.0 b)	
ΔE_1	15.6 (2.8 b)	8.9 (3.0 b)	8.1 (5.3 b)	
ΔE_2	27.0 (0 b)	17.4 (0.1 b)	12.1 (2.8 b)	
ΔE_3	33.3 (0 b)	28.5 (0 b)	29.5 (0.2 b)	

Table 5.2: Crystal field parameters and transition energies for YbNi$_4$P$_2$, in meV; calculated neutron intensities in barn (b) are added to the transition energies (QE = quasi-elastic). PCM = point charge model, based on DFT calculations of Helge Rosner [KLS$^+$11]; results by Pavel Novák and Jan Kuneš are also based on DFT calculations [NK], but use a more elaborate method to deduce the CEF [NKK13, NKM$^+$13]; fits to experimental data were obtained in a grid search using McPhase (details see text). In parenthesis, the interval is given where the goodness of fit changes by less than 10%.
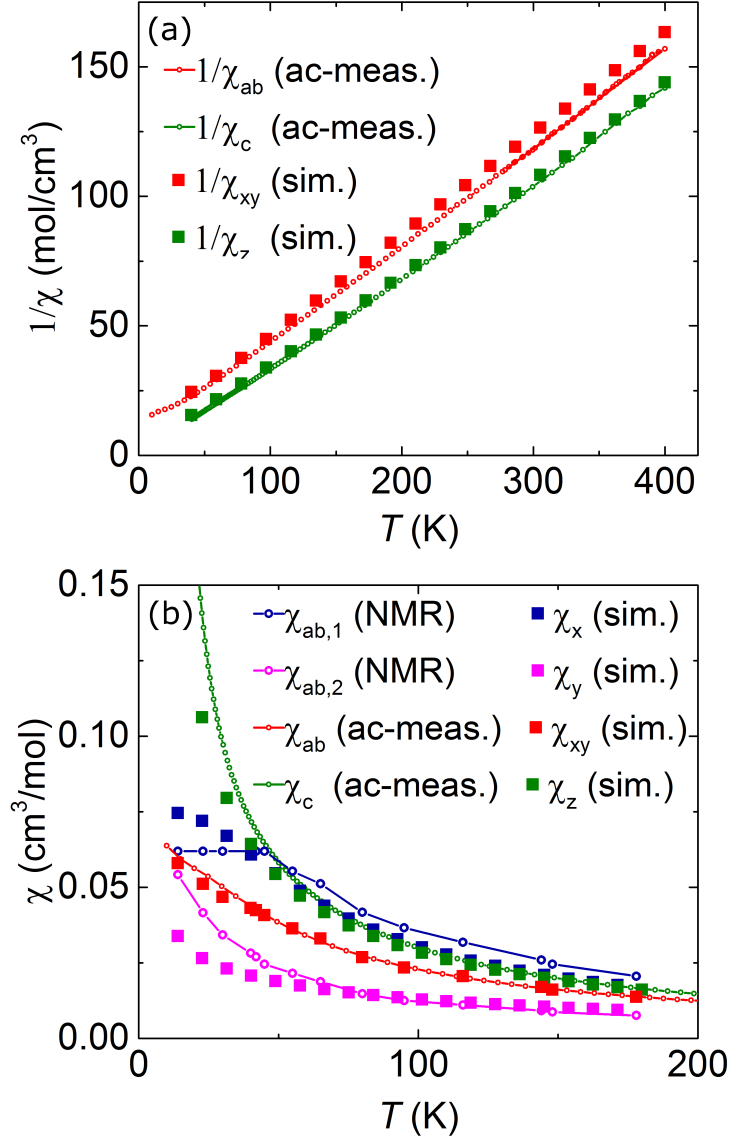
Figure 5.5: Measured and fitted (a) inverse susceptibility and (b) susceptibility of $YbNi_4P_2$. Measured data, both from AC and from NMR measurements, are shifted to account for the Kondo effect (see text). In the McPhase fit, the axes were chosen such that $z \parallel c$, but x and y were rotated by 45° with respect to a and b. The AC-measured χ_{ab} in the right graph is shown for completeness, but was not fitted. Otherwise, the large squares correspond exactly to those points where the fit is based.

minimum of the fit are:

$$\phi_0 = \pm 0.93 \left| \mp {}^5\!/_2 \right\rangle \pm 0.33 \left| \mp {}^1\!/_2 \right\rangle \mp 0.15 \left| \pm {}^7\!/_2 \right\rangle \pm 0.08 \left| \pm {}^3\!/_2 \right\rangle$$
$$\phi_1 = \pm 0.69 \left| \mp {}^3\!/_2 \right\rangle \pm 0.67 \left| \mp {}^7\!/_2 \right\rangle \pm 0.27 \left| \pm {}^1\!/_2 \right\rangle \mp 0.05 \left| \pm {}^5\!/_2 \right\rangle$$
$$\phi_2 = \mp 0.70 \left| \mp {}^7\!/_2 \right\rangle \pm 0.50 \left| \mp {}^3\!/_2 \right\rangle \pm 0.42 \left| \pm {}^1\!/_2 \right\rangle \mp 0.30 \left| \pm {}^5\!/_2 \right\rangle$$
$$\phi_3 = \pm 0.80 \left| \mp {}^1\!/_2 \right\rangle \mp 0.52 \left| \pm {}^3\!/_2 \right\rangle \mp 0.21 \left| \mp {}^5\!/_2 \right\rangle \pm 0.20 \left| \pm {}^7\!/_2 \right\rangle$$

The ground state is strongly dominated by the $m_J = \pm {}^5\!/_2$ state, which is a direct consequence of the requirement that one of the neutron transition matrix elements should vanish, since the transition from the ${}^5\!/_2$ to the ${}^1\!/_2$ state does not fulfill $\Delta m_J = \pm 1$. The calculated saturation moment of this ground state is 2.5 μ_B/Yb for $B \parallel c$. So far, no magnetisation measurement exist where saturation has been reached. However, a measurement by Kristin Kliemt at 2 K yields only $\mu_c = 1.24$ μ_B/Yb at 9 T. This implies that a rather large field of around 25 T would be needed to reach saturation, if the calculated saturation moment was correct.

Table 5.2 includes a confidence interval for each parameter where the standard deviation of the fit is within 10% of the optimum standard deviation; these values were calculated for all other parameters at their optimum value. If all parameters are varied simultaneously, this range is slightly larger due to the inter-dependence of the parameters. It can be seen that the fit is very insensitive to some of the parameters, particularly the values of B_6^m. Also the fitted values of B_4^m have a rather large error bar, and only the values of B_2^m can be fitted reliably. This is caused by the large parameter space, in combination with the relatively small amount of experimental data. It should be noted that the coefficients of the CEF wave functions are much more sensitive to a variation of the B_l^m parameters than the fit quality, so that equations 5.6 only give a rough idea of the true wave functions.

Thus, the fit results give a range of possible solutions rather than a full determination of the CEF scheme: The true parameter set should lie within the range presented here, since other parameter sets are in contradiction to neutron and susceptibility measurements, but more experimental data would be needed to determine the crystal field parameters reliably. Unfortunately, the comparison of experimental data and calculated results necessarily suffers from two problems: Firstly, the presence of the Kondo effect, which can only be accounted for in a mean-field approximation; secondly, the co-occurrence of orthogonal site symmetry and tetragonal crystal structure. While the exact CEF scheme is difficult to determine, the result that the ground state is dominated by the $m_J = 5/2$ wave function seems a rather robust feature of the fits.

5.3 Magnetic fluctuations

The low-energy magnetic fluctuations in $YbNi_4P_2$ were studied by powder neutron spectroscopy. Measurements with thermal neutrons allowed the local response to be studied in a wide range of temperatures, while spectrometers using cold neutrons were used to measure to ferromagnetic fluctuations at low temperatures. The data presented in this section have been published in [HKE+15].

Experimental details

The data presented in this section originated from three different neutron scattering experiments:

- The measurement at IN4 which has already been described in some detail in section 5.2. However, for the measurement of the quasi-elastic fluctuations the incident neutron energy has been reduced to $E_i = 9$ meV ($\lambda_i = 3$ Å) to improve the energy resolution to 0.4 meV (FWHM). In this setting, the wavevector transfer at the elastic line ranged from 0.5 Å^{-1} to 3.5 Å^{-1}.

- A measurement at the cold-neutron time-of-flight spectrometer FOCUS (PSI). To increase the measured intensity, the IN4 powder sample was enlarged by further polycrystalline material from the same batches as before (63522/23/24/29) as well as the batches 63519/28/31; the total sample mass, including the prior neutron sample, was 15.56 g. The incident neutron energy was $E_i = 3.3$ meV ($\lambda_i = 5$ Å). This yielded a momentum transfer range at the elastic line of 0.4 Å^{-1} to 2.2 Å^{-1} and an energy resolution of 0.09 meV. The sample was cooled with a dilution refrigerator with a nominal base temperature of 35 mK. To support a uniform temperature distribution in the powder sample, ^{4}He at elevated pressure (10 bar at room temperature) was filled into the cylindrical copper sample holder.

- A measurement at the cold-neutron time-of-flight spectrometer ToFToF (FRM2). The experimental conditions were very similar to the measurement at FOCUS: The same sample, the same incident neutron energy and similar sample holders were used and cooling was achieved by a dilution fridge (nominal base temperature 60 mK) and ^{4}He at elevated pressure in the sample holder. ToFToF has more detectors at low angles so that wave vector transfers could be measured down to 0.2 Å^{-1}.

In all experiments, a measurement of the empty sample holder was performed so that it could be subtracted from the data. Due to the relatively large absorption cross section of ytterbium (34.8 barn), the data also needed to be corrected for self-absorption effects. In case of the IN4 data, where a flat sample holder was used, the angular correction is particularly important, since the neutron path length depends strongly on the scattering angle. For the cylindrical sample holders, the effect on the angle is much less pronounced [Wut12] and has therefore been neglected. For both set-ups, the absorption varies considerably between different energy transfers, since neutron absorption is proportional to $1/v$ (v being the velocity) in absence of resonances [Pri06]. The neutron transmission T_n of every spectrum is calculated as

$$T_n(v) = \exp(-\frac{\sigma_0 \cdot v_0}{v} \cdot r \cdot \frac{Z}{V} \cdot \frac{\rho_{\mathrm{ideal}}}{\rho_{\mathrm{powder}}}), \qquad (5.6)$$

where $\sigma_0 = 53.1$ barn is the tabulated absorption cross section of one formula unit YbNi$_4$P$_2$ at $v_0 = 2200$ m/s, r the radius of the sample holder (or the thickness in case of flat sample holders), V the unit cell volume, Z the number of formula units in V, and $\rho_{\mathrm{ideal}}/\rho_{\mathrm{powder}}$ accounts for the density ratio of an ideal single crystal to powder, which is roughly 2. Using the radius rather than the diameter assumes that scattering events most likely take place at the centre of the cylinder; the absorption contribution of the neutrons prior to scattering is neglected since it is constant. In case of strong absorption ($T_n \approx 0.5$ at the elastic line) it would be correct to apply the absorption correction before subtracting the empty can data, which corresponds to subtracting only a fraction of the empty can signal. However, there are also large background signals that do not involve a neutron passing the sample, such as cryostat scattering or direct beam contamination at low angles. To account for these effects, the full empty can signal needs to be subtracted. Since the latter features have a pronounced dependence on Q and E, while the signal of the empty can is rather featureless, it is more beneficial for the data analysis to subtract the full empty can signal and subsequently do the absorption correction.

All measurements were normalised to a monitor that was placed in the beam in front of the sample. Comparison between experiments performed at different instruments was done by normalisation to the integrated intensity of the incoherent elastic scattering.

At IN4, the non-magnetic reference LuCo$_4$Ge$_2$ was also measured. Thus it was ensured that the low-energy signal is indeed of magnetic nature; no phonons are observed in the relevant range of energy and momentum transfer. Foreign phases in the sample can also be excluded as the origin of a low-temperature magnetic signal, as has been discussed in section 5.2.

Since the magnetic signal in $YbNi_4P_2$ is very weak, an excellent signal-to-background ratio at low energy transfers is needed for a proper data evaluation. At IN4, the background signal was relatively small compared to the magnetic signal and could be fitted very well from the reference spectra. However, the data measured at FOCUS, see figure 5.6, suffered from much stronger background effects due to double scattering from the vacuum can of the dilution cryostat. Additionally, $\lambda/2$ scattering resulted in a peak at $E \approx 1.1$ meV. In total, the background signal at positive energy transfers was stronger than the magnetic signal. One can attempt to subtract a constant background fitted to the vanadium spectrum, but the accuracy of the fits to the magnetic signal is very poor. These difficulties motivated the experiment at ToFToF, where a boron nitride shield was placed into the vacuum can of the cryostat. The shield was a cylindrical segment of 160° which covered the can opposite to the detector bank. This successfully suppressed double scattering. Furthermore, the instrument ToFToF has a larger incident neutron flux than FOCUS and a set of 7 choppers instead of a single crystal monochromator, which prevents $\lambda/2$ contaminations. In total, the signal-to-background ratio could be improved drastically, which allowed reliable fitting of the magnetic signal.

Despite the use of ^{4}He at elevated pressure in the experiments at FOCUS and ToFToF, cooling to dilution fridge temperatures seems to have failed, since all data taken at very low temperatures fall on top of each other. Based on the intensity at small negative energy transfers (-1 meV $< \Delta E <$ -0.1 meV), which is very sensitive to the Bose factor, the lowest real sample temperature is estimated to be 1 K. All data discussed in this section are thus taken in the paramagnetic phase of $YbNi_4P_2$.

Local quasi-elastic response

A quasi-elastic signal is observed if the lifetime of an excitation is so short that the energy width becomes larger than the excitation energy, so that it effectively appears at zero energy transfer. As before, an exponential decay of the lifetime is assumed, which leads to a Lorentzian-type scattering function

$$S(Q, E) = \frac{1}{1 - \exp(-\frac{E}{k_B T})} \cdot \frac{2E\chi(Q)}{\pi\Gamma \left(1 + \frac{2E}{\Gamma}\right)^2}. \tag{5.7}$$

The first term represents the Bose factor and Γ is the full width of the peak. In case of local fluctuations, which appear in paramagnetic samples at all temperatures, $\chi(Q)$ is constant except for the magnetic form factor. Therefore, the local magnetic response in $YbNi_4P_2$ was analysed by averaging all spectra between 0.6 Å^{-1} and 1.8 Å^{-1}. To describe the measured intensity,
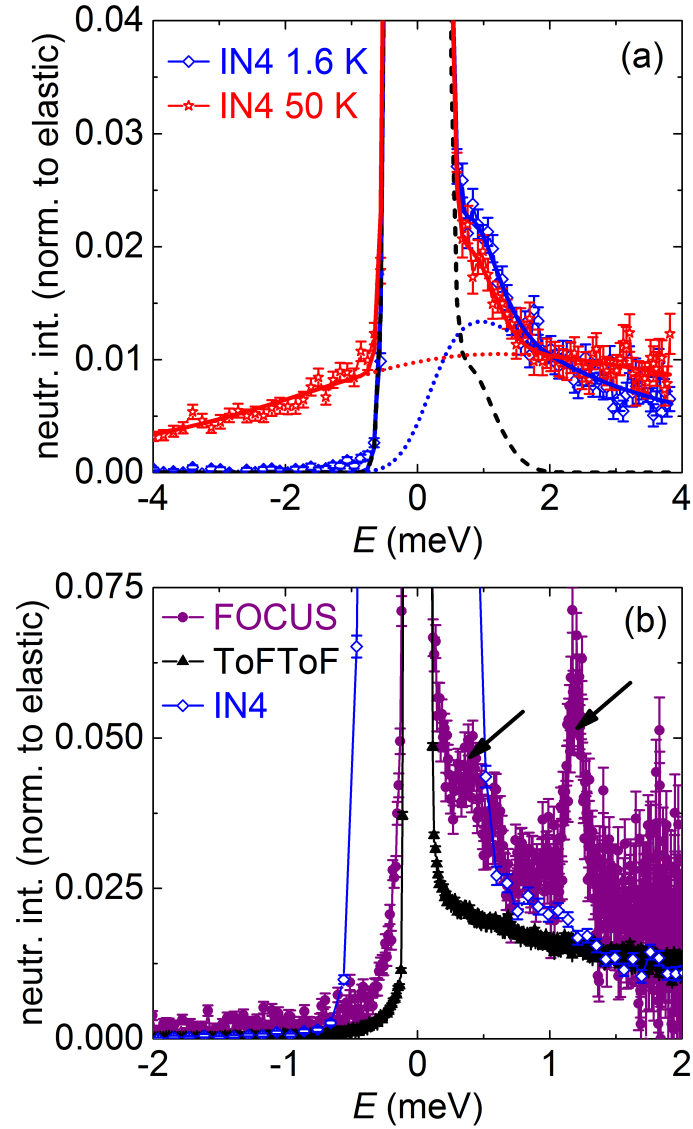
Figure 5.6: Quasi-elastic magnetic signal of YbNi$_4$P$_2$ at $Q = 1.2 \pm 0.6$ Å^{-1}. (a) Data measured at IN4 ($E_i = 9$ meV) at 1.6 K (blue) and 50 K (red). The background, fitted to the non-magnetic reference LuCo$_4$Ge$_2$, is shown in black, the fitted magnetic signal in dashed blue/red lines and the total fit function in solid blue/red lines. (b) Comparison of data measured at IN4, FOCUS and ToFToF, the latter two at $E_i = 3.3$ meV. All data were measured at ≈ 1.5 K and normalised to the integrated intensity of the elastic line. The arrows mark the pronounced spurious peaks in the FOCUS data, caused by double scattering (left arrow) and $\lambda/2$ contaminations (right arrow).
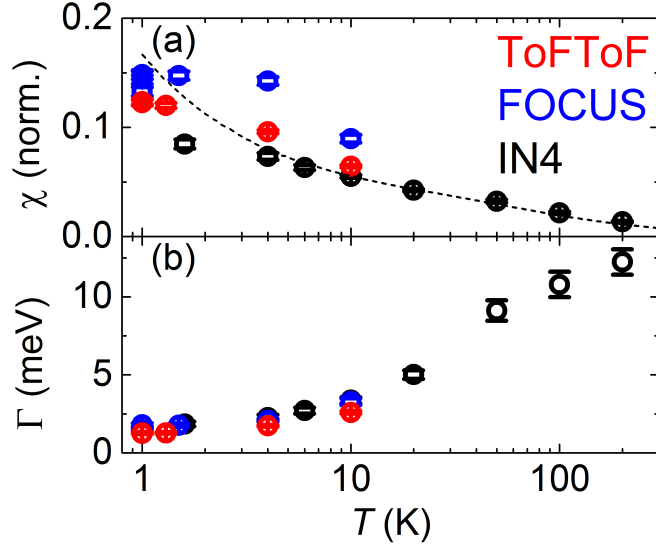
Figure 5.7: (a) Fitted susceptibility and (b) width (FWHM) of the quasi-elastic magnetic signal of $YbNi_4P_2$ at $Q = 1.2 \pm 0.6$ Å^{-1}, based on data measured at IN4, FOCUS and ToFToF. For the comparison of the susceptibility, data were normalised to the integrated intensity of the elastic line. The dashed line shows the bulk susceptibility, based on the AC measurement published in [SKL+13].

it is necessary to convolute $S(Q,E)$ with the spectrometer resolution and to add the elastic line as well as a background signal. In the Q-range till 1.8 Å^{-1}, only weak Bragg peaks appear, so that the elastic signal is mostly incoherent. There are no crystal electric field excitations in the considered spectral range, see also section 5.2.

The local magnetic response of $YbNi_4P_2$ was measured at IN4 at temperatures between 1.6 K and 200 K and at FOCUS and ToFToF at temperatures between 1 K and 10 K. Some exemplary data and fits according to equation 5.7 are shown in figure 5.6. The fitted susceptibility χ and full width Γ of the local magnetic response are shown in figure 5.7. It should be noted that the fits at 10 K are less reliable for the FOCUS and ToFToF data since the width of the signal exceeds the energy transfer range accessible at $E_i = 3.3$ meV. The FOCUS data are generally more difficult to fit due to the strong double scattering, which most likely causes the discrepancy of the fitted susceptibility between the FOCUS data and the IN4/ToFToF data. The fitted local susceptibility in the temperature range 1 - 200 K behaves roughly as the bulk susceptibility [SKL+13]. The fitted half width of

the local response seems to saturate at low temperatures, with a saturation
width $\Gamma/2 \approx 0.8$ meV ($\widehat{=}$ 9 K). In Kondo systems, the width of the local
quasi-elastic neutron scattering is expected to take approximately the value
of the Kondo temperature T_K for $T < T_K$ [CBW86]. The agreement with
the Kondo temperature estimated from thermodynamic measurements, $T_K =$
8 K, is very good [KLS$^+$11].

Ferromagnetic fluctuations

Additionally to the local response, a magnetic sample may show a response
at certain wave vectors, which depends on the magnetic interactions of the
compound. For a ferromagnetic material one expects a magnetic response
at $Q = 0$ at temperatures approaching the ordering temperature, which is
170 mK in YbNi$_4$P$_2$. Therefore, the quasi-elastic response was analysed as a
function of momentum transfer for the data measured at ToFToF (temper-
ature range 1 - 10 K). The susceptibility, again fitted according to equation
5.7, is shown in panel (a) of figure 5.8. For $T \approx 1$ K, the quasi-elastic re-
sponse becomes much more pronounced towards $Q = 0$, indicating ferromag-
netic fluctuations. Despite the fact that the measurement temperature is still
almost an order of magnitude higher than the ordering temperature, the re-
sponse at the lowest measured Q values is considerably enhanced by a factor
of two compared to $Q > 0.6$ Å^{-1}. The correlation length of the fluctuations
can be estimated from the Q width and amounts to a few Å, which roughly
corresponds to the nearest-neighbour distance of 3.6 Å along the ytterbium
chains [KCB00].

   The same fit results are presented in a different way in panels (b) and (c)
of figure 5.8: Spectra averaged between 0.6 Å^{-1} and 1.8 Å^{-1} (as above) are
compared to spectra averaged between 0.32 Å^{-1} and 0.52 Å^{-1}. 5.8(b) shows
how the intensity of the low-Q response becomes gradually larger than the
local response as the temperature is lowered from 10 K to 1 K. 5.8(c) shows
the fitted width, which is much sharper at small momentum transfers than
the Kondo-limited width of the local response. However, also the width
at 10 K is smaller in the low-Q range, indicating that already at this high
temperature the lifetime of ferromagnetic fluctuations is enhanced compared
to the local response. Between 10 K and 1 K, the width of the low-Q signal is
reduced by more than a factor of 3, which denotes considerable slowing down.
On further lowering the temperature, critical slowing down is expected for Q
approaching zero.

   The results show that the $Q = 0$ response is clearly different from the
local response, giving evidence for the ferromagnetic interactions in YbNi$_4$P$_2$.
Considering that the sample temperature was well above T_C, the observed
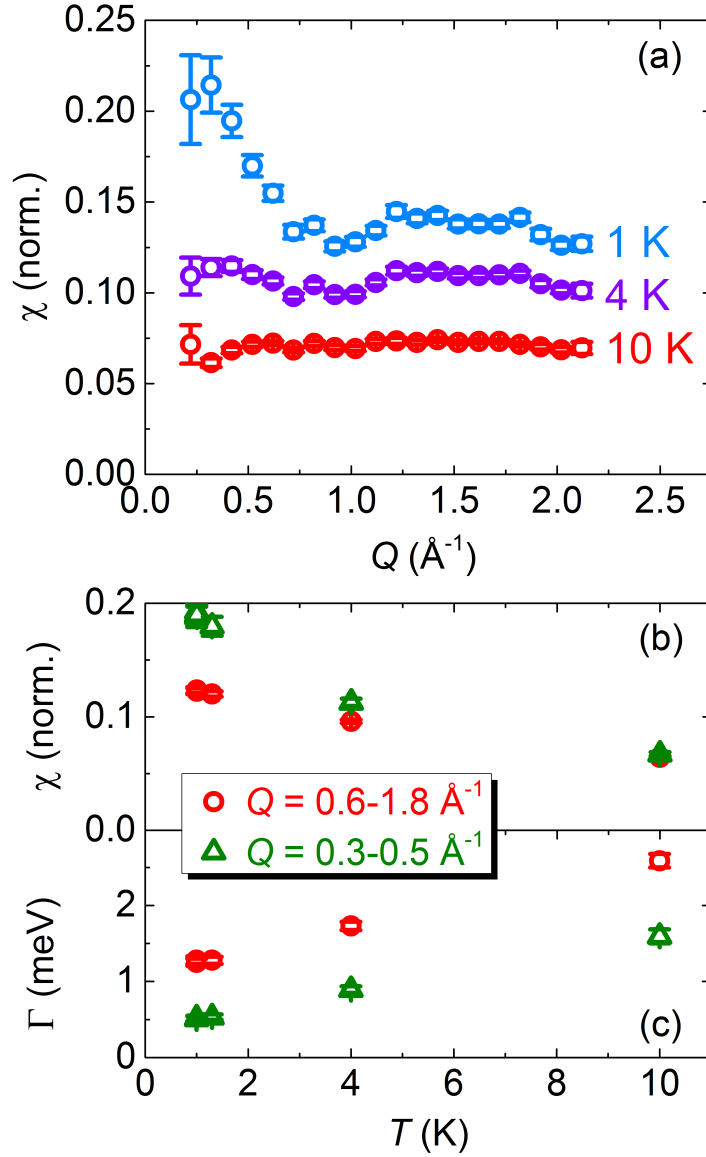
Figure 5.8: Ferromagnetic response of YbNi$_4$P$_2$, measured at ToFToF. (a) Fitted susceptibility as a function of wave vector transfer Q. (b) Fitted susceptibility and (c) width (FWHM) as a function of temperature, for either small wave vector transfers or general wave vector transfers, describing the ferromagnetic and the local response, respectively. Published in reference [HKE$^+$15].

effects are rather large. Particularly surprising is the enhancement of the lifetime at temperatures as high as 10 K. These results might be a sign for frustration in YbNi$_4$P$_2$, or fluctuations induced by the low dimensionality.

Chapter 6

Concluding discussion

In this thesis, three heavy-fermion systems have been studied by neutron scattering. $CeCu_2Si_2$ is a prototypical heavy-fermion compound, which continues to attract attention due to its unconventional superconductivity. Here single crystal neutron spectroscopy was used to gain insights into the interplay of magnetism and superconductivity. CePdAl also shows Kondo characteristics, but is unusual among Kondo systems because the magnetic order is partially frustrated. Detailed single-crystal diffraction studies were performed to obtain a better understanding of the partially frustrated state. The third compound, $YbNi_4P_2$, is exceptional among heavy-fermion systems for its ferromagnetic order at very low temperatures. Its low-temperature magnetic fluctuations were investigated by powder neutron spectroscopy.

$CeCu_2Si_2$ is a heavy-fermion compound which is naturally located very close to a quantum critical point, i.e. without application of magnetic field, pressure or element substitution. Slight variations in the stoichiometry can tune samples from the sub-critical, antiferromagnetic regime to the critical or over-critical regime, where the ground state is superconducting. Some samples, which are just sub-critical, show both phases with $T_c < T_N$. The proximity of pure $CeCu_2Si_2$ to quantum criticality strongly facilitates experiments, particularly neutron scattering experiments, since no pressure cells or magnets are needed. However, it also implies challenges for the sample growth: The growth conditions give only limited control over the ground state of the synthesised crystal. Moreover, concentration gradients in large samples result not only in a distribution of critical temperatures, but also in different ground states within one single crystal. This was actually observed for all samples synthesised and studied in this thesis: The A-type $CeCu_2(Si_{0.98}Ge_{0.02})_2$ crystal showed filamentary superconductivity below 0.4 K, the S-type $CeCu_2Si_2$ crystal had short-ranged antiferromagnetic order [SAF$^+$11], and the A/S-type $CeCu_2(Si_{0.98}Ge_{0.02})_2$ crystal showed a large distribution of T_c as well

as residual antiferromagnetic order at the lowest measured temperatures. Therefore, it should be kept in mind that the nominal ground state of a sample only refers to the majority phase.

There has earlier been a discussion about the co-existence or competition of magnetic order and superconductivity in $CeCu_2(Si_{1-x}Ge_x)_2$ [FAG$^+$97, KIO$^+$02, FSS$^+$07]. The work of Julia Arndt [ASB$^+$09, Arn10] suggested that competition is found for pure $CeCu_2Si_2$ or low Ge substitution, but co-existence is observed for larger Ge substitution. This is in line with theoretical predictions and seems to relate to the relative magnitude of T_c and T_N [KM88]. The data for the A-type and the A/S-type crystal which are presented in this thesis are in agreement with Arndt's findings. Therefore, the discussion of the results is based on the assumption that $CeCu_2Si_2$ and $CeCu_2(Si_{0.98}Ge_{0.02})_2$ behave in principal identically.

A central question of this study was how the inelastic response of different $CeCu_2Si_2$ samples reflects the drastically different thermodynamic properties which are observed in this small region of the phase diagram around the QCP. In an extension to prior results [SFS$^+$06, SAF$^+$11, ASS$^+$11], it can be summarised that the response is gapped in the superconducting state, for both S-type and A/S-type samples, but gapless in the paramagnetic and the antiferromagnetic state, for A-type samples at all temperatures and A/S-type and S-type samples for $T > T_c$ or $B > B_{c2}$. The size of the gap is of the order of 0.15-0.2 meV. The lifetime of the fluctuations is enhanced in the magnetically ordered state, but otherwise similar for the different types of samples at any given temperature. The susceptibility increases towards smaller values of the tuning parameter r, i.e. $\chi(A-type) > \chi(A/S-type) \gg \chi(S-type)$, as expected from the Doniach diagram [Don77].

For the A-type and the S-type sample, the dispersion of the inelastic response was studied (see also references [SAF$^+$11, ASS$^+$11]). A linear dispersion relation is observed up to around 1 meV, where it becomes difficult to follow the dispersion further due to strong damping. The data for the A-type crystal are nearly identical below and above T_N for $\Delta E \gtrsim 0.15$ meV. The comparison of the A- with the S-type sample showed that their dispersion is very similar when superconductivity is suppressed ($T > T_c$ or $B > B_{c2}$), and still rather similar within the superconducting phase for energies larger than the gap size. Thus, it can be concluded that the changes in the ground state between antiferromagnetic, paramagnetic and superconducting state are only reflected in the inelastic response for $\Delta E \lesssim 0.2$ meV.

For unconventional superconductors, paramagnons are supposed to provide the pairing glue for the Cooper pairs, in a similar way that phonons do for conventional superconductors. The dynamical spin susceptibility $\chi(\mathbf{Q}, \omega)$ then enters into the effective interaction between quasiparticles, which can

be attractive for certain values of $\mathbf{Q}$ and ω [MPL07] and possibly lead to Cooper-pair formation. An enhanced susceptibility is expected at the border of a magnetic state, making magnetic quantum critical points a likely place to find superconducting phases. This might explain the similarity between the phase diagrams of heavy-fermion, cuprate and pnictide superconductors [Sca12]. Neutron scattering can directly measure $\chi(\mathbf{Q}, \omega)$ and therefore constitutes the ideal tool to provide microscopic proof of any spin interaction theory. For $CeCu_2Si_2$, strong evidence for magnetically mediated superconductivity came from the observation of spin fluctuations at Q_{AF}, the same wave vector where magnetic order is found in the antiferromagnetic state [SAF+11]. The gap opening in the superconducting state results in an exchange energy saving which is much larger than the superconducting condensation energy. In this thesis, these results were extended by comparing $\chi(\mathbf{Q}, \omega)$ of the antiferromagnetic and the superconducting samples in a wider inelastic interval. Thus, it could be shown that the excitations are not only centred around the same wave vector, but are nearly identical over a large range of energy transfers. Thereby a microscopic justification was given for the statement that magnetic fluctuations associated with the nearby ordered state drive superconductivity.

For the A-type crystal, the anisotropy of the dispersion between the *ab*-plane and the *c*-axis was also measured. Both directions behave identically within the error bars of the experiment. This has important implications for any model that aims to describe the relation of magnetic interactions with superconductivity in $CeCu_2Si_2$. Often unconventional superconductivity is discussed in terms of 2-dimensional models, particularly for the cuprates, but also for some pnictides and heavy-fermion compounds [Sca12]. The results demonstrate that 3-dimensional models are clearly needed for $CeCu_2Si_2$, as has also been suggested for the isostructural '122' iron-pnictide compounds [Sca12].

$CeCu_2Si_2$ is also often discussed as a model system for the Hertz-Millis-Moriya scenario. A central element of the theory is the dynamical critical exponent z, which is assumed to be 2 for an antiferromagnet. Furthermore, the theory predicts $\xi^{-2} \propto T^{1+1/z}$, which implies $\xi_\tau \propto T^{-3/2}$ if $z = 2$. The most suitable sample to study the quantum-critical behaviour of $CeCu_2Si_2$ is the S-type crystal, which is located rather close to the magnetic instability. Superconductivity needs to be suppressed in a field $B > B_{c2}$. In earlier neutron scattering measurements, Arndt *et al.* [ASS+11] have confirmed the $T^{-3/2}$ dependence for the lifetime. In the experiment presented in this thesis, the aim was to measure the exponent for the correlation length. The appearance of propagating paramagnons in the S-type sample makes this experiment difficult. The data suggest a sub-linear dependence of the correlation length

on the temperature, and are thus in agreement with $\xi^{-2} \propto T^{1+1/z}$ for $z = 2$. Furthermore, z was estimated from a direct comparison of the energy width Γ and the Q-width κ measured at the same temperatures. Here, $z = 1.6 \pm 0.2$ was found, slightly smaller than the expected value of 2. This offset is not necessarily in contradiction to the Hertz-Millis-Moriya scenario. It could either be related to the experimental challenges, or be caused by the the fact that the measured sample is not directly located at $r = r_{\mathrm{c}}$.

The next part of this thesis was focussed on the partially frustrated magnetic state of CePdAl, where one third of the cerium moments does not participate in the long-range magnetic order. The ground state of these moments remains to be clarified. From the powder neutron diffraction data [KDKvdB02], it was deduced that they are disordered down to lowest temperature. A powder NMR study [OMN$^+$08] came to the conclusion that the disordered third of the moments enters into a Fermi-liquid state at low temperatures, with a vanishing local moment, and that this relieves the frustration of the compound while keeping the partial order intact. However, recent heat capacity measurements suggest the appearance of a gap in the low-temperature state of CePdAl, which might hint to a spin liquid state of the frustrated moments [FHL$^+$].

The single crystal neutron diffraction data presented here allow further insights into the peculiar magnetic order of CePdAl. Firstly, it was found that the intensity of the forbidden reflections is finite below T_{N}, while it should be zero if the remaining third of the cerium ions was truly disordered. The increased Q-width of these reflections shows that they order only at short range. It can be speculated that the ordered moment on that cerium site also fluctuates in time, although the diffraction data give no information about that. This fluctuating order of the nominally disordered spins can be expected to interfere with the long-range order of the other two thirds of the magnetic moments. Interestingly, the data show that the correlation length (or domain size) of the long-range order is limited at low temperatures, becoming gradually shorter with decreasing temperature. The link between these two observations, the appearance of the forbidden reflections and the shortening of the correlation length of the long-range order, cannot be established with certainty on the basis of the present data; temperature-dependent measurements of intensity and width of the forbidden reflections are necessary to see if a correlation exists. Such measurements will be conducted in the near future. It should be noted that the observed temperature dependence of the correlation length is not in line with a disorder-induced limit of the magnetic interactions, since this should be temperature independent.

These data seem to contradict the conclusions of Keller *et al.* [KDKvdB02] and Oyamada *et al.* [OMN$^+$08]: The frustrated moments are apparently not

truly disordered, and a heavy-fermion state with a quenched moment could not explain the shortening of the correlation length. Rather, if the moment on the frustrated spins vanished, this should stabilise the order of the remaining two thirds. Whether the ground state of the disordered moments might be a spin liquid cannot be decided on the basis of the neutron diffraction data. Future plans involve studying the development of both allowed and forbidden reflections under conditions that alter the magnetic frustration, such as uniaxial pressure or magnetic field in the basal plane. These experiments might make it possible to disentangle influences from the frustration and the Kondo effect, since the latter should stay constant in small fields or pressures.

Single-crystal data also allow the anisotropy of magnetic interactions to be studied. Surprisingly, it was found that the anisotropy of the correlation length between the basal plane and the c-axis is rather small, both for the correlations above T_N, and for the long-range order below T_N. This shows that a two-dimensional model for the magnetic interactions, as given by [NnRLC97], is clearly insufficient to understand the ordering of CePdAl, as the in-plane and out-of-plane interactions are of comparable magnitude. This is already suggested by the inter-atomic distances: The nearest and next-nearest neighbour coupling within the basal plane, which are considered in the model of Núñez-Regueiro et $al.$ [NnRLC97], correspond to distances of 3.73 Å and 5.25 Å; the out-of-plane distance of 4.24 Å is just in between these two. Therefore, a model of all interactions, including the out-of-plane component, is highly desirable.

The magnetic order in CePdAl can be suppressed by Ni substitution on the Pd site [FBG$^+$14]. A quantum critical point is reached for a Ni content of around 14%. It is interesting to see if the frustration has any influence on the criticality. As a first step, it must be confirmed that the magnetic order stays the same under Ni substitution: This has been done in single crystal diffraction experiments on $CePd_{0.95}Ni_{0.05}Al$ and $CePd_{0.9}Ni_{0.1}Al$, where the same ordering vector was found as in the pure compound. Short-ranged correlations at the same Q-vector were also observed for $CePd_{0.86}Ni_{0.14}Al$ [SL], so that it is rather certain that the same type of order exists in the relevant range of the phase diagram. As a next step, it would be interesting to know what happens to the frustration on increasing Ni substitution. Unfortunately, the experimental set-up prevented the measurement of the forbidden reflections, and broadening induced by disorder made it impossible to see if the correlation length shows any temperature development. However, the data show that the ordered moment is linearly suppressed with Ni substitution and Néel temperature, with a vanishing ordered moment at the critical concentration. If frustration increased with Ni substitution, it would be ex-

pected that the ordering temperature is suppressed faster than the ordered moment. The observed proportionality suggests that the suppression of the order through Ni substitution is driven by the Kondo effect, while frustration stays roughly constant. How the frustration of one third of the moments influences the quantum critical behaviour of the remaining two thirds is an exciting topic for further investigations, both by neutron scattering and by thermodynamic measurements.

The third compound studied in this thesis, $YbNi_4P_2$, has only recently attracted interest with respect to its quantum critical behaviour [KLS+11]. Thus, many basic questions need to be settled, such as the crystal electric field scheme. This question concerned the first part of the chapter about $YbNi_4P_2$. The transition energies were measured by powder neutron spectroscopy: Two transitions from the ground state were found at 8.5 meV and 12.5 meV. Because of the orthorhombic site symmetry of Yb, it is expected that the $J = 7/2$ state splits into four doublets. This suggests that one transition cannot be observed by neutron scattering due to a vanishing transition matrix element. From a comparison with heat capacity measurements, the additional level is estimated to be at 25 meV.

A more detailed analysis was done using the programme package McPhase. Here the crystal electric field scheme was evaluated by simultaneously fitting data from neutron scattering, heat capacity, AC susceptibility and NMR measurements; the latter two also contained information about the anisotropy of the magnetism. This analysis yielded the level scheme $\Delta E_1 = 8.1$ meV, $\Delta E_2 = 12.1$ meV and $\Delta E_3 = 29.5$ meV. The ground state wave function was found to be dominated by the $m_J = 5/2$ state. This is in poor agreement with currently available magnetisation measurements, since the analysis does not capture the influence of the Kondo effect properly, while $YbNi_4P_2$ clearly behaves like a Kondo system in small fields. Large fields of the order of 30 T are needed to reveal the full saturation moment without the Kondo effect, which can then be compared with the calculated ground state. Such high-field magnetisation measurements are under way to clarify the matter.

Furthermore, the magnetic fluctuations of $YbNi_4P_2$ were studied. Local, quasi-elastic fluctuations were observed at all temperatures. Their width becomes smaller as the temperature is lowered, but saturates at low temperatures. The saturation width $\Gamma/2 \approx 0.8$ meV corresponds well to the Kondo temperature of 8 K found in thermodynamic measurements [KLS+11]. Since $YbNi_4P_2$ is ferromagnetic below $T_C = 170$ mK, enhanced magnetic fluctuations are expected at low temperatures for $Q = 0$. Unfortunately, the lowest temperature reached in the neutron experiment was around 1 K, since the powder thermally decoupled from the dilution refrigerator. Nevertheless, magnetic fluctuations with enhanced susceptibility and lifetime were observed

for $Q \to 0$, providing a microscopic verification of the ferromagnetic nature of the interactions in YbNi$_4$P$_2$.

Very recently, large single crystals of YbNi$_4$P$_2$, suitable for inelastic neutron scattering, have become available. These will allow the ferromagnetic fluctuations to be studied down to much lower temperatures $T \approx T_{\mathrm{C}}$, so that the critical behaviour can be analysed. Moreover, it will be possible to investigate the directional dependence of these fluctuations. This is particularly interesting for YbNi$_4$P$_2$, since theoretical calculations suggested a special role of transverse fluctuations, which result in ferromagnetic order along the hard axis [KPG14].

Bibliography

[ABMC84]   F. Aliev, N. Brandt, V. Moshchalkov, and S. Chudinov. Electric and magnetic properties of the Kondo-lattice compound $CeCu_2Si_2$. *Journal of Low Temperature Physics*, 57(1-2):61–93, 1984.

[AG61]   A. Abrokosov and L. Gorkov. Contribution to the theory of superconducting alloys with paramagnetic impurities. *SOVIET PHYSICS JETP-USSR*, 12(6):1243–1253, 1961.

[Arn10]   J. Arndt. *Wechselspiel von Magnetismus und Supraleitung im Schwere-Fermionen-System* $CeCu_2Si_2$. PhD thesis, Technical University Dresden, 2010.

[ASB+09]   J. Arndt, O. Stockert, R. Borth, E. Faulhaber, K. Schmalzl, A. Schneidewind, H. S. Jeevan, C. Geibel, M. Loewenhaupt, and F. Steglich. Do antiferromagnetism and superconductivity coexist in 2% and 10% Ge doped $CeCu_2Si_2$? *Journal of Physics: Conference Series*, 150(4):042008, 2009.

[ASF+10]   J. Arndt, O. Stockert, E. Faulhaber, P. Fouquet, H. S. Jeevan, C. Geibel, M. Loewenhaupt, and F. Steglich. Characteristics of the magnetic order in $CeCu_2Si_2$ revealed by neutron spin-echo measurements. *Journal of Physics: Conference Series*, 200(1):012009, 2010.

[ASS+11]   J. Arndt, O. Stockert, K. Schmalzl, E. Faulhaber, H. S. Jeevan, C. Geibel, W. Schmidt, M. Loewenhaupt, and F. Steglich. Spin fluctuations in normal state $CeCu_2Si_2$ on approaching the quantum critical point. *Phys. Rev. Lett.*, 106:246401, 2011.

[BBGK15]   M. Brando, D. Belitz, F. Grosche, and T. Kirkpatrick. Metallic quantum ferromagnets. *arXiv:1502.02898*, 2015.

[Blu01]   S. Blundell. *Magnetism in Condensed Matter*. Oxford Univ. Press, 2001.

[BPV11]   A. Benlagra, T. Pruschke, and M. Vojta. Finite-temperature spectra and quasiparticle interference in Kondo lattices: From light electrons to coherent heavy quasiparticles. *Phys. Rev. B*, 84:195141, 2011.

[CBW86]   D. Cox, N. Bickers, and J. Wilkins. Calculated properties of valence fluctuators. *Journal of Magnetism and Magnetic Materials*, 54–57, Part 1(0):333–337, 1986.

[CN10]   P. Coleman and A. H. Nevidomskyy. Frustration and the Kondo effect in heavy fermion materials. *Journal of Low Temperature Physics*, 161(1-2):182–202, 2010.

[Col89]   M. F. Collins. *Magnetic Critical Scattering*. Oxford Univ. Press, 1989.

[DEM$^+$96] A. Dönni, G. Ehlers, H. Maletta, P. Fischer, H. Kitazawa, and M. Zolliker. Geometrically frustrated magnetic structures of the heavy-fermion compound CePdAl studied by powder neutron diffraction. *Journal of Physics: Condensed Matter*, 8(50):11213, 1996.

[DLG$^+$14] P. Das, S.-Z. Lin, N. J. Ghimire, K. Huang, F. Ronning, E. D. Bauer, J. D. Thompson, C. D. Batista, G. Ehlers, and M. Janoschek. Magnitude of the magnetic exchange interaction in the heavy-fermion antiferromagnet CeRhIn$_5$. *Phys. Rev. Lett.*, 113:246403, 2014.

[Don77]   S. Doniach. The Kondo lattice and weak antiferromagnetism. *Physica B+C*, 91:231–234, 1977.

[DS82]   H.-U. Desgranges and K. Schotte. Specific heat of the Kondo model. *Physics Letters A*, 91(5):240–242, 1982.

[EH00]   C. Enns and S. Hunklinger. *Tieftemperaturphysik*. Springer, 2000.

[Ehr33]   P. Ehrenfest. Phasenumwandlungen im ueblichen und erweiterten Sinn, classifiziert nach den entsprechenden Singularitaeten des thermodynamischen Potentiales. *Proceedings Koninklijke Akademie van Wetenschappen*, 36:153–157, 1933.

[FAG$^+$97]   R. Feyerherm, A. Amato, C. Geibel, F. N. Gygax, P. Hell-mann, R. H. Heffner, D. E. MacLaughlin, R. Müller-Reisener, G. J. Nieuwenhuys, A. Schenck, and F. Steglich. Competition between magnetism and superconductivity in CeCu$_2$Si$_2$. *Phys. Rev. B*, 56:699–710, 1997.

[Faw88]   E. Fawcett.   Spin-density-wave antiferromagnetism in chromium. *Rev. Mod. Phys.*, 60:209–283, 1988.

[FBG$^+$14]   V. Fritsch, N. Bagrets, G. Goll, W. Kittler, M. J. Wolf, K. Grube, C.-L. Huang, and H. v. Löhneysen. Approaching quantum criticality in a partially geometrically frustrated heavy-fermion metal. *Phys. Rev. B*, 89:054416, 2014.

[FHB$^+$13]   V. Fritsch, C.-L. Huang, N. Bagrets, K. Grube, S. Schumann, and H. v. Löhneysen. Magnetization and specific heat of CePd$_{1-x}$Ni$_x$Al. *physica status solidi (b)*, 250(3):506–510, 2013.

[FHL$^+$]   V. Fritsch, Z. Huesges, S. Lucas, A. Sakai, W. Kittler, C. Taubenheim, E. Green, S. Woitschach, H. von Löhneysen, and O. Stockert. To be published.

[FMS09]   A. Furrer, J. Mesot, and T. Strässle. *Neutron Scattering in Condensed Matter Physics*. World Scientific, 2009.

[FSH$^+$15]   Fritsch, V., Stockert, O., Huang, C.-L., Bagrets, N., Kittler, W., Taubenheim, C., Pilawa, B., Woitschach, S., Huesges, Z., Lucas, S., Schneidewind, A., Grube, K., and Löhneysen, H. v. Role of the tuning parameter at magnetic quantum phase transitions. *Eur. Phys. J. Special Topics*, 224(6):997–1019, 2015.

[FSS$^+$07]   E. Faulhaber, O. Stockert, K. Schmalzl, H. Jeevan, M. Deppe, C. Geibel, F. Steglich, and M. Loewenhaupt. Spatial separation of antiferromagnetism and superconductivity in CeCu$_2$Si$_2$. *Journal of Magnetism and Magnetic Materials*, 310(2, Part 1):295–297, 2007.

[Ful95]   P. Fulde. *Electron Correlations in Molecules and Solids*. Springer Berlin Heidelberg, 1995.

[GFR$^+$]   P. Geselbracht, E. Faulhaber, M. Rotter, K. Schmalzl, D. Quintero-Castro, O. Stockert, M. Loewenhaupt, and A. Schneidewind.   Low-energy magnetic excitations of

CeCu$_2$Ge$_2$ investigated by inelastic neutron scattering. Physics Procedia, accepted.

[GHU$^+$02]   T. Goto, S. Hane, K. Umeo, T. Takabatake, and Y. Isikawa. Field-induced magnetic transitions and pressure-induced magnetic instability in CePdAl. *Journal of Physics and Chemistry of Solids*, 63(6–8):1159–1163, 2002.

[GSS08]   P. Gegenwart, Q. Si, and F. Steglich. Quantum criticality in heavy-fermion metals. *Nat Phys*, 4(3):186–197, 2008.

[GTS$^+$15]   S. K. Goh, D. A. Tompsett, P. J. Saines, H. C. Chang, T. Matsumoto, M. Imai, K. Yoshimura, and F. M. Grosche. Ambient pressure structural quantum critical point in the phase diagram of (Ca$_x$Sr$_{1-x}$)$_3$Rh$_4$Sn$_{13}$. *Phys. Rev. Lett.*, 114:097002, 2015.

[GZ74]   G. Gruner and A. Zawadowski. Magnetic impurities in non-magnetic metals. *Reports on Progress in Physics*, 37(12):1497, 1974.

[HBP$^+$07]   V. Hinkov, P. Bourges, S. Pailhes, Y. Sidis, A. Ivanov, C. D. Frost, T. G. Perring, C. T. Lin, D. P. Chen, and B. Keimer. Spin dynamics in the pseudogap state of a high-temperature superconductor. *Nat Phys*, 3(11):780–785, 2007.

[Her76]   J. A. Hertz. Quantum critical phenomena. *Phys. Rev. B*, 14:1165–1184, 1976.

[HH69]   B. I. Halperin and P. C. Hohenberg. Scaling laws for dynamic critical phenomena. *Phys. Rev.*, 177:952–971, 1969.

[HHML$^+$81]   S. Horn, E. Holland-Moritz, M. Loewenhaupt, F. Steglich, H. Scheuer, A. Benoit, and J. Flouquet. Magnetic neutron scattering and crystal-field states in CeCu$_2$Si$_2$. *Phys. Rev. B*, 23:3171–3176, 1981.

[HKE$^+$15]   Z. Huesges, M. M. Koza, J. P. Embs, T. Fennell, G. Simeoni, C. Geibel, C. Krellner, and O. Stockert. Ferromagnetic fluctuations in YbNi$_4$P$_2$ measured by inelastic neutron scattering. *Journal of Physics: Conference Series*, 592(1):012083, 2015.

[HSK$^+$13]   Z. Huesges, O. Stockert, M. M. Koza, C. Krellner, C. Geibel, and F. Steglich. Crystalline electric field splitting in YbNi$_4$P$_2$

measured by inelastic neutron scattering. *physica status solidi (b)*, 250(3):522–524, 2013.

[Hut64]   M. Hutchings. Point-charge calculations of energy levels of magnetic ions in crystalline electric fields. *SOLID STATE PHYSICS-ADVANCES IN RESEARCH AND APPLICATIONS*, 16:227–273, 1964.

[Jee10]   H. S. Jeevan. *Crystal Growth and Investigation of* $CeCu_2Si_2$ *and* $YbRu_2Ge_2$: *Competition/Co-existence of Superconducting, Dipolar and Quadrupolar order*. PhD thesis, Technical University Dresden, 2010.

[JM91]   J. Jensen and A. R. Mackintosh. *Rare Earth Magnetism*. Oxford Univ. Press, 1991.

[Kas56]   T. Kasuya. A theory of metallic ferro- and antiferromagnetism on Zener's model. *Progress of Theoretical Physics*, 16(1):45–57, 1956.

[KB03]   T. R. Kirkpatrick and D. Belitz. Nature of the quantum phase transition in clean itinerant heisenberg ferromagnets. *Phys. Rev. B*, 67:024419, 2003.

[KCB00]   Y. Kuz'ma, S. Chykhrij, and S. Budnyk. Yb-Ni-P system. *Journal of Alloys and Compounds*, 298(12):190–194, 2000.

[KDKvdB02] L. Keller, A. Dönni, H. Kitazawa, and B. van den Brandt. Geometrical frustration and incommensurate magnetic ordering in CePdAl: A low-temperature neutron-diffraction study. *Applied Physics A*, 74(1):s686–s688, 2002.

[KG12]   C. Krellner and C. Geibel. Magnetic anisotropy of $YbNi_4P_2$. *Journal of Physics: Conference Series*, 391(1):012032, 2012.

[KIO$^+$02] Y. Kawasaki, K. Ishida, K. Obinata, K. Tabuchi, K. Kashima, Y. Kitaoka, O. Trovarelli, C. Geibel, and F. Steglich. Exotic magnetism and superconductivity in Ge-substituted $CeCu_2Si_2$: A Cu NQR study. *Phys. Rev. B*, 66:224502, 2002.

[KLS$^+$11] C. Krellner, S. Lausberg, A. Steppke, M. Brando, L. Pedrero, H. Pfau, S. Tencé, H. Rosner, F. Steglich, and C. Geibel. Ferromagnetic quantum criticality in the quasi-one-dimensional heavy fermion metal $YbNi_4P_2$. *New Journal of Physics*, 13(10):103014, 2011.

[KM88]   M. Kato and K. Machida. Superconductivity and spin-density waves: Application to heavy-fermion materials. *Phys. Rev. B*, 37:1510–1519, 1988.

[KMMS94]   H. Kitazawa, A. Matsushita, T. Matsumoto, and T. Suzuki. Electronic and thermal properties of CePdAl. *Physica B: Condensed Matter*, 199–200(0):28–30, 1994.

[Kon64]   J. Kondo. Resistance minimum in dilute magnetic alloys. *Progress of Theoretical Physics*, 32(1):37–49, 1964.

[KPG14]   F. Krüger, C. J. Pedder, and A. G. Green. Fluctuation-driven magnetic hard-axis ordering in metallic ferromagnets. *Phys. Rev. Lett.*, 113:147001, 2014.

[KRF$^+$03] W. Knafo, S. Raymond, B. Fåk, G. Lapertot, P. C. Canfield, and J. Flouquet. Study of low-energy magnetic excitations in single-crystalline CeIn$_3$ by inelastic neutron scattering. *Journal of Physics: Condensed Matter*, 15(22):3741, 2003.

[Lan57]   L. D. Landau. The theory of a fermi liquid. *SOVIET PHYSICS JETP-USSR*, 3(6):920–925, 1957.

[LRVW07]   H. v. Löhneysen, A. Rosch, M. Vojta, and P. Wölfle. Fermi-liquid instabilities at magnetic quantum phase transitions. *Rev. Mod. Phys.*, 79:1015–1075, 2007.

[LTGC$^+$11] M. Le Tacon, G. Ghiringhelli, J. Chaloupka, M. M. Sala, V. Hinkov, M. W. Haverkort, M. Minola, M. Bakr, K. J. Zhou, S. Blanco-Canosa, C. Monney, Y. T. Song, G. L. Sun, C. T. Lin, G. M. De Luca, M. Salluzzo, G. Khaliullin, T. Schmitt, L. Braicovich, and B. Keimer. Intense paramagnon excitations in a large family of high-temperature superconductors. *Nat Phys*, 7(9):725–730, 2011.

[Luc14]   S. Lucas. Stabilität der magnetischen Ordnung im geometrisch frustrierten Schwere-Fermionen-System CePd$_{1-x}$Ni$_x$Al. Master's thesis, Technical University Dresden, 2014.

[Mil93]   A. J. Millis. Effect of a nonzero temperature on quantum critical points in itinerant fermion systems. *Phys. Rev. B*, 48:7183–7196, 1993.

[Mis08]   P. Misra. *Heavy-Fermion Systems*. Elsevier, 2008.

[MPL07]   P. Monthoux, D. Pines, and G. G. Lonzarich. Superconductivity without phonons. *Nature*, 450(7173):1177–1183, 2007.

[MT95]   T. Moriya and T. Takimoto. Anomalous properties around magnetic instability in heavy electron systems. *Journal of the Physical Society of Japan*, 64(3):960–969, 1995.

[Mur83]   A. P. Murani. Magnetic spectral response in the intermetallic compound $CeSn_3$. *Phys. Rev. B*, 28:2308–2311, 1983.

[Neu03]   Neutron data booklet. Institut Laue-Langevin, 2003.

[NK]   P. Novák and J. Kuneš. Private communication.

[NKK13]   P. Novák, K. Knížek, and J. Kuneš. Crystal field parameters with wannier functions: Application to rare-earth aluminates. *Phys. Rev. B*, 87:205139, 2013.

[NKM+13]   P. Novák, K. Knížek, M. Maryško, Z. Jirák, and J. Kuneš. Crystal field and magnetism of Pr^{3+} and Nd^{3+} ions in orthorhombic perovskites. *Journal of Physics: Condensed Matter*, 25(44):446001, 2013.

[NnRLC97]   M. D. Núñez Regueiro, C. Lacroix, and B. Canals. Magnetic ordering in the frustrated Kondo lattice compound CePdAl. *Physica C: Superconductivity*, 282–287, Part 3(0):1885–1886, 1997.

[Nol02]   W. Nolting. *Grundkurs Theoretische Physik*. Springer, 2002.

[OKH+96]   A. Oyamada, K. Kamioka, K. Hashi, S. Maegawa, T. Goto, and H. Kitazawa. NMR studies of the antiferromagnetic heavy fermion compound CePdAl. *J. Phys. Soc. Jpn.*, 65:123–128, 1996.

[OMN+08]   A. Oyamada, S. Maegawa, M. Nishiyama, H. Kitazawa, and Y. Isikawa. Ordering mechanism and spin fluctuations in a geometrically frustrated heavy-fermion antiferromagnet on the Kagome-like lattice CePdAl: A ^{27}Al NMR study. *Phys. Rev. B*, 77:064432, 2008.

[Pfl09]   C. Pfleiderer. Superconducting phases of f-electron compounds. *Rev. Mod. Phys.*, 81:1551–1624, 2009.

[PMA+06]   K. Prokeš, P. Manuel, D. Adroja, H. Kitazawa, T. Goto, and Y. Isikawa. Magnetic order in CePdAl single crystal: Effect of magnetic field. *Physica B: Condensed Matter*, 385–386, Part 1(0):359–362, 2006.

[PMA+07]   K. Prokeš, P. Manuel, D. Adroja, H. Kitazawa, T. Goto, and Y. Isikawa. Magnetic order of CePdAl under pressure - neutron diffraction study. *Journal of Magnetism and Magnetic Materials*, 310(2, Part 1):e28–e30, 2007.

[PP62]   H. H. Paalman and C. J. Pings. Numerical evaluation of x-ray absorption factors for cylindrical samples and annular sample cells. *Journal of Applied Physics*, 33(8):2635–2639, 1962.

[Pri06]   E. Prince, editor. *International Tables of Crystallography*, volume C, Mathematical, Physical and Chemical Tables. First online edition edition, 2006.

[RASN14]   M. A. Romero, A. A. Aligia, J. G. Sereni, and G. Nieva. Interpretation of experimental results on Kondo systems with crystal field. *Journal of Physics: Condensed Matter*, 26(2):025602, 2014.

[res]   Restrax version 5.2.4. http://neutron.ujf.cas.cz/restrax/.

[RK54]   M. A. Ruderman and C. Kittel. Indirect exchange coupling of nuclear magnetic moments by conduction electrons. *Phys. Rev.*, 96:99–102, 1954.

[RLK+13]   M. Rotter, D. M. Le, J. Keller, L. G. Pascut, T. Hoffmann, M. Doerr, R. Schedler, P. Fabi, S. Rotter, M. Banks, and N. Klüver. *McPhase Users Manual*. http://mcphase.de, 2013.

[RSS+14]   S. E. Rowley, L. J. Spalek, R. P. Smith, M. P. M. Dean, M. Itoh, J. F. Scott, G. G. Lonzarich, and S. S. Saxena. Ferroelectric quantum criticality. *Nat. Phys.*, 10:367–372, 2014.

[SAA+06]   O. Stockert, D. Andreica, A. Amato, H. Jeevan, C. Geibel, and F. Steglich. Magnetic order and superconductivity in single-crystalline $CeCu_2Si_2$. *Physica B: Condensed Matter*, 374–375(0):167–170, 2006.

[SAB+79]   F. Steglich, J. Aarts, C. D. Bredl, W. Lieke, D. Meschede, W. Franz, and H. Schäfer. Superconductivity in the presence

of strong pauli paramagnetism: $CeCu_2Si_2$. *Phys. Rev. Lett.*, 43:1892–1896, 1979.

[SAF$^+$11]   O. Stockert, J. Arndt, E. Faulhaber, C. Geibel, H. S. Jeevan, S. Kirchner, M. Loewenhaupt, K. Schmalzl, W. Schmidt, Q. Si, and F. Steglich. Magnetically driven superconductivity in $CeCu_2Si_2$. *Nat Phys*, 7(2):119–124, 2011.

[Sar96]   J. Saroun. Restrax. *ILL Technical Report*, 96SA08T, 1996.

[SAS$^+$08]   O. Stockert, J. Arndt, A. Schneidewind, H. Schneider, H. Jeevan, C. Geibel, F. Steglich, and M. Loewenhaupt. Magnetism and superconductivity in the heavy-fermion compound $CeCu_2Si_2$ studied by neutron scattering. *Physica B: Condensed Matter*, 403(59):973–976, 2008.

[SBKG]   R. Sarkar, M. Baenitz, C. Krellner, and C. Geibel. To be published.

[Sca12]   D. J. Scalapino. A common thread: The pairing interaction for unconventional superconductors. *Rev. Mod. Phys.*, 84:1383–1417, 2012.

[SDJ$^+$10]   S. Seiro, M. Deppe, H. Jeevan, U. Burkhardt, and C. Geibel. Flux crystal growth of $CeCu_2Si_2$: Revealing the effect of composition. *physica status solidi (b)*, 247(3):614–616, 2010.

[SFS$^+$06]   O. Stockert, E. Faulhaber, K. Schmalzl, W. Schmidt, H. S. Jeevan, M. Deppe, C. Geibel, T. Cichorek, T. Nakanishi, M. Loewenhaupt, and F. Steglich. Peculiarities of the antiferromagnetism in $CeCu_2Si_2$. *Journal of Physics: Conference Series*, 51(1):211, 2006.

[SFZ$^+$04]   O. Stockert, E. Faulhaber, G. Zwicknagl, N. Stüßer, H. S. Jeevan, M. Deppe, R. Borth, R. Küchler, M. Loewenhaupt, C. Geibel, and F. Steglich. Nature of the a phase in $CeCu_2Si_2$. *Phys. Rev. Lett.*, 92:136401, 2004.

[SGG$^+$96]   F. Steglich, P. Gegenwart, C. Geibel, R. Helfrich, P. Hellmann, M. Lang, A. Link, R. Modler, G. Sparn, N. Büttgen, and A. Loidl. New observations concerning magnetism and superconductivity in heavy-fermion metals. *Physica B: Condensed Matter*, 223–224(0):1–8, 1996.

[Si06]   Q. Si. Global magnetic phase diagram and local quantum crit-
              icality in heavy fermion metals. *Physica B: Condensed Matter*,
              378–380:23–27, 2006.

[SJL$^+$94]   C. Schank, F. Jährling, L. Luo, A. Grauel, C. Wassilew,
              R. Borth, G. Olesch, C. Bredl, C. Geibel, and F. Steglich. 4f-
              conduction electron hybridization in ternary Ce–TM–Al com-
              pounds. *Journal of Alloys and Compounds*, 207–208(0):329–
              332, 1994.

[SKL$^+$13]   A. Steppke, R. Küchler, S. Lausberg, E. Lengyel, L. Steinke,
              R. Borth, T. Lühmann, C. Krellner, M. Nicklas, C. Geibel,
              F. Steglich, and M. Brando. Ferromagnetic quantum critical
              point in the heavy-fermion metal $YbNi_4(P_{1-x}As_x)_2$. *Science*,
              339(6122):933–936, 2013.

[SL]   O. Stockert and S. Lucas. Private communication.

[SNT$^+$07]   O. Stockert, M. Nicklas, P. Thalmeier, P. Gegenwart, and
              F. Steglich. *Handbook of Magnetism and Advanced Magnetic
              Materials*, chapter Magnetism and Quantum Criticality in
              Heavy-Fermion Compounds: Interplay with Superconductiv-
              ity. John Wiley & Sons, Ltd., 2007.

[SS11]   O. Stockert and F. Steglich. Unconventional quantum critical-
              ity in heavy-fermion compounds. *Annual Review of Condensed
              Matter Physics*, 2(1):79–99, 2011.

[ST08]   R. Srivastava and W. Teizer. Analytical density of states in
              the Abrikosov-Gorkov theory. *Solid State Communications*,
              145(910):512–513, 2008.

[Sto]   O. Stockert. Private communication.

[TMKM96]   J. Tang, A. Matsushita, H. Kitazawa, and T. Matsumoto. High
              pressure effect on the magnetic transition in heavy fermion
              systems $CePd_2Al_3$ and CePdAl. *Physica B: Condensed Matter*,
              217(12):97–101, 1996.

[vDFC$^+$97] N. van Dijk, B. Fåk, T. Charvolin, P. Lejay, J. Mignot, and
              B. Hennion. Magnetic excitations in $CePd_2Si_2$. *Physica B:
              Condensed Matter*, 241–243(0):808–810, 1997.

[Voj03]   M. Vojta. Quantum phase transitions. *Reports on Progress in Physics*, 66(12):2069, 2003.

[Voj08]   M. Vojta. From itinerant to local-moment antiferromagnetism in Kondo lattices: Adiabatic continuity versus quantum phase transitions. *Phys. Rev. B*, 78:125109, 2008.

[WK74]   K. G. Wilson and J. Kogut. The renormalization group and the expansion. *Physics Reports*, 12(2):75–199, 1974.

[WLRS04]   H. Wilhelm, T. Lühmann, T. Rus, and F. Steglich. A compensated heat-pulse calorimeter for low temperatures. *Review of Scientific Instruments*, 75(8):2700–2705, 2004.

[Wut12]   J. Wuttke. Absorption-correction factors for scattering from flat or tubular samples: Open-source implementation libabsco, and why it should be used with caution. online resources, 2012. Jülich Centre for Neutron Science at FRM II.

[XSH94]   B. Xue, H. Schwer, and F. Hulliger. Structure of CePdAl. *Acta Crystallographica Section C*, 50(3):338–340, 1994.

[YGD$^+$03]   H. Q. Yuan, F. M. Grosche, M. Deppe, C. Geibel, G. Sparn, and F. Steglich. Observation of two distinct superconducting phases in $CeCu_2Si_2$. *Science*, 302(5653):2104–2107, 2003.

[Yos57]   K. Yosida. Magnetic properties of Cu-Mn alloys. *Phys. Rev.*, 106:893–898, 1957.

[YS10]   S. J. Yamamoto and Q. Si. Metallic ferromagnetism in the Kondo lattice. *Proceedings of the National Academy of Sciences*, 107(36):15704–15707, 2010.

[ZGRS03]   L. Zhu, M. Garst, A. Rosch, and Q. Si. Universally diverging Grüneisen parameter and the magnetocaloric effect close to quantum critical points. *Phys. Rev. Lett.*, 91:066404, 2003.

[ZHM$^+$13]   K.-J. Zhou, Y.-B. Huang, C. Monney, X. Dai, V. N. Strocov, N.-L. Wang, Z.-G. Chen, C. Zhang, P. Dai, L. Patthey, J. van den Brink, H. Ding, and T. Schmitt. Persistent high-energy spin excitations in iron-pnictide superconductors. *Nat Commun*, 4:1470, 2013.

[ZJ93]   K. Zeppenfeld and W. Jeitschko. Magnetic behaviour of Ni_3P, Ni_2P, NiP_3 and the series $Ln_2Ni_{12}P_7$ (Ln = Pr, Nd, Sm, Gd–Lu). *Journal of Physics and Chemistry of Solids*, 54(11):1527–1531, 1993.

Acknowledgment

The success of any PhD thesis depends hugely on the willingness and ability of more experienced scientists to pass on their knowledge. In that regard, I consider myself very lucky, since I conducted my PhD in a work environment where both are abundant. First and foremost, I would like to thank my supervisor Oliver Stockert: During the last four years, he supported me a lot whenever I reached the limits of my capabilities, but gave me plenty of trust and freedom when I was within - this matches very closely my idea of what good supervision is. Furthermore, there were many people in the institute who were not formally my supervisors, but still taught be a lot over the time, the most important being Christoph Geibel, Burkhard Schmidt and Manuel Brando. Also among the PhD students, there were plenty of helpful discussions, most importantly, but not exclusively in our theory-circle; here I would like to mention Sarah Wunderlich, Sandra Hamann, Katharina Weber, Heike Pfau, Stefan Lucas and Alexander Steppke. I have also profited much from the weekly meetings with other members of the neutron scattering group, Ariane Hannaske, Sarah Wunderlich, Stefan Lucas and Oliver Stockert.

I am thankful to all my colleagues at the MPI for Chemical Physics of Solids for the friendly work atmosphere, especially the department Physics of Quantum Materials. Many visits to the Mensa, many conversations in the coffee corner and quite a few after-work activities have certainly had a big impact on making my stay in Dresden a very enjoyable time for me. The heads of the department, Frank Steglich and Andy Mackenzie, I thank for providing me the opportunity to work in their group. I would also like to acknowledge the excellent support I have received from the administrative and technical staff in the institute, who have done a lot to make work easier for me.

The major part of my thesis was funded by the DFG-Forschergruppe 960 "Quantum Phase Transitions". Apart from financial support, I would like to acknowledge the fruitful discussions at several workshops and the productive cooperation on the CePdAl project with KIT (Karlsruhe Institute of Technology) and the University of Augsburg. Here I would like to mention

Versicherung

Hiermit versichere ich, dass ich die vorliegende Arbeit ohne unzulässige Hilfe Dritter und ohne Benutzung anderer als der angegebenen Hilfsmittel angefertigt habe; die aus fremden Quellen direkt oder indirekt übernommenen Gedanken sind als solche kenntlich gemacht. Die Arbeit wurde bisher weder im Inland noch im Ausland in gleicher oder ähnlicher Form einer anderen Prüfungsbehörde vorgelegt.

Die Dissertation wurde in der Zeit vom Oktober 2011 bis zum Oktober 2015 am Max-Planck-Institut für Chemische Physik fester Stoffe in Dresden angefertigt, unter der Betreuung von PD Oliver Stockert.

Ich erkenne die Promotionsordnung der Technischen Universität Dresden, Fakultät Mathematik und Naturwissenschaften, vom 23.02.2011 an.